Doctoral Thesis

Controlling thermal emission and light matter interaction using phonon-induced epsilon-near-zero materials in the mid-infrared region

Author:
Maryam Abbasi

Supervisor:
Professor Robert W.Boyd

A thesis submitted to the University of Ottawa in fulfillment of the requirements for the degree of Doctor of Philosophy

in the

School of Electrical Engineering and Computer Science

School of Electrical Engineering and Computer Science
Faculty of Engineering
University of Ottawa

December 19, 2025

Declaration of Authorship

I, Maryam Abbasi, declare that this thesis is my work and is written entirely by myself. Specific contributions are as follows:

Chapter 1. An overview of the field studied in this thesis, entirely written and gathered by Maryam Abbasi, and supervised by Prof. Robert W. Boyd.

Chapter 2. Conceptualization, numerical simulations, experimental design, measurements, data analysis, writing the manuscript entirely by: Maryam Abbasi. Sample fabrication and provision: Dr. Florentina Ganotte and Prof. Gerd Leuchs. Supervision: Prof. Robert W. Boyd. Additional guidance: Dr. Jeremy Upham, Dr. R. Margoth Córdova-Castro, Dr. M. Zahirul Alam, Prof. Gerd Leuchs.

Chapter 3. Numerical simulations, experiments, data analysis, writing the manuscript entirely by: Maryam Abbasi. Sample fabrication: Dr. Matthew Klein, Dr. Dennis E. Walker Jr., Dr. Shivashankar Vangala, Dr. Joshua R. Hendrickson. Supervision: Prof. Robert W. Boyd. Additional guidance: Dr. M. Zahirul Alam, and Dr. Jeremy Upham.

Chapter 4. Numerical simulations and experiments entirely by: Maryam Abbasi. Sample fabrication: Dr. Matthew Klein, Dr. Dennis E. Walker Jr., Dr. Shivashankar Vangala, Dr. Joshua R. Hendrickson. Supervision: Prof. Robert W. Boyd. Additional guidance: Dr. M. Zahirul Alam, and Dr. Jeremy Upham.

Signed:

_____

Date:

_____

Abstract

This thesis explores phonon-induced epsilon-near-zero (ENZ) materials as a platform for tailoring light–matter interactions in the mid-infrared (mid-IR) spectral regime. After introducing the fundamental concepts of thermal emission, light–matter interaction in subwavelength structures, and the unique electromagnetic properties of polar dielectrics near their optical phonon resonances, we show how ENZ conditions can (i) enable spectrally selective, temporally improved thermal emission and (ii) support strong coupling between gap-plasmon resonances and ENZ phonon-polaritons.

The first research project of my thesis investigates ultra-thin silicon dioxide (SiO_2) films, which support phonon-polariton resonances near their longitudinal optical (LO) phonon frequency. By leveraging the dispersive behavior of SiO_2 in the ENZ regime, we demonstrate spectrally selective and temporally coherent thermal emission from structures with thicknesses much smaller than the emission wavelength. Full-wave electromagnetic simulations, supported by angle- and polarization-resolved emissivity measurements, confirm the emergence of partially coherent thermal radiation, offering a platform for narrowband mid-IR thermal sources.

In the second part of the thesis, we study the strong coupling between gap-plasmon resonances—supported by a metallic–dielectric–metal antenna array—and the ENZ phonon-polariton mode of an ultra-thin aluminum oxide (Al_2O_3) film. This interaction gives rise to hybrid polaritonic states characterized by modified dispersion and strong field confinement. Numerical and experimental investigations confirm that the system operates in the strong coupling regime, with tunable mode positions achieved by varying structural parameters such as antenna dimensions and ENZ film thickness.

Finally, we present a numerical study of field enhancement in the coupled gap-plasmon–ENZ system. Simulations reveal that decreasing the ENZ film thickness leads to significant field concentration within the structure, with electric field magnitudes approaching two orders of magnitude above the incident field. These findings underscore the potential of ENZ-coupled plasmonic systems for enhancing nonlinear optical effects and advancing mid-IR photonic applications.

Acknowledgements

I am deeply grateful to my supervisor, Prof. Robert W. Boyd, for the opportunity to join his group and for his generosity with ideas, encouragement, and support throughout this work. He provided the resources and, more importantly, the freedom to explore and develop new ideas. I am especially thankful for the trust he placed in me to pursue an exciting topic during my PhD. His openness fostered a learning environment where his succinct, fundamental questions and thoughtful comments guided me toward a clearer understanding. I deeply appreciate his approach as a generous way of helping students recognize and correct mistakes without discouragement.

I have benefited greatly from technical discussions with Dr. Jeremy Upham and from his helpful feedback, as well as his efforts in organizing our weekly group meetings. I thank Dr. M. Zahirul Alam for valuable discussions and diligent questions that strengthened this work. I am also grateful to Dr. Florentina Gannott, Dr. Matthew Klein, Dr. Dennis E. Walker Jr., Dr. Shivashankar Vangala, Dr. Joshua R. Hendrickson, and Dr. R. Margoth Córdova-Castro for their excellent work on fabrication of samples. I thank all of my group-mates for the nice moments in our meetings; I learned from you all. In particular, I should mention Yaswant and Theng Loo for their kind and encouraging words during the final months of my PhD and making the last stages of writing this thesis easier. And, it was a true honor to know and learn from Prof. Gerd Leuchs. I am sincerely thankful for our discussions in physics, giving me the opportunity to collaborate on another paper (not included in this thesis), his support in facilitating sample provision, and his thoughtful feedback on our manuscript.

I would like to express special thanks to my parents, Anoushirvan and Sohiela, for their unwavering support through all these years. I also would like to acknowledge two other names, Alena (5), and Alma (1.5), my nieces, the two work-life-balance officers from Vancouver forcing me to take a few days off from my PhD life. The doctoral journey has its ups and downs, and I am sincerely thankful to my family and friends who supported me during challenging periods. My motivation in pursuing a PhD was to enjoy doing science, unravel a mystery, contribute something new, and test myself. I am grateful for this journey.

Finally, I am grateful to the members of my examination committee for their time, thoughtful review, and insightful feedback, which improves the clarity of this thesis.

Contents

List of Abbreviations

DFG	Difference Frequency Generator
DOS	Density Of States
ENZ	Epsilon-Near-Zero
FDTD	Finite-Difference Time-Domain
FTIR	Fourier Transform Infra-Red
GSPs	Gap Surface Plasmons
GPA	Gap Plasmon Antenna
hBN	hexagonal Boron Nitride
ITO	Indium Tin Oxide
LSPR	Localized Surface Plasmon Resonance
LO	Longitudinal Optical
MIM	Metal-Insulator-Metal
OPG	Optical Parametric Generator
SEM	Scanning Electron Microscopy
SPhP	Surface Phonon Polariton
SPP	Surface Plasmon Polariton
TE	Transverse Electric
TM	Transverse Magnetic
TO	Transverse Optical

Chapter 1

Fundamentals

1.1 Introduction

Advances in nanophotonics and thermal photonics have enabled unprecedented control over the spectral, directional, and polarization properties of thermal radiation—moving beyond the statistical limits described by Planck's law and the classical concept of blackbody emission [1, 2, 3]. This emerging control over thermal emission is critical for applications including infrared sensing, energy harvesting, and spectrally/directionally selective thermal light sources [1, 4, 5, 6, 7, 8, 9, 10].

The primary motivation of this thesis stems from the fundamental and applied significance of understanding how reducing the thickness of a polar dielectric film to nanometer scales alters its thermal emission characteristics. A central theme is the engineering of optical modes and the photonic density of states using subwavelength structures and materials with tailored electromagnetic responses. Among these, materials exhibiting epsilon-near-zero (ENZ) behavior—where the real part of the dielectric permittivity approaches zero at specific frequencies—have attracted considerable attention [11, 12]. Specifically, we investigate the emergence of narrowband and temporally coherent emission in ultra-thin SiO_2 films and relate these phenomena to ENZ-induced field uniformity and mode confinement [12, 13]. Silicon dioxide (SiO_2) supports transverse optical (TO) and longitudinal optical (LO) phonon resonances in the mid-infrared range; near the LO phonon, SiO_2 exhibits ENZ behavior [13, 14, 15]. While prior research has investigated ENZ-enhanced response in related phononic and plasmonic systems—including ultra-thin AlN emitters and optically thin reststrahlen media, as well as plasmonic ENZ (ITO) platforms [16, 17, 18]—the potential of ultra-thin SiO_2 films as mid-IR thermal emitters remains comparatively underexplored. Our approach is grounded in the formalism of thermal radiation and fluctuational

electrodynamics, emphasizing how subwavelength thickness can suppress incoherent channels and favor selected modes [3, 12, 19, 20]. We experimentally investigate the spectral and angular dependence of thermal emission from ultra-thin SiO_2 films, and we numerically model the absorption spectra of our structures using realistic dielectric functions extracted from ellipsometry.

In addition to characterizing thermal emission from SiO_2 thin films, this thesis explores hybrid systems where ultra-thin ENZ films are integrated with plasmonic structures. In the ENZ regime, the electric field can exhibit near-uniform phase and strong amplitude enhancement within the material, leading to unique phenomena such as enhanced nonlinearity, strong field confinement, and modified emission [11, 12]. We harness this property by coupling to ENZ modes using gap-plasmon antennas, which provide reconfigurable mid-IR resonances for different applications [21]. In particular, we study strong coupling between gap-plasmon cavity modes and the phonon-polariton ENZ mode of an ultra-thin polar dielectric, giving rise to hybrid polaritonic states with modified dispersion and enhanced local fields [22, 23]. This platform is promising for both thermal emission control and nonlinear optical enhancement. We explore the strong coupling between the gap-plasmon resonances of gold patch antennas and the ENZ phonon-polariton mode of an aluminum oxide thin film, and extract key parameters such as resonance splitting, coupling strength. We analyze and quantify the electric field enhancement associated with the hybrid modes, particularly within the ENZ layer, and assess its implications for enhancing nonlinear optical processes such as second- and third-harmonic generation.

In fulfilling these objectives, this thesis contributes to the broader understanding of light–matter interaction in polar materials in the mid-IR spectrum, offering new insights into spectrally selective (coherent, in the interferometric sense) thermal radiation and nonlinear photonic devices. By leveraging the unique properties of ENZ modes and plasmon–phonon hybridization, the work opens pathways toward engineering compact mid-IR thermal emitters. In the following sections, we introduce the key concepts that are the main focus of this thesis and are used in other chapters to establish the foundation for the subsequent chapters.

1.2 Thermal emission

Thermal emission is the process by which all matter with a finite temperature radiates electromagnetic energy. Historically, the theoretical foundations for thermal radiation were established by Kirchhoff, who formulated the principle of thermal equilibrium, and Planck, who derived the spectral distribution of blackbody radiation [3]. Under these classical assumptions, thermal radiation is considered isotropic, temporally and spatially incoherent, and spectrally broadband. Planck's law, which relates the spectral radiance of a blackbody to temperature and wavelength, assumes local thermodynamic equilibrium and neglects the material and structural complexities that can modify radiation behavior. As a result, thermal radiation was seen as fundamentally incoherent and unpolarized, offering limited avenues for engineering its properties beyond emissivity modulation.

1.2.1 Planck's Law of thermal radiation

Planck's law describes how the temperature of a body determines the amplitude and spectrum of its thermal emission. It provides a precise mathematical framework for understanding the distribution of electromagnetic radiation emitted by a blackbody in thermal equilibrium. A blackbody is defined as an object that perfectly absorbs all the radiant energy incident on it [3]. If that body is in thermal equilibrium with its surroundings, then in addition to being a perfect absorber, it must also be a perfect radiator, in the sense that it must reradiate as much energy as it absorbs; otherwise, it could not remain in thermal equilibrium. At its core, Planck's law states that the spectral energy density (energy per unit volume) of a system is influenced by the temperature of the system and can be expressed as [2, 3, 24]:

$$I(\omega) = E(\omega, T) \cdot \mathrm{DOS}, \tag{1.1}$$

where $I(\omega)$ is the spectral energy density, which represents the energy emitted per unit frequency and unit volume at angular frequency ω, $E(\omega, T)$ is the mean energy per photon at a given frequency ω and the absolute temperature of the blackbody T, DOS refers to the Density of States, which accounts for the number of available photon states at each frequency. The mean energy per photon $E(\omega, T)$ is given by:

$$E(\omega, T) = \hbar\omega N(\omega, T), \tag{1.2}$$

where $\hbar$ is the reduced Planck constant ($\hbar = h/2\pi$) and $N(\omega, T)$ is the photon number distribution. To find the photon number we can start from Maxwell–Boltzmann distribution which gives the occupation probability of the optical states as a function of frequency at thermal equilibrium. Maxwell–Boltzmann statistics dictate that the probability of the occupation of a state with energy E is e^{-E/k_BT}, where k_B is the Boltzmann constant. Thus, the average energy per state, E, can be calculated by taking a weighted average of the possible energies and their probability of occupation. The equation below calculates the mean photon energy by adding the allowed energies ($E_i = i\hbar\omega, i = 0, 1, 2, ...$) multiplied by the occupation probabilities divided by the sum of the probabilities [24]:

$$E(\omega, T) = \frac{0 \cdot e^0 + \hbar\omega \cdot e^{-\hbar\omega/k_BT} + 2\hbar\omega \cdot e^{-2\hbar\omega/k_BT} + \cdots}{1 + e^{-\hbar\omega/k_BT} + e^{-2\hbar\omega/k_BT} + \cdots}. \tag{1.3}$$

Summing the infinite series and dividing, we get the equation below which is the Bose-Einstein distribution times $\hbar\omega$ and describes the mean photon energy at thermal equilibrium:

$$E(\omega, T) = \hbar\omega \cdot \frac{1}{\exp\left(\frac{\hbar\omega}{k_BT}\right) - 1}. \tag{1.4}$$

Finally, the total energy radiated by an emitter per unit volume at a given frequency ω is the product of the mean energy per photon $E(\omega, T)$ and density of states. The DOS quantifies the number of allowed electromagnetic modes per unit volume and per unit frequency interval. Consider a rectangular cavity with perfectly reflecting walls and side lengths L_x, L_y, and L_z. Electromagnetic waves inside this cavity must satisfy boundary conditions that lead to quantized wavevectors of the form:

$$\vec{k} = \left(\frac{2\pi n_x}{L_x}, \frac{2\pi n_y}{L_y}, \frac{2\pi n_z}{L_z}\right), \tag{1.5}$$

where n_x, n_y, n_z in Z are integers. These discrete $\vec{k}$ values form a grid in k-space. Each allowed mode occupies a small volume in k-space given by:

$$\Delta k = \left(\frac{2\pi}{L_x}\right)\left(\frac{2\pi}{L_y}\right)\left(\frac{2\pi}{L_z}\right) = \frac{(2\pi)^3}{V}, \tag{1.6}$$

where $V = L_xL_yL_z$ is the volume of the cavity. Thus, the number of allowed modes inside a shell between k and $k + dk$ is:

$$dN = 2 \cdot \frac{1}{8} \cdot \frac{4\pi k^2 dk}{\Delta k} = \frac{V k^2 dk}{\pi^2}, \tag{1.7}$$

where the factor of 2 accounts for the two possible polarization states, and the 1/8 factor restricts counting to positive values of n_x, n_y, and n_z. The density of states per unit frequency can be found by using the relation $k = \omega/c$, which yields:

$$\frac{dN}{d\omega} = \frac{V\omega^2}{\pi^2 c^3}. \tag{1.8}$$

This expression represents the density of photon states in a rectangular cavity. To calculate the spectral energy density of blackbody radiation, we multiply the DOS by the mean energy per mode, obtained from the Bose–Einstein distribution. Therefore, the energy density per unit frequency for a blackbody becomes the well-known Planck radiation law:

$$I(\omega, T) = \frac{\hbar\omega^3}{\pi^2 c^3} \cdot \frac{1}{\exp(\hbar\omega/k_B T) - 1}. \tag{1.9}$$

It is worth mentioning that, in a fully quantum treatment, each harmonic mode of frequency ω carries a zero-point-energy of $\frac{1}{2}\hbar\omega$ as a result of quantum field fluctuations even at absolute zero temperature. Thus the term $\frac{1}{2}\hbar\omega$ should be added to the mean energy per mode expressed in Eq. 1.4 [20]. Although each mode carries a vacuum energy, it produces no net radiative flux, since the zero-point contribution cancels out and detectors are insensitive to it.

Finally, the emissivity of a material, $\widetilde{\epsilon}(\omega, T)$, is the emission of the object divided by the one from the blackbody which is a measure of how efficiently it emits thermal radiation compared to a perfect blackbody. A blackbody has an emissivity of 1 at all frequencies and temperatures, meaning it emits the maximum possible radiation. For a non-ideal emitter, the emissivity obeys the inequality $0 \leq \widetilde{\epsilon}(\omega, T) < 1$. This formulation highlights the critical role of the density of optical states in determining the thermal emission spectrum of a body in thermal equilibrium [1, 2].

1.2.2 Modification of the density of states in cavities with subwavelength dimensions

When one or more dimensions of a cavity become smaller than the thermal emission wavelength. The boundary conditions imposed by these confined directions begin to

strongly influence the electromagnetic mode structure [25]. In such a scenario, the continuous distribution of states in k-space becomes discrete or even suppressed in certain directions, leading to a substantial modification in the density of optical states (DOS) [24]. This situation is analogous to the electronic "quantum box." Because the states are widely spaced, the density of states just becomes a series of delta functions as each state is encountered. If only one dimension is small, we again have a similar situation to the quantum well for electrons [24].

As an example, consider a planar slab geometry where the thickness d in the z-direction is much smaller than the wavelength of interest ($d \ll \lambda$), while the in-plane dimensions L_x, L_y remain large. The allowed k_z components are now quantized with large spacing:

$$k_z = \frac{n\pi}{d}, \quad n = 1, 2, 3, \ldots \tag{1.10}$$

This quantization effectively limits the number of available longitudinal modes in the z-direction. Consequently, the DOS becomes quasi-two-dimensional, and the number of available optical modes per unit frequency interval is reduced. The density of states in this case is given approximately by:

$$\rho_{\mathrm{2D}}(\omega) \propto \frac{A\omega}{2\pi c^2}, \tag{1.11}$$

where $A = L_x L_y$ is the cross-sectional area of the slab. The linear ω-dependence (instead of ω^2 or ω^3 in 3D) results from the reduced number of degrees of freedom.

In such subwavelength structures the emission can become spectrally and angularly selective. However, for materials with positive real part of permittivity, the structure is below cutoff for guided modes and the enhancements are typically modest compared with the wavelength structure with plasmonic or phononic materials. In polar dielectric materials that exhibit strong phonon-polariton resonances over their reststrahlen band (such as SiO_2 or SiC), the confinement in subwavelength geometries can result in enhanced DOS at specific frequencies (usually around the LO phonon resonance). This enables efficient channeling of thermal energy into spectrally narrow coherent modes. This dimensionality reduction is a foundational concept for engineering thermal emission to provide coherent thermal emission, directional emitters, etc. Moreover, subwavelength confinement modifies not only the overall magnitude of the DOS but also its spectral distribution, opening new avenues in thermal photonics and

energy conversion. This is the main focus of our work discussed in chapter 2 of this thesis where we use an ultra-thin structure to suppress the unwanted emission and provide sharp emission in mid-IR spectrum.

1.2.3 Kirchhoff's Law of thermal emission

Kirchhoff's law states that, in thermal equilibrium and for reciprocal media, the spectral emissivity equals the absorptivity, $\widetilde{\epsilon}(\omega, T) = \alpha(\omega, T)$, where $\widetilde{\epsilon}(\omega, T)$ is the emissivity of the body at a given frequency ω and temperature T, and $\alpha(\omega, T)$ is the absorptivity of the body at the same frequency and temperature [3]. It is worth noting that, in the more general case, both emissivity and absorptance are angle-dependent quantities and can vary with the direction of emission/illumination and polarization. For simplicity, we have not included the angle dependence in the above equation. In practice, this equality provides a powerful route to validate emissivity data against independent absorption/reflectance calculations or measurements [2, 26]. We use this correspondence to compare measured emissivity with numerically calculated absorptance (chapter 2). We note that departures from ideal conditions (e.g., non-isothermal samples or nonreciprocal fields) can produce apparent deviations [27, 28].

Kirchhoff's law implies that a body that is good at absorbing radiation at a given frequency is also good at emitting radiation at that frequency, and vice versa. The principle of detailed balance in thermal equilibrium underpins this law, meaning that the rate of absorption of radiation by a body is equal to the rate at which it emits radiation. Kirchhoff's law is rooted in the concept of thermal equilibrium. In an environment where thermal radiation is exchanged between bodies, the radiation emitted by one body is absorbed by another. The balance between the absorption and emission of radiation is crucial for thermal equilibrium. The law can be derived from the Planck's law of blackbody radiation and the principles of energy conservation. In thermal equilibrium, the radiation emitted by a body should be equal to the radiation it absorbs, ensuring that net energy is not gained or lost. The interaction of electromagnetic radiation with a body depends both on the properties of the material and on the surrounding environment. To provide a rigorous understanding, we can express the net power radiated by a body at temperature T when it is exposed to an incident radiation field $I_{\text{inc}}(\omega)$. The power absorbed per unit area is given by:

$$P_{\text{abs}}(\omega) = \alpha(\omega, T) I_{\text{inc}}(\omega), \tag{1.12}$$

where $\alpha(\omega, T)$ is the absorptivity at frequency ω and $I_{\text{inc}}(\omega)$ is the intensity of incident radiation at the same frequency. In thermal equilibrium, the power emitted by the body at the same frequency ω must be equal to the power it absorbs. According to Planck's law, the radiative intensity emitted by the body at temperature T is given by the following:

$$P_{\text{emit}}(\omega) = \widetilde{\epsilon}(\omega, T) I_{\text{BB}}(\omega, T), \tag{1.13}$$

where $I_{\text{BB}}(\omega, T)$ is the Planck radiation intensity for a blackbody at temperature T, given by Eq. 1.9. In thermal equilibrium, the power emitted by the body must be equal to the power absorbed. Therefore, Kirchhoff's law dictates that:

$$\widetilde{\epsilon}(\omega, T) = \alpha(\omega, T),$$

which implies that the emissivity at any frequency is equal to the absorptivity at that frequency. This relationship holds regardless of the material's properties, as long as the system is in thermal equilibrium.

For a perfect blackbody, $\widetilde{\epsilon}(\omega, T)$ and $\alpha(\omega, T)$ are equal to unity, meaning that it absorbs and emits the maximum amount of radiation at every frequency. This makes blackbodies ideal references for measuring other bodies' emission properties. For real materials, the emissivity and absorptivity are less than 1. A material that is a poor emitter (low $\widetilde{\epsilon}(\omega, T)$) will typically be a poor absorber (low $\alpha(\omega, T)$) as well. This behavior is especially significant in applications such as thermography, where the efficiency of heat radiation and absorption is critical. Kirchhoff's law is consistent with the second law of thermodynamics, which states that energy can neither be created nor destroyed, only transferred. The law ensures that the absorption and emission processes are balanced, thus conserving energy. The relationship between emissivity and absorptivity holds at each frequency ω, meaning that the material's ability to absorb and emit radiation is frequency-dependent.

In our work reported in chapter 2, we use Kirchhoff's law to verify our emissivity measurements. We observe agreement in the behavior of our measured emissivity and the numerically calculated absorptance spectra, but the exact values differ because

Kirchhoff's law strictly applies to perfect absorbers. For thin films with subwavelength dimensions, we expect slight deviations from the law.

1.3 Phonon-induced epsilon-near-zero (ENZ)

ENZ materials are a class of materials whose real part of permittivity vanishes at a specific wavelength, called the ENZ wavelength. Materials can show interesting properties when their permittivity vanishes [11, 29, 30, 31]. A vanishing permittivity also implies the vanishing of the refractive index, $n = \sqrt{\mu\varepsilon}$, where μ and ε are the relative permeability and permittivity of the material. Therefore, the wavelength inside the materials, λ_0/n will be very large, and the phase velocity, $n\omega/c$, will be near zero in propagation direction (λ_0 and c are the wavelength and speed of light in vacuum) [11, 12, 32]. This means that the electromagnetic fields inside the material oscillate in time and with the same phase everywhere within the medium. For plasmonic materials like metals and doped semiconductors, ENZ occurs at frequencies close to their plasma frequency [12, 33]. In addition to plasmon-induced ENZ, we have another category of materials which offer phonon-induced ENZ condition. For example, polar dielectrics have two zero crossings in their permittivity, one occurs at the transverse optical (TO) phonon resonance and one at their longitudinal optical (LO) phonon resonance [14, 25, 34]. These resonances typically occur at infrared frequencies. In this thesis, our focus is on phonon-induced ENZ materials. In chapter 2, we use the phonon-induced ENZ in silicon dioxide thin film to provide sharp thermal emission which is temporally coherent as a result of ENZ condition. In another work, presented in chapter 3, we investigate the coupling between the phonon-induced ENZ mode of aluminum oxide polar dielectric and gap-plasmon antennas. Moreover, in chapter 4 we show how the phonon-induced ENZ in a thin film of aluminum oxide provides field enhancement in the hybridized modes described in chapter 3. In the next section we provide more detail about polar dielectric materials and their interaction with light which will help the reader follow our work in the other chapters more easily.

1.3.1 Optical phonons in polar crystals

In crystalline solids, atoms are arranged in a periodic lattice and can undergo collective vibrational motions. These quantized lattice vibrations are termed phonons, which are bosonic quasiparticles representing the normal modes of the lattice. Phonons are

categorized based on their polarization and propagation characteristics into acoustic and optical phonons. Acoustic phonons correspond to in-phase oscillations of atoms in the lattice whereas optical phonons arise from out-of-phase oscillations between atoms in the basis of the unit cell, typically occurring in crystals with more than one atom per primitive cell [14, 25, 35]. Many naturally occurring materials exhibit optical phonon resonances in the mid-IR range (5–20 μm), making them highly relevant for applications such as thermal emission control, infrared nanophotonics, and radiative heat transfer. This property makes phononic materials highly useful in infrared thermal emitters, passive radiative cooling, and nanophotonic devices [1, 4, 5, 6, 7, 8, 9, 10].

In ionic crystals, such as silicon carbide (SiC), the unit cell contains at least two atoms with opposite charges. These oppositely charged ions can oscillate against each other, leading to optical phonon modes that interact with electromagnetic radiation [14, 35]. Optical phonons are characterized by the relative motion of positive and negative ions in the lattice. When the displacement of ions is perpendicular to the direction of wave propagation, the mode is termed a transverse optical (TO) phonon mode. Conversely, if the displacement is parallel to the propagation direction, it is a longitudinal optical (LO) phonon. The frequencies of these modes at the center of the Brillouin zone (i.e., at zero wavevector) are denoted as ω_{TO} and ω_{LO}, respectively. Because LO phonons generate long-range electric field, they experience larger restoring force compared to TO phonons. Due to long-range Coulomb interactions in polar crystals, ω_{LO} is typically higher than ω_{TO}. The optical modes can interact strongly with electromagnetic radiation, especially in polar materials, resulting in the formation of hybrid quasiparticles known as phonon polaritons. As discussed in chapter 14 of Kittel [35], this coupling arises because the transverse optical (TO) phonons generate a macroscopic electric field, and when an incident electromagnetic wave interacts with this field, it can no longer propagate independently. Instead, the coupled system exhibits mixed modes that are part photon, part phonon. Furthermore, between the frequencies ω_{TO} and ω_{LO}, the real part of the dielectric function $\mathrm{Re}[\epsilon(\omega)]$ becomes negative. This frequency range is known as the reststrahlen band [14, 25]. Within this band, the material exhibits high reflectivity similar to the behavior of metals (below their plasma frequency), also called optical metals [14]. The negative permittivity arises due to the resonance between the incident electromagnetic wave and the optical phonon modes. The frequencies of LO and TO phonons at the Brillouin zone center

($q \to 0$) are related through the Lyddane–Sachs–Teller (LST) relation under certain assumptions:

$$\frac{\varepsilon_0}{\varepsilon_\infty} = \left(\frac{\omega_{\mathrm{LO}}}{\omega_{\mathrm{TO}}}\right)^2, \tag{1.14}$$

where ε_0 is the static dielectric constant, ε_∞ is the high-frequency dielectric constant, and ω_{LO} and ω_{TO} are the angular frequencies of the LO and TO phonons, respectively. This relation underscores the influence of lattice vibrations on the dielectric properties of polar materials [35]. This relation is valid under the assumption that the crystal is a polar dielectric with at least two atoms in the basis, resulting in long-range Coulomb interactions, the ions are treated within the harmonic approximation, only one dominant infrared-active optical phonon mode is present, the material is non-magnetic and insulating (no free carriers), and local field effects and spatial dispersion are neglected.

1.3.2 Permittivity model for phononic materials

In polar dielectric crystals, such as SiO_2, AlN, or SiC, the basis contains at least two atoms of opposite charge. When these ions oscillate out of phase compared to each other under the influence of an electric field, they give rise to optical phonons.

The interaction of electromagnetic waves with optical phonons can be modeled using the Lorentz oscillator model [25, 35]. This classical approach considers the displacement of bound charges under an external electric field. The equation of motion for such a system is:

$$m\frac{d^2x}{dt^2} + m\gamma\frac{dx}{dt} + m\omega_0^2 x = -eE(t), \tag{1.15}$$

where m is the effective mass of the oscillator, γ is the damping constant, ω_0 is the natural frequency of the oscillator, e^* is the effective charge, and $E(t)$ is the time-dependent electric field. Assuming a harmonic time dependence $E(t) = E_0 e^{-i\omega t}$, the steady-state solution for the displacement $x(t)$ leads to a frequency-dependent polarization $P(\omega)$:

$$P(\omega) = Ne^*x(\omega) = \frac{N(e^*)^2}{m} \cdot \frac{1}{\omega_{\mathrm{TO}}^2 - \omega^2 - i\gamma\omega} \cdot E, \tag{1.16}$$

and consequently to the frequency-dependent dielectric function:

$$\varepsilon(\omega) = \varepsilon_\infty + \frac{S}{\omega_{\mathrm{TO}}^2 - \omega^2 - i\gamma\omega}, \tag{1.17}$$

where $S = \frac{N(e^*)^2}{\varepsilon_0 m}$ is the oscillator strength. By using the LST relation we can write $S = \varepsilon_\infty(\omega_{\mathrm{LO}}^2 - \omega_{\mathrm{TO}}^2)$ and hence the permittivity can be expressed as:

$$\varepsilon(\omega) = \varepsilon_\infty \left(1 + \frac{\omega_{LO}^2 - \omega_{\mathrm{TO}}^2}{\omega_{\mathrm{TO}}^2 - \omega^2 - i\gamma\omega}\right). \tag{1.18}$$

The above equation shows that the permittivity becomes negative in the interval $\omega_{\mathrm{TO}} < \omega < \omega_{\mathrm{LO}}$ known as the reststrahlen band. The optical properties of polar dielectrics across the reststrahlen band are determined by their frequency-dependent complex permittivity. To accurately describe the dielectric response associated with phonon resonances, various models have been developed based on the material's microscopic properties. The Lorentz oscillator model, introduced previously [Eq. (1.18)], provides a fundamental framework to capture the essential features of the dielectric function, particularly the resonance between the transverse optical (TO) and longitudinal optical (LO) phonon modes. This model is highly effective for ideal, crystalline materials with minimal structural disorder, such as bulk silicon carbide (SiC). However, for amorphous materials like silicon dioxide (SiO_2) or for thin films where disorder, inhomogeneous broadening, and microscopic structural variations are significant, the Lorentz model alone is insufficient to capture the observed broadening of phonon features [15, 36]. In such cases, more advanced formulations are needed to realistically model the optical response. One widely adopted approach is the Brendel–Bormann (BB) oscillator model, which introduces a Gaussian distribution of Lorentzian resonances to account for inhomogeneous broadening [15]. In this model, the dielectric function is expressed as:

$$\epsilon(\omega) = \epsilon_\infty + \sum_j \chi_j(\omega), \tag{1.19}$$

$$\chi_j(\omega) = \frac{1}{\sqrt{2\pi}\sigma_j} \int_{-\infty}^{\infty} \exp\left(-\frac{(x-\omega_{0j})^2}{2\sigma_j^2}\right) \frac{\omega_{pj}^2}{x^2 - \omega^2 - i\gamma_j\omega}\, dx, \tag{1.20}$$

where each oscillator j is characterized by a center frequency ω_{0j}, oscillator strength ω_{pj}, damping constant γ_j, and Gaussian width σ_j. This approach effectively models the effects of disorder and varying local environments on the optical phonon modes, which are particularly important in amorphous thin films.

In their comprehensive study, Kischkat *et al.* [15] employed the Brendel–Bormann model to fit ellipsometric measurements of mid-infrared optical properties of various thin film materials, including Al_2O_3, TiO_2, SiO_2, AlN, and Si_3N_4. For silicon dioxide, they extracted the high-frequency permittivity ϵ_∞ and the parameters for multiple Brendel oscillators, accurately capturing the complex multi-phonon structure observed experimentally. Their results demonstrated that the optical response of SiO_2 thin films could not be fully explained by a single Lorentzian oscillator but required a broadened oscillator model to account for the observed spectral features, such as the two prominent zero-crossings in $\mathrm{Re}(\epsilon)$ corresponding to the LO phonon at approximately 8.23 μm and the TO phonon at approximately 9.33 μm.

In summary, while the Lorentz model provides a basic description of phonon-polariton resonances in ideal polar crystals, modeling real-world materials, particularly thin films and amorphous phases, requires more sophisticated approaches such as the Brendel–Bormann model. The choice of model depends on the degree of structural disorder, material anisotropy, and the specific spectral features being investigated. Considering the above and the fact that the permittivity of subwavelength thin film of phononic material could be modified compared to their bulk version, ellipsometery measurements were performed to provide the permittivity values of our samples and used that for our simulations presented in chapter 2.

1.3.3 Phonon polaritons

Coupled light–lattice excitations (phonon polaritons) enable sub-diffraction confinement and strong dispersion control in the mid/far-IR [13, 14, 37]. The interaction of electromagnetic waves with matter is a fundamental mechanism that governs diverse phenomena in optics, condensed matter physics, atomic physics, and astrophysics. When light propagates through a dielectric medium, it induces dipole moments in the constituent atoms or molecules. The resulting dipole density is referred to as the polarization, which—under the regime of weak electromagnetic fields—responds linearly to the electric field [38].

A classical approach to describe this interaction is the Lorentz oscillator model, where each dipole is modeled as a driven damped harmonic oscillator. This model effectively captures the linear optical response of materials under low-intensity illumination. However, near material resonances, the interaction between light and matter

can become strong enough to generate hybrid light–matter states known as polaritons. These arise from the coherent exchange of energy between photons and material excitations. In the strong coupling regime, the photonic and material modes become inseparable, giving rise to new eigenstates whose dispersion relations exhibit a characteristic avoided crossing. This behavior is a hallmark of polaritonic systems and is central to many emerging applications in nanophotonics and quantum optics [12, 13].

In polar dielectric materials, lattice vibrations involving oppositely charged ions give rise to optical phonon modes that can strongly interact with electromagnetic radiation in the infrared regime. These coupled excitations are known as phonon polaritons. These modes exhibit unique dispersion relations and can propagate along the interface of polar dielectrics over their reststrahlen band (similar to surface plasmon polaritons). These modes are central to engineered thermal emission [1, 39, 40, 41]. The dispersion relation for surface phonon-polaritons (SPhPs) at the interface between a polar dielectric and another medium (e.g., air) is given by:

$$k_{\parallel} = \frac{\omega}{c}\sqrt{\frac{\epsilon(\omega)}{\epsilon(\omega)+\epsilon_m}}, \tag{1.21}$$

where $k_{\parallel}$ is the in-plane wavevector, c is the speed of light in vacuum, $\epsilon(\omega)$ is the frequency-dependent dielectric function of the polar material, ϵ_m is the dielectric constant of the adjacent medium. Phase matching conditions are crucial for the efficient excitation of SPhPs. These conditions require that the momentum of the incident photon matches that of the phonon-polariton mode, which can be achieved through techniques such as prism coupling or grating structures.

1.4 Berreman and ENZ Modes in thin films

Electromagnetic modes in thin-film structures play a crucial role in nanophotonics. In a general case, consider a three-layer structure with a dielectric film (thickness d, permittivity $\varepsilon_2(\omega)$) sandwiched between two semi-infinite media with permittivities ε_1 and ε_3, shown in Fig. 1.1. Electromagnetic eigenmodes with real in-plane wavevector $k_{\parallel}$ and complex frequency ω satisfy [12, 42]:

$$1+\frac{\varepsilon_1 k_{z3}}{\varepsilon_3 k_{z1}} = i\tan(k_{z2}d)\left(\frac{\varepsilon_2 k_{z3}}{\varepsilon_3 k_{z2}}+\frac{\varepsilon_1 k_{z2}}{\varepsilon_2 k_{z1}}\right), \tag{1.22}$$

where

$$k_{zi}^2 = \varepsilon_i k_0^2 - k_{\parallel}^2, \quad k_0 = \frac{\omega}{c}, \quad i = 1, 2, 3.$$

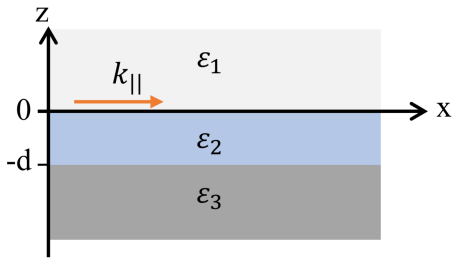

FIGURE 1.1: A three-layer structure containing a layer with thickness d and two semi-infinite regions.

Under specific material arrangement, where the permittivity of the thin film vanishes and $d \ll \lambda$, the solutions to Eq. (1.22) reveal two modes. One, a leaky, radiative resonance that lies within the light cone called Berreman mode. It produces a sharp absorption at frequencies where $\mathrm{Re}[\varepsilon_2(\omega)] \approx 0$, and can be directly excited by incident *p*-polarized (transverse magnetic) light [13]. The other, a non-radiative, confined resonance that lies outside the light cone called the ENZ mode. This mode is typically excited via evanescent coupling (e.g., prism or grating) [12]. Near the ENZ condition, the mode's dispersion flattens and the out-of-plane electric field E_z scales inversely with film thickness, indicating intense field confinement [12].

Phononic thin films naturally realize these behaviors near the LO phonon frequencies and have been observed in AlN, SiO_2, and related dielectrics [14, 16]. The ENZ/Berreman resonance does not occur at the TO phonon resonance, where the permittivity has a pole. For a thin film the normal displacement is continuous and forces a large internal normal field, producing the confined, largely non-radiative ENZ (Berreman) mode. As an example, the above dispersion relation is numerically solved for plasmonic thin film with the permittivity function represented by drude model $\varepsilon_2(\omega) = 1 - \frac{\omega_p^2}{\omega^2 + i\gamma\omega}$, with ω_p and γ being the plasma angular frequency and the damping, surrounded by free space ($\varepsilon_1 = \varepsilon_2 = 1$) [12]. Fig. 1.2 shows the solved dispersion diagram for different thin-film thicknesses. As observed in panel (a) an almost flat dispersion is observed around ω_p for 2-nm-thick plasmonic slab suspended in air. This mode is referred to as the epsilon-near-zero (ENZ) mode. Moreover, as depicted in the bottom panels, it is also shown that when the dispersion curve lies within the ENZ mode region, indicated by the shaded gray area, the electric field remains relatively uniform throughout the slab.

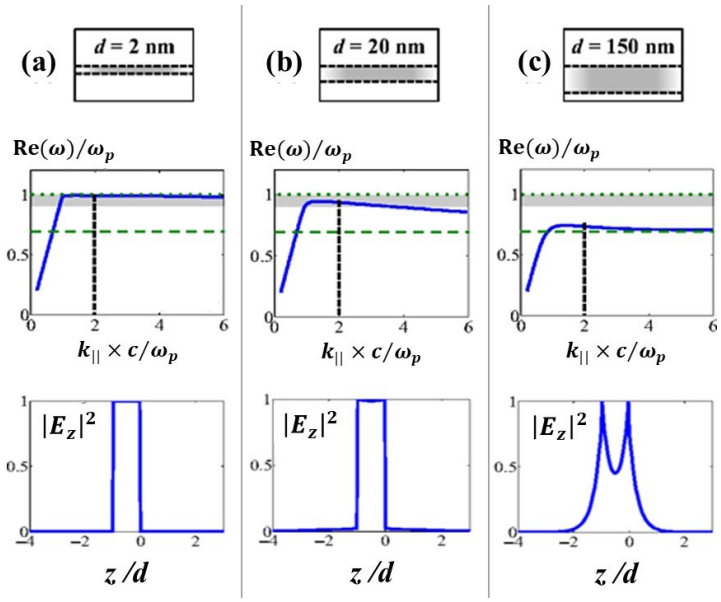

FIGURE 1.2: Dispersion (middle row) and profile of the intensity of the z component of the electric field vs the spatial variable z normalized by the thickness d computed at $k_{\|} = 2\omega_p/c$ (bottom row) for the long-range SPP supported by a (a) 2-nm-thick, (b) 20-nm-thick, and (c) 150-nm-thick layer surrounded by free space. In the dispersion graphs, the shaded gray area describes the ENZ mode validity range. $|E_z|^2$ is normalized to the maximum value. When the dispersion curve does not lie within the ENZ mode validity range, the field is not constant inside the layer. Adapted from [12] with permission.

Polar dielectrics such as SiO_2, Al_2O_3, and SiC exhibit a natural-occurring ENZ condition near their longitudinal optical (LO) phonon frequency, with $\mathrm{Re}[\varepsilon_2(\omega_{\mathrm{LO}})] \approx 0$ and relatively low loss [13, 23]. It is shown that these materials support both Berreman and ENZ phonon-polariton modes, similar to plasmonic ENZ systems. In thin films or slab geometries, the polariton behavior significantly differs due to confinement and boundary conditions. Notably, LO phonon modes, which are purely longitudinal in bulk and thus not directly excitable by transverse light, can be excited in thin films under specific conditions. In such films, the dielectric function $\varepsilon(\omega)$ exhibits a strongly dispersive behavior near the optical phonon frequencies according to Eq. 1.18. And, within the reststrahlen band, bulk propagation is forbidden, but surface or guided modes may exist governed by Eq. 1.21. In the thin-film geometry, the boundary conditions at the film interfaces lead to additional modes not present in the bulk. These include surface phonon polaritons (SPhPs) and hybridized guided modes whose dispersion relations differ from the single interface. Crucially, the highest-energy guided mode asymptotically approaches ω_{LO} at large in-plane wavevector $k_{\|}$. This behavior was detailed by Vassant et al. [13], who analyzed the polariton dispersion in ultra-thin

polar films. In contrast to plasmonic ENZ films (e.g., ITO), polar dielectrics offer low-loss behavior in the mid-infrared (mid-IR) and far-IR regimes [18, 43]. As an example, the mentioned three-layer structure is solved for a phononic material and the surface polariton modes are depicted in Fig. 1.3. When a surface phonon polariton (SPhP) propagates along the interface between air and a polar dielectric, its dispersion extends from the transverse optical (TO) phonon frequency ω_{TO}, up to a cutoff frequency ω_{S}, as shown by the green curve. For film thicknesses $d < \lambda/2$, where λ is the free-space wavelength, the SPhP dispersion splits into symmetric and antisymmetric branches (indicated in orange), with the separation increasing as the film becomes thinner. In the ultrathin limit ($d < \lambda/100$), the upper branch is pushed toward the longitudinal optical (LO) phonon frequency, ω_{LO} (shown in light blue), where the permittivity of the material naturally approaches zero. This symmetric mode is the epsilon-near-zero (ENZ) mode emerging in polar dielectrics in the mid-IR/NIR/FIR spectrum [12, 13].

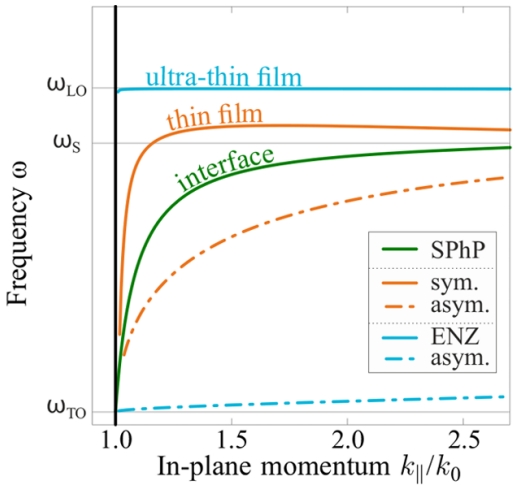

FIGURE 1.3: Surface phonon polaritons and epsilon-near-zero modes. The green curve shows a SPhP propagating at a single interface of air and a polar crystal emerging from the transversal optical phonon frequency ω_{TO} up to a cutoff frequency ω_{s}. For film thicknesses $d < \lambda/2$, where λ is the free-space wavelength, the SPhP dispersion splits into symmetric and antisymmetric branches (indicated in orange). In the ultrathin limit ($d < \lambda/100$), the upper branch is pushed toward the longitudinal optical (LO) phonon frequency, ω_{LO} (shown in light blue), where the permittivity of the material naturally approaches zero. This symmetric mode is therefore referred to as the epsilon-near-zero (ENZ) mode. Adapted from [23] with permission.

Early instances of coherent thermal emission were reported by Greffet *et al.*, who demonstrated spectrally and directionally selective emission from a SiC grating structure in the mid-infrared [40]. This coherence arose from grating-assisted coupling

of the surface phonon polaritons (SPhPs) to the far field, resulting in highly directional, narrowband thermal radiation. Building on the role of optical phonons in polar materials, Nordin *et al.* investigated coupling to the Berreman mode in ultra-thin aluminum nitride (AlN) films. Their work showed that these films support high-Q modes in the mid-IR, which was shown in both emissivity and reflectivity features [16]. Further insights into anisotropic thermal emitters were provided by Shin *et al.*, who studied individual hexagonal boron nitride (hBN) nanoribbons acting as directional mid-IR thermal antennas. They observed far-field spectral sharpening and directionality from deeply subwavelength structures and introduced the concept of a "coherent enhancement factor" to quantify the degree of coherence in thermal radiation [44]. The majority of recent approaches attribute the unique spectral and angular properties of thermal emission in polar dielectrics to the excitation of surface phonon polaritons (SPhPs). These hybrid light–matter modes enable sub-diffraction confinement and are responsible for enhanced emission characteristics in various 2D and nanostructured systems [37, 45].

1.5 Surface plasmon polaritons, gap plasmons, and gap-plasmon antennas

In this section, we introduce the gap-plasmon modes that are used in chapters 3 and 4 to study their coupling to the ENZ mode of an aluminum oxide thin film. Hybridizing localized plasmonic resonances with ENZ modes has garnered significant attention in recent years, especially within the visible to near-IR spectral ranges for plasmon-based materials like graphene and transparent conducting oxides such as indium tin oxide (ITO) [46, 47, 48, 49, 50]. In contrast, our work targets phonon-induced ENZ modes in the mid-infrared regions. This shift into the mid-IR is motivated by the rich phonon-polariton behavior of polar dielectric materials like Al_2O_3, where the dielectric function crosses zero near the longitudinal optical phonon frequency with negligible loss.

Surface plasmon polaritons (SPPs) are modes bound to a metal–dielectric interface that propagate along the surface as transverse magnetic waves (electric field oriented along the y-axis) that decay exponentially into both the metal and dielectric media. The dispersion relation for a SPP propagating along a metal–dielectric interface is

given by [42]:

$$k_{\mathrm{SPP}} = k_0 \sqrt{\frac{\varepsilon_m \varepsilon_d}{\varepsilon_m + \varepsilon_d}}, \tag{1.23}$$

where ε_m and ε_d denote the frequency-dependent permittivity of the metal and dielectric materials, respectively. Now, if we consider having two metal-dielectric boundaries like a metal-insulator-metal (MIM) structure, with sufficiently small gap area between the metal surfaces, the SPP modes can interact with each other and a mode called gap surface plasmons (GSPs) is created. Gap surface plasmons are highly confined electromagnetic modes that travel within dielectric gaps sandwiched between two metal surfaces, Fig. 1.4. When the gap thickness is much smaller than the wavelength, the mode becomes tightly confined, showing large wave vectors, slow group velocities, and intense local fields at the metal–dielectric interface [21, 51]. The extreme confinement and reduced mode volume associated with GSPs make them highly attractive for enhancing light–matter interaction in optical applications. The dispersion relation of the symmetric gap surface plasmon mode in a MIM waveguide is given by [52]:

$$\tanh\left(\frac{k_d w}{2}\right) = -\frac{\varepsilon_d k_y^m}{\varepsilon_m k^d{}_y}, \tag{1.24}$$

where t is the thickness of the dielectric gap, and

$$k_d = \sqrt{{k_{GSP}}^2 - k_0^2 \varepsilon_d}, \quad k_m = \sqrt{{k_{GSP}}^2 - k_0^2 \varepsilon_m},$$

are the transverse wavevectors in the dielectric and metal, respectively. Here, k_{GSP} is the propagation constant of the GSP mode, and $k_0 = \omega/c$ is the free-space wavevector.

Gap-plasmon antennas are similarly MIM nanostructures comprising a patterned metallic patch (such as a disk, square or bow-tie) separated from a metallic ground plane (optical reflector) by a thin dielectric spacer. Such antennas support resonant gap-plasmon modes [21, 52]. The resonance condition depends on the dimensions of the patch, the spacer thickness, and the permittivity of the material. These antennas exhibit strong electric field localization within the gap, producing high absorption and enabling sensitive refractive-index sensing and enhanced nonlinear interactions [51, 53]. In particular, bow-tie configurations yield field enhancements of several orders of magnitude within the small gap regions [21, 52].

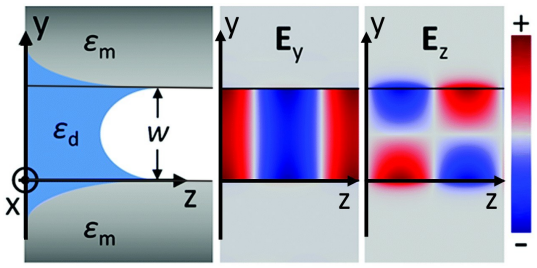

FIGURE 1.4: Illustration and numerically solved field components of a symmetric GSP mode propagating along the z-axis supported by two metal surfaces with a dielectric gap of width w between. The light blue color shows the electric field distribution; the corresponding electric field has its normal component, E_y, maintaining the same sign across the gap with an even-symmetric profile, whereas the tangential component, E_z, consequently exhibits an odd-symmetric profile. The calculated electric fields were obtained with the aid of finite-element method simulations (scale normalized for clarity) using gold surfaces with an air gap of width w = 0.5 μm at λ = 775 nm (nm = 0.174 + 4.86i). Adapted from [51] with permission.

Recent studies have explored hybrid architectures that combine gap-plasmon antennas with ENZ materials, including both plasmonic ENZ (e.g. ITO) and phonon-induced ENZ dielectrics (e.g., SiO_2, Al_2O_3) [22, 53]. When a subwavelength ENZ layer is inserted into the antenna gap, strong coupling between the gap-plasmon mode and the ENZ mode gives rise to polaritonic hybrid modes, characterized by resonance splitting (also known as vacuum Rabi splitting), avoided crossings, and enhanced electromagnetic fields [22, 53]. For example, Guo *et al.* observed flat-top, broadband absorption in a gold-nanodisk MIM stack by integrating a 12-nm-thick ITO ENZ layer, demonstrating strong coupling and field enhancement [53]. And, Yoo *et al.* reported ultrastrong coupling between TO phonon-polariton modes in SiO_2 and ENZ gap-plasmon nanocavity modes, achieving normalized coupling rates $\eta > 0.25$ and splitting up to 50% of the mode frequency [22]. These hybrid systems not only enable strong mode confinement and field enhancement but also provide a platform for mid-IR nonlinear optics, coherent thermal emission, and tunable absorption.

1.6 Thesis Structure

This thesis is organized into four chapters. The core experimental work of the thesis is presented in chapter 2. It explores the thermal emission properties of SiO_2 thin films. Spectral measurements in the mid-infrared regime reveal sharp emission features, with improved temporal coherence. Our results are consistent with the numerical simulation. The role of the ENZ condition and the impact of film thickness, angle

of incidence, and polarization are systematically investigated. A detailed description of the numerical simulation methodology is provided in Appendix A

Chapter 3 presents a theoretical and numerical study of a strongly coupled system composed of a gold gap-plasmon antenna integrated with an ultra-thin ENZ film. Using finite-difference time-domain (FDTD) simulations, we demonstrate that hybridization between the localized gap-plasmon resonance and the ENZ phonon polariton leads to the formation of upper and lower polariton branches. The characteristic anti-crossing behavior is used to extract the coupling strength and resonance splitting as a function of gold patch widths and ENZ layer thickness. This strongly coupled system is shown to exhibit dispersion engineering capabilities with potential applications in infrared optics and photonic devices. A detailed description of the numerical simulation methodology is provided in Appendix A

Building on the findings of chapter 3, chapter 4 investigates the electric field enhancement associated with the hybrid modes in the ENZ-coupled system. By calculating the spatial distribution and magnitude of the electric field at both upper and lower polariton resonances, we evaluate the local field intensity as a function of ENZ film thickness. The simulations reveal orders-of-magnitude enhancement inside the ENZ film, particularly for films thinner than 20 nm. These results are critical for understanding and exploiting nonlinear optical effects, such as second- and third-harmonic generation, where the nonlinear polarization scales with the local field.

The thesis concludes with a summary of the key findings, their implications for future nanophotonic and thermal technologies, and a discussion of possible extensions. In addition to the central research presented in the main chapters, Appendix A describes a nonlinear characterization setup that I constructed to support ongoing and future studies in nonlinear optics within our group.

References

[1] Denis G. Baranov et al. "Nanophotonic engineering of far-field thermal emitters". In: *Nature Materials* 18.9 (2019), pp. 920–930. DOI: 10.1038/s41563-019-0363-y.

[2] Michela F. Picardi, Kartika N. Nimje, and Georgia T. Papadakis. "Dynamic modulation of thermal emission—A Tutorial". In: *Journal of Applied Physics* 133.11 (2023), p. 111101. DOI: 10.1063/5.0089223.

[3] Max Planck. *The theory of heat radiation*. Blakiston, 1914.

[4] G. T. Papadakis et al. "Deep-subwavelength Thermal Switch via Resonant Coupling in Monolayer Hexagonal Boron Nitride". In: *Physical Review Applied* 15 (2021), p. 054002. DOI: 10.1103/PhysRevApplied.15.054002.

[5] Bosai Lyu et al. "Phonon Polariton-assisted Infrared Nanoimaging of Local Strain in Hexagonal Boron Nitride". In: *Nano Letters* 19.3 (2019), pp. 1982–1989. DOI: 10.1021/acs.nanolett.8b05166.

[6] Alireza Shahsafi et al. "Mid-infrared Optics Using Dielectrics with Refractive Indices Below Unity". In: *Phys. Rev. Applied* 10 (3 Sept. 2018), p. 034019. DOI: 10.1103/PhysRevApplied.10.034019.

[7] A. B. Dajwi Shaik and P. Palla. "Optical quantum technologies with hexagonal boron nitride single photon sources". In: *Scientific Reports* 11.1 (2021), p. 12285. DOI: 10.1038/s41598-021-91364-x.

[8] S. J. U. White et al. "Electrical control of quantum emitters in a Van der Waals heterostructure". In: *Light: Science and Applications* 11.1 (2022), p. 186. DOI: 10.1038/s41377-022-00776-1.

[9] Marine Laroche et al. "Coherent thermal antenna using a photonic crystal slab". In: *Physical Review Letters* 96.12 (2006), p. 123903. DOI: 10.1103/PhysRevLett.96.123903.

[10] Yunbin Ying et al. "Whole LWIR Directional Thermal Emission Based on ENZ Thin Films". In: *Laser & Photonics Reviews* 16.8 (2022), p. 2200018. DOI: https://doi.org/10.1002/lpor.202200018.

[11] Andrea Alù et al. "Epsilon-near-zero metamaterials and electromagnetic sources: Tailoring the radiation phase pattern". In: *Phys. Rev. B* 75 (Apr. 2007), p. 155410. DOI: 10.1103/PhysRevB.75.155410. URL: https://doi.org/10.1103/PhysRevB.75.155410.

[12] Salvatore Campione, Igal Brener, and Francois Marquier. "Theory of epsilon-near-zero modes in ultrathin films". In: *Phys. Rev. B* 91.12 (2015), p. 121408. DOI: 10.1103/PhysRevB.91.121408.

[13] Simon Vassant et al. "Berreman mode and epsilon near zero mode". In: *Optics Express* 20.21 (2012), pp. 23971–23977. DOI: 10.1364/OE.20.023971.

[14] Joshua D. Caldwell et al. "Low-loss, infrared and terahertz nanophotonics using surface phonon polaritons". In: *Nanophotonics* 4.1 (2015), pp. 44–68. DOI: 10.1515/nanoph-2014-0007.

[15] Jan Kischkat et al. "Mid-infrared optical properties of thin films of aluminum oxide, titanium dioxide, silicon dioxide, aluminum nitride, and silicon nitride". In: *Applied Optics* 51 (2012), pp. 6789–6798. DOI: 10.1364/AO.51.006789.

[16] L. Nordin et al. "Mid-infrared epsilon-near-zero modes in ultra-thin phononic films". In: *Applied Physics Letters* 111.9 (Aug. 2017), p. 091105. ISSN: 0003-6951. DOI: 10.1063/1.4996213. eprint: https://pubs.aip.org/aip/apl/article-pdf/doi/10.1063/1.4996213/13139383/091105_1_online.pdf. URL: https://doi.org/10.1063/1.4996213.

[17] Eric Y. Ma et al. "The Reststrahlen Effect in the Optically Thin Limit: A Framework for Resonant Response in Thin Media". In: *Nano Letters* 22.20 (2022). PMID: 36112673, pp. 8389–8393. DOI: 10.1021/acs.nanolett.2c02819.

[18] M. Z. Alam, I. De Leon, and R. W. Boyd. "Large optical nonlinearity of indium tin oxide in its epsilon-near-zero region". In: *Science* 352.6287 (2016), pp. 795–797. DOI: 10.1126/science.aad3105.

[19] Sergei Mikhailovich Rytov and Herman Erkku. *Theory of electric fluctuations and thermal radiation*. Air Force Cambridge Research Center Bedford, MA, 1959.

[20] R. Kubo. "The fluctuation-dissipation theorem". In: *Reports on Progress in Physics* 29.1 (1966), p. 255. DOI: 10.1088/0034-4885/29/1/306.

[21] Fei Ding et al. "A review of gap-surface plasmon metasurfaces: fundamentals and applications". In: *Nanophotonics* 7.6 (2018), pp. 1129–1156. DOI: 10.1515/nanoph-2017-0125.

[22] Daehan Yoo et al. "Ultrastrong plasmon–phonon coupling via epsilon-near-zero nanocavities". In: *Nature Photonics* 15 (2021), pp. 125–130. DOI: 10.1038/s41566-020-00731-5.

[23] Nikolai Christian Passler et al. "Strong Coupling of Epsilon-Near-Zero Phonon Polaritons in Polar Dielectric Heterostructures". In: *Nano Letters* 18.7 (2018). PMID: 29894195, pp. 4285–4292. DOI: 10.1021/acs.nanolett.8b01273.

[24] Larry A. Coldren, Scott W. Corzine, and Milan L. Mašanović. *Diode Lasers and Photonic Integrated Circuits*. 2nd. Hoboken, NJ: Wiley, 2012. ISBN: 978-0470484128.

[25] J. M. Ziman. *Principles of the Theory of Solids*. Cambridge: Cambridge University Press, 1972. DOI: 10.1017/CBO9781139644075. URL: http://dx.doi.org/10.1017/CBO9781139644075.

[26] T. G. Folland, L. Nordin, and D. Wasserman. "Probing polaritons in the mid- to far-infrared". In: *Journal of Applied Physics* 125.19 (2019), p. 191102. DOI: 10.1063/1.5085824.

[27] Komron J Shayegan et al. "Direct observation of the violation of Kirchhoff's law of thermal radiation". In: *Nature Photonics* 17.10 (2023), pp. 891–896.

[28] Bo Zhao et al. "Near-complete violation of Kirchhoff's law of thermal radiation with a 0.3 T magnetic field". In: *Optics Letters* 44.16 (2019), pp. 4203–4206. DOI: 10.1364/OL.44.004203.

[29] M. Zahirul Alam, Israel De Leon, and Robert W. Boyd. "Large optical nonlinearity of indium tin oxide in its epsilon-near-zero region". In: *Science* 352.6287 (2016), pp. 795–797. DOI: 10.1126/science.aae0330. URL: https://www.science.org/doi/abs/10.1126/science.aae0330.

[30] Yaliang Gui et al. "Towards integrated metatronics: a holistic approach on precise optical and electrical properties of Indium Tin Oxide". In: *Scientific Reports* 9.1 (2019), p. 11279. ISSN: 2045-2322. DOI: 10.1038/s41598-019-47631-5. URL: https://doi.org/10.1038/s41598-019-47631-5.

[31] Yiyu Wang and colleagues. "Broadband frequency translation through time refraction in indium–tin-oxide epsilon-near-zero films". In: *Nature Communications* 11 (2020). DOI: 10.1038/s41467-020-15682-2.

[32] Sebastian A. Schulz et al. "Roadmap on photonic metasurfaces". In: *Applied Physics Letters* 124.26 (June 2024), p. 260701. ISSN: 0003-6951. DOI: 10.1063/5.0204694. URL: https://doi.org/10.1063/5.0204694.

[33] Orad Reshef et al. *Nonlinear optical effects in epsilon-near-zero media*. 2019. DOI: 10.1038/s41578-019-0120-5.

[34] Nikolai Christian Passler et al. "Strong Coupling of Epsilon-Near-Zero Phonon Polaritons in Polar Dielectric Heterostructures". In: *Nano Letters* 18.7 (2018). PMID: 29894195, pp. 4285–4292. DOI: 10.1021/acs.nanolett.8b01273.

[35] Charles Kittel. *Introduction to Solid State Physics*. 8th. Wiley, 2005.

[36] Daniel Franta et al. "Dispersion model for optical thin films applicable in wide spectral range". In: 9628 (2015). Ed. by Angela Duparré and Roland Geyl, 96281U. DOI: 10.1117/12.2190104.

[37] Nicholas Rivera, Teodor K. Christensen, and Prineha Narang. "Phonon Polaritonics in Two-Dimensional Materials". In: *Nano Letters* 19.4 (2019), pp. 2653–2660. DOI: 10.1021/acs.nanolett.9b00767.

[38] John David Jackson. *Classical Electrodynamics*. 3rd. Hoboken, NJ: John Wiley & Sons, 1999.

[39] Mariano Pascale, Maxime Giteau, and Georgia T. Papadakis. "Perspective on near-field radiative heat transfer". In: *Applied Physics Letters* 122.10 (Mar. 2023), p. 100501. ISSN: 0003-6951. DOI: 10.1063/5.0142651. eprint: https://pubs.aip.org/aip/apl/article-pdf/doi/10.1063/5.0142651/16773700/100501_1_online.pdf. URL: https://doi.org/10.1063/5.0142651.

[40] Jean-Jacques Greffet, Romain Carminati, and Jean-Pierre D. Joulain. "Coherent thermal emission of light by thermal sources". In: *Nature* 416.6876 (2002), pp. 61–64. DOI: 10.1038/416061a.

[41] Irfan Khan et al. "Vertical Thermal Emission from Optical Antennas on an Epsilon-Near–Zero Substrate". In: *Advanced Optical Materials* 12.25 (2024), p. 2400715. DOI: https://doi.org/10.1002/adom.202400715.

[42] Stefan A. Maier. *Plasmonics: Fundamentals and Applications*. New York: Springer, 2007. ISBN: 978-0-387-33150-8. DOI: 10.1007/978-0-387-37825-1.

[43] Orad Reshef et al. "Nonlinear optical effects in epsilon-near-zero media". In: *Nature Reviews Materials* 3 (2019), pp. 170–182. DOI: 10.1038/s41578-019-0120-5.

[44] Seungho Shin et al. "Far-field Coherent Thermal Emission from Polaritonic Resonance in Individual Anisotropic Nanoribbons". In: *Nature Communications* 10 (2019), p. 1377. DOI: 10.1038/s41467-019-09378-5. URL: https://doi.org/10.1038/s41467-019-09378-5.

[45] S. Ogawa, S. Fukushima, and M. Shimatani. "Extraordinary Optical Transmission by Hybrid Phonon–Plasmon Polaritons Using hBN Embedded in Plasmonic". In: *Journal of the Optical Society of America A* 14.4 (1997), pp. 741–755. DOI: 10.1364/JOSAA.14.000741.

[46] Mohammad Karimi et al. "Interactions of Fundamental Mie Modes with Thin Epsilon-near-Zero Substrates". In: *Nano Letters* 23.24 (2023). PMID: 38038228, pp. 11555–11561. DOI: 10.1021/acs.nanolett.3c03301. eprint: https://doi.org/10.1021/acs.nanolett.3c03301. URL: https://doi.org/10.1021/acs.nanolett.3c03301.

[47] Saumya Choudhary et al. "Strongly Coupled Plasmon Polaritons in Gold and Epsilon-Near-Zero Bifilms". In: *ACS Photonics* 10.1 (2023), pp. 162–169. DOI: 10.1021/acsphotonics.2c01412. eprint: https://doi.org/10.1021/acsphotonics.2c01412. URL: https://doi.org/10.1021/acsphotonics.2c01412.

[48] Saumya Choudhary et al. "Weak superradiance in arrays of plasmonic nanoantennas". In: *Phys. Rev. A* 100 (4 Oct. 2019), p. 043814. DOI: 10.1103/PhysRevA.100.043814. URL: https://link.aps.org/doi/10.1103/PhysRevA.100.043814.

[49] Yu Liu and R. F. Willis. "Plasmon-phonon strongly coupled mode in epitaxial graphene". In: *Phys. Rev. B* 81 (8 Feb. 2010), p. 081406. DOI: 10.1103/PhysRevB.81.081406. URL: https://link.aps.org/doi/10.1103/PhysRevB.81.081406.

[50] Maureen J. Lagos et al. "Imaging Strongly Coupled Plasmon–Phonon Modes in Mid-Infrared Double Antennas". In: *ACS Photonics* 8.5 (2021), pp. 1293–1300. DOI: 10.1021/acsphotonics.1c00335.

[51] Randall A. Smith, N. Asger Mortensen, and Sergey I. Bozhevolnyi. "Gap and channelled plasmons in tapered grooves: a review". In: *arXiv preprint arXiv:1503.00554* (2015).

[52] Randall A. Smith, N. Asger Mortensen, and Sergey I. Bozhevolnyi. "Gap and channelled plasmons in tapered grooves: a review". In: *arXiv preprint arXiv:1503.00554* (2015). Also covers bow-tie antennas.

[53] Junpeng Guo et al. "Coupling of epsilon-near-zero mode to gap plasmon mode for flat-top wideband perfect light absorption". In: *ACS Photonics* (2018). DOI: 10.1021/acsphotonics.7b01491.

Chapter 2

Coherence in mid-infrared thermal emission from silicon dioxide under epsilon-near-zero conditions

2.1 Contribution Statement

Epsilon-near-zero (ENZ) media offer a powerful route to manipulate light–matter interactions by exploiting regimes where the real part of the permittivity approaches zero. Within our research group, ENZ phenomena had previously been investigated primarily in plasmonic transparent conducting oxides such as indium tin oxide (ITO), with emphasis on optical effects in the visible and near-infrared regimes. In contrast, this manuscript experimentally explores a fundamentally different ENZ platform based on phonon-polaritonic response in naturally occurring polar dielectrics. Unlike plasmonic ENZ materials, which typically require carrier doping and electrical/chemical tuning, polar dielectrics exhibit intrinsic ENZ conditions near their longitudinal optical (LO) phonon frequencies. These ENZ points arise without extrinsic doping and naturally occur in the mid-IR, a spectral window central to thermal photonics, chemical sensing, and free-space infrared technologies. Motivated by this distinction, and upon joining Prof. Robert W. Boyd's group, I was assigned to initiate a new line of research in the mid-IR spectrum focused on phonon-induced ENZ material to answer the question of "could the phonon-induced ENZ provide coherence in the thermal emission?" While engineered plasmonic ENZ systems had demonstrated striking dispersion engineering for driven (externally illuminated) responses. I then suggested the necessity of using ultra-thin, phononic ENZ films to shape spontaneous, thermally generated radiation—particularly with respect to coherence which is reported

in our manuscript.

This project was done under expert guidance and technical discussions provided by Dr. Jeremy Upham, Dr. R. Margoth Córdova-Castro, Dr. M. Zahirul Alam, Prof. Gerd Leuchs, and Prof. Robert W. Boyd. My contribution in the project is as follows. I proposed using subwavelength structure, performed the simulations, designed the samples, designed and conducted the experiments, developed the scientific narrative and interpreting the results, and wrote the first draft of the manuscript. Sample fabrication and provision was carried out at the Max Planck Institute for the Science of Light by Dr. Florentina Gannott and Prof. Gerd Leuchs.

This project represents the first mid-IR experimental study conducted in our lab, requiring extensive preparation, instrumentation development, and conceptual groundwork. I played a leading role in the acquisition and integration of key laboratory infrastructure, including a Fourier-transform infrared (FTIR) spectrometer, thermal controller, and polarization-resolved detection optics, all of which required research and technical discussion with providers to finalize our choices. I also designed a custom thermal control sample mounting stage built for stable and repeatable angle and temperature-dependence measurements of the thermal emission from samples with minimal contribution from the thermal background. In particular, the project began during the COVID-19 quarantine period, which caused logistical challenges. Despite these obstacles, we pushed forward with simulations, equipment handling, and code development to ensure the project's continuity. In the early phase of the study, I evaluated several candidate materials—such as hexagonal boron nitride (hBN), bulk silicon carbide (SiC), and bulk quartz—through both electromagnetic simulations and preliminary measurements. We finally chose silicon dioxide (SiO_2) as the most promising material due to its well-defined ENZ condition in the mid-IR and wide accessibility, I designed a series of samples with subwavelength thicknesses. I conducted full-wave electromagnetic simulations using COMSOL to predict emission characteristics and field distributions, and then performed angle-resolved and polarization-resolved emissivity measurements under different temperatures. I also developed codes to analyze the data and extract emissivity spectra from raw emission measurements. The resulting measurements revealed narrowband thermal emission peaks with quality factors exceeding 27 in 30 nm-thick SiO_2 films, confirming the emergence of partially coherent thermal radiation governed by ENZ physics.

This project not only established a new experimental capability within our group

but also revealed new insights into the interplay between phonon-polaritonic modes and thermal radiation in ENZ systems. The work forms a cornerstone of this thesis and provides a foundational platform for future exploration of ENZ-enhanced thermal photonics and infrared sensing technologies.

Coherence in mid-infrared thermal emission from silicon dioxide under epsilon-near-zero conditions

Maryam Abbasi[1*], M. Zahirul Alam[2†], Jeremy Upham[2†], R. Margoth Córdova-Castro[2†], Florentina Gannott[3†], Gerd Leuchs[2,3,4,5†], Robert W. Boyd[1,2,6†]

[1*]Department of Electrical Engineering, University of Ottawa, Ottawa, K1N6N5, ON, Canada.
[2]Department of Physics, University of Ottawa, Ottawa, K1N7N9, ON, Canada.
[3]Max-Planck-Institut für die Physik des Lichts, Erlangen, 91058, Germany.
[4]Max Planck Society - University of Ottawa Centre for Extreme Quantum Photonics, Erlangen, 91058, Germany.
[5]Institut für Optik, Information und Photonik, University Erlangen-Nuremberg, Erlangen, 91058, Germany.
[6]Department of Physics, University of Rochester, Rochester, 14627, New York, USA.

†

Abstract

We observe coherent thermal emission from ultra-thin phononic materials in the mid-infrared. We harness the phononic dispersion of a poly-crystalline silicon dioxide polar crystal in an ultra-thin structure to produce sharp coherent emission features near the longitudinal optical phonon wavelengths with a spectral quality factor of Q=27. We explore this phenomenon in 300, 90, and 30-nm-thick films of silicon dioxide deposited on Si substrates. The emission of the samples are experimentally explored for different temperatures and polarizations using Fourier-transform infrared spectroscopy. We describe how this condition facilitates channeling the thermal energy given to the system into preferential emission over a narrow spectral range.

Keywords: Thermal emission, Polar dielectrics, Epsilon Near Zero, Ultra-thin

1 Introduction

In recent years, the conventional understanding of thermal emission has been challenged, triggering a surge in research to tailor emissions for specific temporal, spectral, and directional characteristics, along with enhanced quality factors (Q-factors). Notably, instances of violating Kirchhoff's law and achieving super-Planckian radiation in the near field are observed, thanks to the disruption of the assumptions underlying those well-established laws [1–4]. These breakthroughs not only reveal the untapped potential of the underlying physics, especially in the infrared spectrum, but also herald photonic-based devices that were previously hindered by temperature constraints. These advancements pave the way for transformative applications, including enhanced energy conversion in thermophotovoltaic systems, bio/chemical sensing, advanced light emission technologies, light sources for infrared photonics, and innovative approaches to passive radiative cooling[5–12].

Despite extensive exploration of near-field thermal emission, achieving strong coherent emission in the far-field remains a significant challenge [13–16]. Early instances of coherent emission by a SiC grating have been reported, featuring a narrow spectral and angular range [17]. Recently, again for laterally structured thin films, highly directional emission normal to the surface was reported by coupling the antenna resonance mode to the Berreman mode of the epsilon-near-zero (ENZ) material - materials where the real part of the permittivity crosses zero at specific wavelengths [18]. Another notable research demonstrated enhanced emissivity, as compared to laterally unstructured ultra-thin films, in the far field at low temperatures ranging from 100 K to 400 K by exploiting surface phonon polaritons (SPhP) in a single nanoribbon of silicon dioxide polar dielectric, with a width comparable to the wavelength [19]. Additionally and most remarkably, an investigation into the coupling to a Berreman mode was also made for a thin film of AlN showing a narrow spectral emission feature even though the thin film was not laterally structured [20]. The majority of proposed approaches attribute the unique properties of thermal emission to the excitation of SPhPs [21–23].

Phonon polaritons, excited across the reststrahlen band of polar dielectrics, present a compelling avenue for achieving extreme light-matter interaction [22, 24]. In the mid-infrared spectrum, the permittivity of polar dielectrics is predominantly governed by longitudinal optical (LO) and transverse optical (TO) phonon resonances, well-fitted with a Lorentzian model [25]. These materials exhibit two distinct wavelengths where a plot of the real part of the permittivity crosses zero, which occur at the wavelengths of the LO and TO phonons., originated from out-of-phase oscillations of ions with opposite charges within the crystal's primitive cells. Thanks to their intrinsic optical characteristic in the infrared spectrum, they obviated the need for using degenerate metal-oxides and the ensuing drawbacks of free carriers. Furthermore, unlike plasmon polaritons, which are hindered by significant losses and are primarily confined to surfaces, phonon polaritons not only exhibit a longer lifetime, but volume-confined phonon polaritons can also exist within the material under specific conditions, with anisotropic materials serving as a prime example where this behavior can be accommodated [26, 27].

Epsilon-near-zero materials, distinguished by a vanishing real part of the permittivity, hold significant promise for enabling coherent thermal emission[28, 29]. The unique property of ENZ materials, featuring a significantly large propagation wavelength within the material and near-zero phase velocity, sets the stage for exploring their impact on the coherence of thermal emission from polar materials in the far-field, specifically in the mid-infrared spectrum [28]. Traditionally, thermal radiation from a material is anticipated to be unpolarized, temporally and spatially incoherent, and spectrally broadband. This work investigates how phonon-induced ENZ behavior in polar dielectrics influences far-field thermal emission from ultra-thin silicon dioxide films.

We harness the ENZ properties of silicon dioxide polar dielectrics and demonstrate the importance of laterally unstructured ultra-thin films as a key design feature to obtain coherent and narrow-band thermal emission in the mid-infrared spectrum.

2 Results

Fig. 1 presents the numerical results for the spectral and angular absorptance for a thick layer of silicon dioxide (a,b), and for silicon dioxide films with thicknesses of 300 nm (c,d), 90 nm (e,f), and 30 nm (g,h) deposited on a Si substrate. For the bulk silicon dioxide shown in Fig. 1 (a,b), the material is non-transparent within the Reststrahlen band, primarily reflecting or absorbing light due to its interactions with phonon resonances. The absorptive behavior is broadband across this band due to the overlap of multiple phononic oscillations mainly around $\lambda = 8.23$ μm associated with LO phonons, and others at $\lambda = 8.5$ μm and $\lambda = 9.33$ μm, corresponding to TO phonons for normal incidence ($\theta = 0°$). The angular dependence of the absorptance spectra for all samples follows the complex Fresnel reflection coefficients, which depend on the polarization state of light reflected from the surface at non-normal incidence. For the thin films under TE-polarized illumination, Fig. 1 (c,e,g), strong absorption peaks near $\lambda = 9.33$ μm and a weaker feature at $\lambda = 8.5$ μm are clearly distinguishable, both attributed to TO phonons. The absorptance spectra decrease with increasing angle of incidence, due to the corresponding rise in surface reflectivity for TE modes. In contrast, for TM-polarized light Fig. 1 (d,f,h), a prominent absorption peak appears at a higher energy near $\lambda = 8.23$ μm, corresponding to LO phonons. The peak close to the LO phonon wavelength emerges only under TM polarization and at larger angles of incidence, where the tangential component of the incident electric field can couple to the dipole moments oscillating in the plane of the surface. As expected, longitudinal phonon modes cannot be excited under TE-polarized light. Furthermore, the relative peak amplitude of the resonance close to the LO at $\lambda = 8.23$ μm to the one at TO $\lambda = 9.33$ μm increases as the thickness of the oxide layer decreases from 300 nm to 30 nm. Moreover, as the oxide layer thickness decreases, the absorptance spectrum near the LO phonon resonance features a sharper peak, likely due to the confinement of ionic charge oscillations in the out of plane direction relative to the sample surface. This confinement reduces phonon-phonon scattering, leading to a higher quality factor for the resonance. The maximum absorptance at the LO phonon resonance shifts from angles between 60° to 80° as the film thickness decreases from 300 nm to 30 nm.

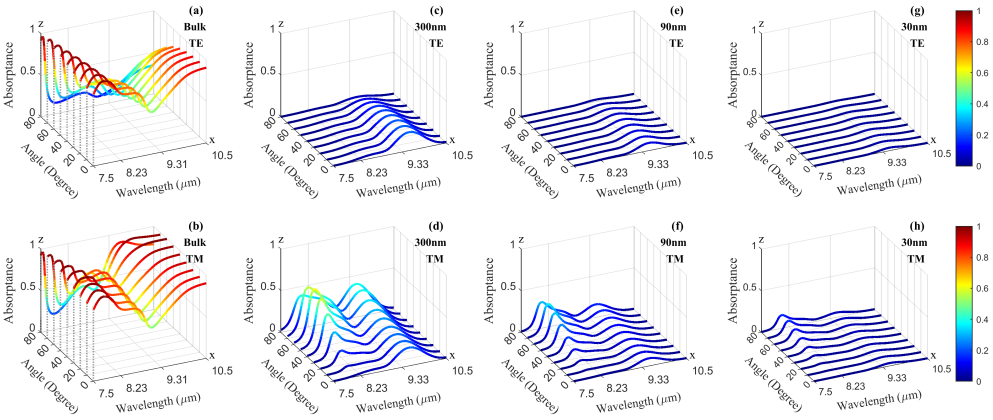

Fig. 1 Numerical results showing the absorptance spectra for a thick layer of (bulk) silicon dioxide (a,b) and silicon dioxide films of 300 nm (c,d), 90 nm (e,f), and 30 nm (g,h) thickness on 2-mm-thick Si substrate under the illumination of TE (top row) and TM (bottom row) polarized light, for incident angle, from 0° to 80°. Note that as the oxide layer decreases the absorptance shows sharper peaks at the LO whereas the peak at TO wavelengths is damped. The dotted gray lines connect individual curves to a specific angle of incidence on the Angle axis.

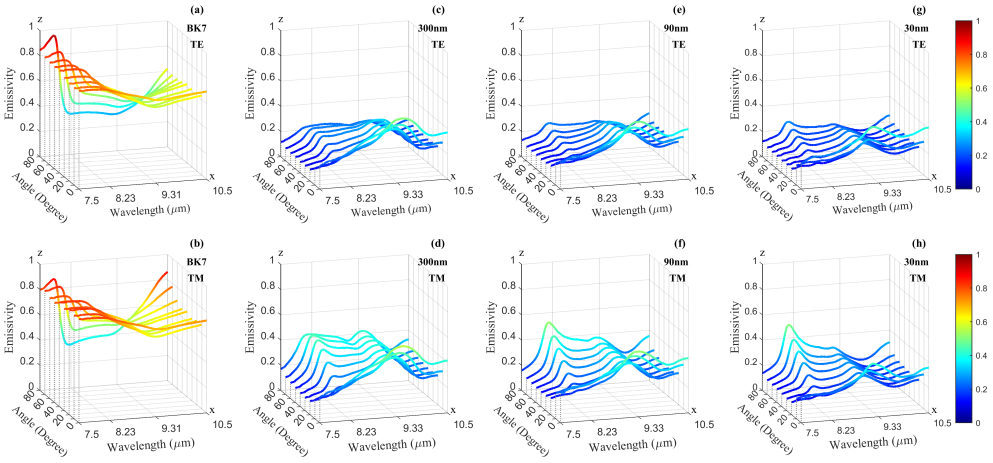

Fig. 2 Measurement results showing emissivity for thick layer of (bulk) silicon dioxide (a,b) and silicon dioxide films of 300 nm (c,d), 90 nm (e,f), and 30 nm (g,h) thickness on 2-mm-thick Si substrate for different angles of observation from 0° to 80°, having TE (top row) and TM (bottom row) characteristics. The dotted gray lines connect individual curves to a specific angle of incidence on the Angle axis.

To compare to our numerical predictions, we next characterized the spectral, angular and polarization of thermal emission from similar samples. Fig. 2 shows the measured emissivity for thick layer of silicon dioxide (a,b) and silicon dioxide films with the thickness of 300 nm (c,d), 90 nm (e,f), and 30 nm (g,h) on 2-mm-thick

Si substrate for different angles from 0° to 80°. Comparing the measured emissivity with the calculated absorption spectrum reported in Fig. 1, reveals a strong similarity between the two graphs for each sample (see Supplementary information for more detail). The graphs on the bottom pertain to the emissions with TM characteristic. As observed, two main emissivity peaks are present: one close to the LO phonons around $\lambda = 8.23$ μm and another near the TO phonon resonances around $\lambda = 9.5$ μm, which aligns with the absorption behavior reported earlier. Regarding angular dependence, the peak emerging around LO phonons at $\lambda = 8.23$ μm, reaches its maximum around 60° for TM polarized radiation with a half-width-at-half-maximum of 25° without any lateral structuring (see Fig. 2 (h)), whereas the maximum at $\lambda = 9.5$ μm occurs under perpendicular emission for TE polarized radiation. For TE polarization, the measured emissivity is consistent with the reported absorption behavior, and the observed peaks around the LO phonon resonances are attributed to polarization coupling. In the same vein, the peak amplitude ratio between the resonance and the TO peak at $\lambda = 9.5$ μm increases as the thickness of the oxide layer decreases from 300 nm to 30 nm. Additionally, as the film thickness decreases, a narrower emission spectrum close to the LO phonon resonance emerges. This behavior can be explained by the lattice dynamics of polar crystals over the Reststrahlen band [22, 30].

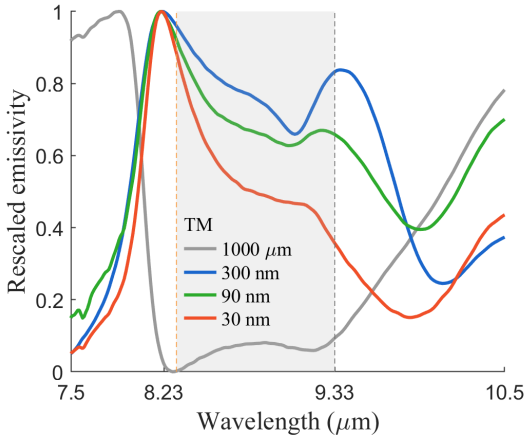

Fig. 3 Rescaled (see text) emissivity for thick layer of silicon dioxide and 300 nm, 90 nm, and 30 nm thin films of silicon dioxide on a 2-mm-thick Si substrate for TM polarizations at angles of 60°, 80° and 80°, respectively using a FTIR spectrometer. For each curve, the chosen angle is the one for which the emissivity shows the largest quality factor.

Fig. 3 illustrates the rescaled emissivity for 300 nm, 90 nm, and 30 nm thin films of silicon dioxide on a 2-mm-thick silicon substrate under TM polarization at angles of 60°, 80°, and 80°, respectively, at which the spectral features are sharpest. The emissivity data are rescaled over the whole range from 6 μm to 14 μm (not fully shown in Fig. 3 and 2) using the formula $\frac{\epsilon(\lambda,T,\theta)-\min(\epsilon(\lambda,T,\theta))}{\max(\epsilon(\lambda,T,\theta))-\min(\epsilon(\lambda,T,\theta))}$, which allows for a direct comparison of the emission profiles across different thicknesses (see Supplementary information for the comparison of the unscaled emissivity graphs). This rescaling

highlights the relative shape of the emissivity peaks while removing absolute intensity differences. A comparison of the rescaled emissivity for the ultra-thin samples reveals that as the oxide layer thickness decreases, the emissivity peaks at the LO phonon wavelength become significantly sharper ($8.23 + 0.55/-0.15$ μm), indicating a quality factor of about $Q = 27$ for the underlying de-convolved curve. In contrast, the peak at the TO phonon wavelength becomes more damped. Additionally, contrasting the emissivity of a thick silicon dioxide layer at 80° with that of the ultra-thin samples underscores the advantage of ultra-thin layers in achieving sharp, well-defined emission peaks, making them ideal for applications requiring high spectral selectivity. This result compares favorably to the earlier measurements by Nordin et al. who measured the thermal emission from a thin aluminum nitride layer of 100 nm thickness [20]. Our results on silicon dioxide in Fig. 2 show how this spectral feature develops as the thickness decreases, becoming more and more coherent. The quoted Q value refers to the thinnest sample and is about the same as the Q one can extract from Nordin et al. but in our case for the easily accessible material silicon dioxide [20].

3 Method

To explore coherent thermal emission at ENZ wavelengths from ultra-thin films of polar dielectrics, we investigate the emission spectra of silicon dioxide ultra-thin films deposited on an optically thick silicon (Si) substrate with a gold backing, using chemical vapor deposition. We compare this with a numerical simulation of the absorption spectrum. Note, that the Si substrate is non-polar supporting no optical phonons. The thermal radiation of the samples is measured experimentally and calculated numerically for different polarizations, sample orientations, and temperatures within the mid-infrared wavelength range.

3.1 Numerical Calculations

In accordance with Kirchhoff's law, which stipulates that the absorptivity and emissivity are equal for thermal emitters with materials satisfying Lorentz reciprocity. We present the absorptance of the samples calculated using the finite element method (FEM) in COMSOL. In the simulations, the samples are illuminated with transverse electric (TE) polarized light (top row) and transverse magnetic (TM) polarized light (bottom row), plane waves, with the convention shown in Fig. 5. The permittivity values of the samples are derived from ellipsometry measurements and used in simulations to ensure accuracy.

Fig. 4 shows the real and imaginary part of the relative permittivity of silicon dioxide thin films, derived from ellipsometry measurements of the samples; The minus sign in the imaginary part of the complex permittivity follows from the convention that the imaginary component of the permittivity causes the electric field to decay exponentially with $\exp\left(-i\frac{2\pi}{\lambda}\sqrt{\epsilon' - i\epsilon''}\, r\right)$ as the wave propagates through the medium in the r-direction, where $i^2 = -1$. Recently, Ma et al. measured the reflectance, R, under normal incidence, which is related to measuring the absorptance, A, and transmitance, T, based on $R + A + T = 1$, for the first time on a whole set of thin films with a wide

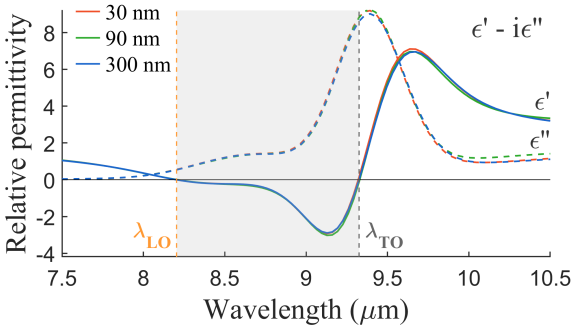

Fig. 4 Relative permittivity of silicon dioxide derived from ellipsometry measurements for samples with different silicon dioxide film thickness of 300 nm, 90 nm, and 30 nm on a 2-mm-thick Si substrate. As expected, the measured permittivity of the silicon dioxide shows only minuscule dependence for the mentioned thicknesses.

variation in thickness. We measured emission in a similar wide range of thicknesses but under varying angles, very different from and complementary to their work [30].

For each sample, two zero-crossings in the real part of the permittivity are observed: one near $\lambda = 8.23$ μm and another close to $\lambda = 9.33$ μm, corresponding to longitudinal and transverse optical (LO and TO) phonons, respectively. The ellipsometry data reveal that as the film thickness decreases, the zero crossing near the longitudinal wavelength remains almost unchanged. The triatomic structure of silicon dioxide leads to multiple TO and LO phonon resonances across the Reststrahlen band. However, the permittivity at the TO phonon frequency can be effectively modeled with a single Lorentz oscillator term near $\lambda = 9.33$ μm and $\lambda = 8.5$ μm [31]. Additionally, along with the primary LO phonon resonance at $\lambda = 8.23$ μm, weaker longitudinal oscillations appear at $\lambda = 8.37$ μm and $\lambda = 8.67$ μm. The contribution of each TO oscillation in the permittivity of the silicon dioxide thin-films can be well described with the Brendel oscillator model [31]. This model is useful for materials such as silicon dioxide, where the response is broadened due to inhomogeneous effects. The permittivity of the silicon dioxide films then can be represented with the following equations:

$$\epsilon(\nu) = \epsilon_\infty + \sum_{j=1}^{m} \chi_j(\nu) \tag{1}$$

$$\chi_j(\nu) = \frac{1}{\sqrt{(2\pi)}\sigma_j} \int_{-\infty}^{\infty} \exp\left[-\frac{(x-\nu_{0j})^2}{2\sigma_j^2}\right] \frac{\nu_{pj}^2}{x^2 - \nu^2 - i\nu_{\tau j}\nu} dx \tag{2}$$

where ν_{0j}, ν_{pj}, $\nu_{\tau j}$, and σ_j are the center frequency, the strength of the oscillator, the damping constant, and the standard deviation of the Gaussian distribution, respectively, for each oscillation mode, j.

3.2 Measurement

We confirm our argument through direct measurements of the emissivity of the samples. The emission spectra of the samples in the far field are measured directly using a

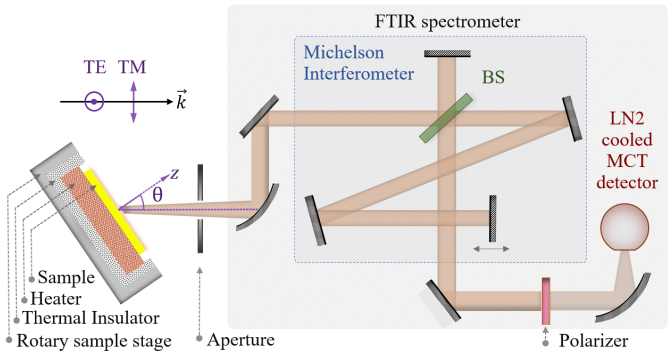

Fig. 5 Schematic of the experimental setup for direct measurement of emission for different angles, polarizations, and temperatures.

Fourier-transform infrared spectrometer (Bruker 80 FTIR) for different polarizations, angles, and temperatures, utilizing the setup depicted in Fig. 5. The interference condition in the interferometric part of the FTIR limits the area on the sample from which the light is effectively collected (diameter about 0.2 mm). The emission from this surface area of the heated samples is captured for different angles. The sample holder is designed to maintain the surface of the samples at the focal spot of the parabolic mirror (with focal length of 100 mm) at the input port of the FTIR spectrometer. The emitted signal is captured using an aperture, collimated by a parabolic mirror, passed through the interferometer, and collected by a nitrogen-cooled mercury cadmium telluride (MCT) detector after passing through a KRS-5 wire-grid polarizer to separate TE and TM polarizations. The FTIR spectrometer collects the emission from a surface area with the diameter of 3 mm of the sample resulting in a full acceptance angle of approximately 2°. The gold mirror on the back side of the sample serves as a reflector, preventing emission from the heater from entering the interferometer. Emission characterization for all samples is conducted at thermal equilibrium at five temperatures of 25°C, 50°C, 90°C, 130°C, 160°C achieved through the use of a resistor-ceramic heater connected to a controller, along with a resistor temperature sensor providing feedback with a precision of 0.5°C. The emissivity of the samples is then calculated using a reference sample with a known emissivity [32]. For the reference sample, we used Acktar Metal Velvet™ foil, which exhibits an absorptance exceeding 99% across the UV to far-infrared spectral range (0.3–14 μm) [33]. The calculated emissivity is relatively temperature-independent over the specified range; herefore we report in Fig. 2 the emissivity remeasured at 160°C (see Supplementary information for temperature-dependent spectra at various angles).

4 Discussion

Thermal emission from a material can be modified through the engineering of the radiation constituents. These thermally induced oscillating electrical currents obey the fluctuation–dissipation theorem and can be numerically determined for complex structures [34, 35]. The properties of the thermal radiation can then be deduced from

the Maxwell equations for both the near- and far-field regions. The properties of the primary radiative elements of the emitter are governed by the material properties and its response to the heat, microscopically defined as temperature, its wavelength, life time or bandwidth for example. The total sum of these constituent radiations define the characteristics of the final emission. From the quantum nature of thermal radiation, the spectral density of a thermal emitter is described by Planck's law, governed by mean thermal photon energy and density of states, where the mean photon number follows the Bose-Einstein distribution. The density of states quantifies the number of photonic states available per frequency interval and unit volume. Hence, in the far-field and for a gray-body emitter, the spectral density of emission, I, can be expressed as the product of the spectral density of emission from a black-body, I_{BB}, and the emissivity, ϵ of the emitter[36, 37]:

$$I(\lambda, \theta, T) = I_{BB} \cdot \epsilon(\lambda, \theta, T) \tag{3}$$

$$I_{BB}(\lambda, T) = \frac{2hc^2}{\lambda^5} \frac{1}{e^{hc/\lambda k_B T} - 1} \tag{4}$$

where λ is the wavelength of the emission, T represents the temperature of the emitter at thermal equilibrium in Kelvin, h and k_B are the Planck's and Boltzmann constant, respectively, and c is the speed of light in the vacuum. By reducing the thickness of polar dielectrics into the sub-wavelength regime, we can couple the energy into the desired states by quenching the unwanted emissions, thereby minimizing the broadening of the emission peak at the ENZ wavelength. The thermal behaviour of a crystal, whether radiative or non-radiative, hinges on the interplay of the quantum oscillators within the material as well as its boundary conditions imposed by the surrounding environment. The strength, frequency, and direction of the oscillations in response to the applied energy (heat) are primarily associated with the atomic bonds, mass distribution, and the degree of freedom in the displacement of the ionic charges in the material. When light impinges on a material, its energy can couple to the modes that accommodate the momentum and energy matching to the incident light, leaving the other modes left unexcited; whereas for thermal excitation of the optical modes from a bulk material all the possible modes have a chance to emerge unless otherwise engineered accordingly. This probabilistic behaviour is then well formulated in Planck's law. For a bulk material, at thermal equilibrium, all the allowed eigenstates can be occupied, each having a mean energy of $hc/\lambda(e^{hc/\lambda k_B T} - 1)$. The given heat energy is therefore distributed over all the states (modes) and, consequently, the thermal emission from a heated object tends to be broad-spectrum, un-polarized, and temporally and spatially incoherent. This behavior arises not only from the proximity of energy eigenstates in solids but also from phonon-photon or phonon-phonon scattering mechanisms. In other words, for an incandescent source of light the emissions from different points of the emitter are incoherent. It is also worth mentioning that thin films, relative to the bulk material, are reported to mitigate self-absorption (reabsorption of emitted radiation) and as a result can produce narrower emission features due to uniform temperature gradient over the thin film [38].

To achieve a desired thermal emission from silicon dioxide, among the mentioned contributing factors, the parameter we have at our disposal is the direction of charge oscillation, which we can engineer in our favor. In consideration of the nature of optical transverse and longitudinal phonon resonances in a crystal, the strategic reduction of polar dielectric thickness into the extremely sub-wavelength regime promotes effective coupling into the desired modes. In other words, by structuring a material we engineer the polaritonic electromagnetic density of states and, consequently, the thermal radiation [39]. It increases the strength of total emission from the desired oscillatory dipole moments relative to those oscillating in undesired directions, and as a result make that mode dominant. Our numerical and experimental results show that thermal emission from sub-wavelength silicon dioxide films can deviate strongly from blackbody behavior. Within the Reststrahlen band, a sub-wavelength silicon dioxide film supports surface phonon-polaritons at its two interfaces; when the layer is sufficiently thin, these surface modes hybridize, producing a leaky Berreman (and ENZ) mode whose dispersion is nearly flat near the LO phonon frequency [20, 27]. The associated normal field inside the ultra-thin film is approximately uniform and strongly enhanced due to the ENZ response. As the thickness decreases, hybridization strengthens and the modal overlap with the lossy film volume falls which reduces non-radiative damping. These effects can narrow the absorption/emission line and yield spectrally sharper far-field thermal emission for thinner films. For an ENZ material the wavelength inside the material is much longer than the free-space wavelength, so fields across an ultra-thin film are nearly in-phase. Within this region, the in-phase electromagnetic fields constructively interfere in the far-field and can enhance directionality in the vicinity of the ENZ region [28]. In fact, FTIR measurements indirectly demonstrate temporal coherence. An FTIR spectrometer (a Michelson interferometer) measures the autocorrelation function of the thermal emission field, and then applies the Fourier transform to obtain the emission spectrum. According to the Wiener–Khinchin theorem, the sharper the spectral peak, the longer the temporal coherence time/length. Therefore, the spectral sharpening of the emission is indicative of increased temporal coherence in our structures [40]. Note, that the FTIR used here, effectively samples a region of only about 0.2 mm across. If the ENZ wavelength were to exceed this number, any corresponding spatially coherent emission will only be partially captured by the current set-up. Hence, an ultra-thin slab composed of a material with negative permittivity can under certain conditions lead to the excitation of the ENZ mode inside the material. This mode features an enhanced and uniform electric field inside the thin film, providing extreme confinement of phonon polaritons. In addition, the ultra-thin structure effectively suppresses the otherwise incoherent emissions close to the ENZ wavelength.

5 Conclusions

In this study, we investigated the thermal emission characteristics of ultra-thin structures of silicon dioxide thin films with respect to temperature, polarization, and optical orientation. Our observations reveal spectrally narrow emissivity, suggesting temporally coherent behavior occurring at phononic-induced ENZ. We investigated how the

ultra-thin layer of silicon dioxide provides coherent emission thanks to the in-phase quantum oscillations associated with the uniform field distribution in the structure in the vicinity of ENZ domain. Moreover, emission with an enhanced Q-factor is achieved due to the suppression of undesired emissions and consequently less broadening of the resonance features of the material in those wavelengths. To support our conclusions, we measured the thermal emission of ultra-thin structures of silicon dioxide films deposited on Si with respect to temperature, polarization, and optical orientation. We verified our measurements with the numerical calculation of the absorption spectra of the samples. The work presented here offers a potential route towards the development of narrow-band, angle-dependent mid-IR thermal emitters, in addition to intriguing possibilities for coupling longitudinal lattice excitation to free-space radiation. The implications of this study extend to a heightened comprehension of the thermal emission from polar crystals. This enhanced understanding holds the potential to catalyze the development of novel optical devices, spanning applications ranging from thermal emitters to systems reliant on polarization effects.

Declarations

All authors have approved this submission, and we declare no conflicts of interest. The data supporting the findings of this study are available from the corresponding authors upon reasonable request.

References

[1] Shayegan, K.J., Biswas, S., Zhao, B., Fan, S., Atwater, H.A.: Direct observation of the violation of kirchhoff's law of thermal radiation. Nature Photonics **17**(10), 891–896 (2023) https://doi.org/10.1038/s41566-023-01261-6

[2] Sabbaghi, P., Long, L., Ying, X., Lambert, L., Taylor, S., Messner, C., Wang, L.: Super-Planckian radiative heat transfer between macroscale metallic surfaces due to near-field and thin-film effects. Journal of Applied Physics **128**(2), 025305 (2020) https://doi.org/10.1063/5.0008259

[3] Guo, Y., Cortes, C.L., Molesky, S., Jacob, Z.: Broadband super-Planckian thermal emission from hyperbolic metamaterials. Applied Physics Letters **101**(13), 131106 (2012) https://doi.org/10.1063/1.4754616

[4] Pascale, M., Giteau, M., Papadakis, G.T.: Perspective on near-field radiative heat transfer. Applied Physics Letters **122**(10), 100501 (2023) https://doi.org/10.1063/5.0142651

[5] Baranov, D.G., Xiao, Y., Nechepurenko, I.A., Krasnok, A., Alù, A., Kats, M.A.: Nanophotonic engineering of far-field thermal emitters. Nature Materials **18**(9), 920–930 (2019) https://doi.org/10.1038/s41563-019-0363-y

[6] Papadakis, G.T., Ciccarino, C.J., Fan, L., Orenstein, M., Narang, P., Fan, S.:

Deep-subwavelength thermal switch via resonant coupling in monolayer hexagonal boron nitride. Physical Review Applied **15**, 054002 (2021) https://doi.org/10.1103/PhysRevApplied.15.054002

[7] Lyu, B., Li, H., Jiang, L., Shan, W., Hu, C., Deng, A., Ying, Z., Wang, L., *et al.*: Phonon polariton-assisted infrared nanoimaging of local strain in hexagonal boron nitride. Nano Letters **19**(3), 1982–1989 (2019) https://doi.org/10.1021/acs.nanolett.8b05166

[8] Shahsafi, A., Xiao, Y., Salman, J., Gundlach, B.S., Wan, C., Roney, P.J., Kats, M.A.: Mid-infrared optics using dielectrics with refractive indices below unity. Phys. Rev. Applied **10**, 034019 (2018) https://doi.org/10.1103/PhysRevApplied.10.034019

[9] Shaik, A.B.D., Palla, P.: Optical quantum technologies with hexagonal boron nitride single photon sources. Scientific Reports **11**(1), 12285 (2021) https://doi.org/10.1038/s41598-021-91364-x

[10] White, S.J.U., Yang, T., Dontschuk, N., *et al.*: Electrical control of quantum emitters in a van der waals heterostructure. Light: Science and Applications **11**(1), 186 (2022) https://doi.org/10.1038/s41377-022-00776-1

[11] Laroche, M., Carminati, R., Greffet, J.-J., Joulain, J.-P.D.: Coherent thermal antenna using a photonic crystal slab. Physical Review Letters **96**(12), 123903 (2006) https://doi.org/10.1103/PhysRevLett.96.123903

[12] Ying, Y., Ma, B., Yu, J., Huang, Y., Ghosh, P., Shen, W., Qiu, M., Li, Q.: Whole lwir directional thermal emission based on enz thin films. Laser & Photonics Reviews **16**(8), 2200018 (2022) https://doi.org/10.1002/lpor.202200018

[13] Liu, R., Zhou, C., Zhang, Y., Cui, Z., Wu, X., Yi, H.: Near-field radiative heat transfer in hyperbolic materials. International Journal of Extreme Manufacturing **4**(3), 032002 (2022) https://doi.org/10.1088/2631-7990/ac4d6d

[14] Li, P., Lewin, M., Kretinin, A., *et al.*: Hyperbolic phonon-polaritons in boron nitride for near-field optical imaging and focusing. Nature Communications **6**(1), 7507 (2015) https://doi.org/10.1038/ncomms8507

[15] Zhao, B., Shi, Y., Wang, J., Zhao, Z., Zhao, N., Fan, S.: Near-complete violation of Kirchhoff's law of thermal radiation with a 0.3 t magnetic field. Optics Letters **44**(16), 4203–4206 (2019) https://doi.org/10.1364/OL.44.004203

[16] Inoue, T., Koyama, T., Kang, D.D., Ikeda, K., Asano, T., Noda, S.: One-chip near-field thermophotovoltaic device integrating a thin-film thermal emitter and photovoltaic cell. Nano Letters **19**(6), 3948–3952 (2019)

[17] Greffet, J.-J., Carminati, R., Joulain, J.-P.D.: Coherent thermal emission of light

by thermal sources. Nature **416**(6876), 61–64 (2002) https://doi.org/10.1038/416061a

[18] Khan, I., Palei, M., Dominguez, O., Simmons, E., Podolskiy, V.A., Hoffman, A.J.: Vertical thermal emission from optical antennas on an epsilon-near–zero substrate. Advanced Optical Materials **12**(25), 2400715 (2024) https://doi.org/10.1002/adom.202400715

[19] Shin, S., Elzouka, M., Prasher, R., *et al.*: Far-field coherent thermal emission from polaritonic resonance in individual anisotropic nanoribbons. Nature Communications **10**, 1377 (2019) https://doi.org/10.1038/s41467-019-09378-5

[20] Nordin, L., Dominguez, O., Roberts, C.M., Streyer, W., Feng, K., Fang, Z., Podolskiy, V.A., Hoffman, A.J., Wasserman, D.: Mid-infrared epsilon-near-zero modes in ultra-thin phononic films. Applied Physics Letters **111**(9), 091105 (2017) https://doi.org/10.1063/1.4996213

[21] Ogawa, S., Fukushima, S., Shimatani, M.: Extraordinary optical transmission by hybrid phonon–plasmon polaritons using hbn embedded in plasmonic. Journal of the Optical Society of America A **14**(4), 741–755 (1997) https://doi.org/10.1364/JOSAA.14.000741

[22] Rivera, N., Christensen, T.K., Narang, P.: Phonon polaritonics in two-dimensional materials. Nano Letters **19**(4), 2653–2660 (2019) https://doi.org/10.1021/acs.nanolett.9b00767

[23] Li, N., Guo, X., Yang, X., *et al.*: Direct observation of highly confined phonon polaritons in suspended monolayer hexagonal boron nitride. Nature Materials **20**(1), 43–48 (2021) https://doi.org/10.1038/s41563-020-00800-x

[24] Caldwell, J.D., Lindsay, L., Giannini, V., Vurgaftman, I., Reinecke, T.L., Maier, S.A., Glembocki, O.J.: Low-loss, infrared and terahertz nanophotonics using surface phonon polaritons. Nanophotonics **4**(1), 44–68 (2015) https://doi.org/10.1515/nanoph-2014-0007

[25] Ziman, J.M.: Principles of the Theory of Solids. Cambridge University Press, Cambridge (1972). https://doi.org/10.1017/CBO9781139644075

[26] Caldwell, J.D., Kretinin, A., Chen, Y., *et al.*: Sub-diffractional volume-confined polaritons in the natural hyperbolic material hexagonal boron nitride. Nature Communications **5**(1), 1–7 (2014) https://doi.org/10.1038/ncomms4314

[27] Vassant, S., Hugonin, J.-P., Marquier, F., Greffet, J.-J.: Berreman mode and epsilon near zero mode. Optics Express **20**(21), 23971–23977 (2012) https://doi.org/10.1364/OE.20.023971

[28] Alù, A., Silveirinha, M.G., Salandrino, A., Engheta, N.: Epsilon-near-zero metamaterials and electromagnetic sources: Tailoring the radiation phase pattern. Phys. Rev. B **75**, 155410 (2007) https://doi.org/10.1103/PhysRevB.75.155410

[29] Alam, M.Z., De Leon, I., Boyd, R.W.: Large optical nonlinearity of indium tin oxide in its epsilon-near-zero region. Science **352**(6287), 795–797 (2016) https://doi.org/10.1126/science.aad3105

[30] Ma, E.Y., Hu, J., Waldecker, L., Watanabe, K., Taniguchi, T., Liu, F., Heinz, T.F.: The reststrahlen effect in the optically thin limit: A framework for resonant response in thin media. Nano Letters **22**(20), 8389–8393 (2022) https://doi.org/10.1021/acs.nanolett.2c02819 . PMID: 36112673

[31] Kischkat, J., Peters, S., Gruska, B., Semtsiv, M., Chashnikova, M., Klinkmüller, M., *et al.*: Mid-infrared optical properties of thin films of aluminum oxide, titanium dioxide, silicon dioxide, aluminum nitride, and silicon nitride. Applied Optics **51**, 6789–6798 (2012) https://doi.org/10.1364/AO.51.006789

[32] Folland, T.G., Nordin, L., Wasserman, D.: Probing polaritons in the mid- to far-infrared. Journal of Applied Physics **125**(19), 191102 (2019) https://doi.org/10.1063/1.5085824

[33] Zhang, Z., Kalantari Dehaghi, A., Ghosh, P., Zhu, L.: Observation of strong nonreciprocal thermal emission. Phys. Rev. Lett. **135**, 016901 (2025) https://doi.org/10.1103/PhysRevLett.135.016901

[34] Kubo, R.: The fluctuation-dissipation theorem. Reports on Progress in Physics **29**(1), 255 (1966) https://doi.org/10.1088/0034-4885/29/1/306

[35] Rytov, S.M., Erkku, H.: Theory of Electric Fluctuations and Thermal Radiation. Air Force Cambridge Research Center, Bedford, MA (1959)

[36] Planck, M.: The Theory of Heat Radiation. Blakiston, Philadelphia (1914)

[37] Picardi, M.F., Nimje, K.N., Papadakis, G.T.: Dynamic modulation of thermal emission—a tutorial. Journal of Applied Physics **133**(11), 111101 (2023) https://doi.org/10.1063/5.0089223

[38] Griffiths, P.R., Haseth, J.A.: Fourier Transform Infrared Spectrometry, 2nd edn. John Wiley & Sons, Hoboken, NJ (2007)

[39] Coldren, L.A., Corzine, S.W., Mašanović, M.L.: Diode Lasers and Photonic Integrated Circuits, 2nd edn. Wiley, Hoboken, NJ (2012)

[40] Goodman, J.W.: Statistical Optics, 2nd edn. John Wiley & Sons, Hoboken, NJ (2015)

Supplementary information

1. Comparison of the Q-factor of the emissivity of the thin-film samples reported in Fig. 3 of the paper in unscaled format.

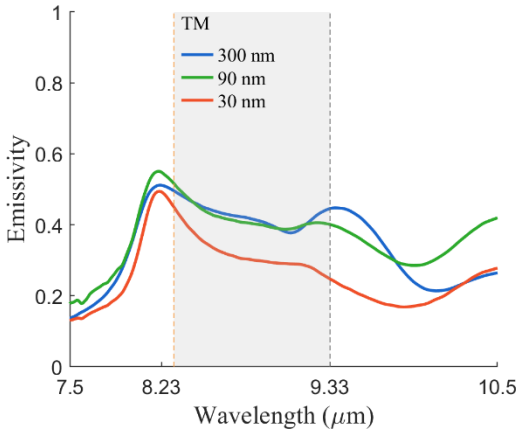

Fig. S1. Emissivity for 300~nm, 90~nm, and 30~nm thin films of silicon dioxide on a 2-mm-thick Si substrate for TM polarizations at angles of 60°, 80° and 80°, respectively using a FTIR spectrometer. For each curve, the chosen angle is the one for which the emissivity shows the largest quality factor.

2. Comparison of the measurements and simulations.

Below, we present a comprehensive comparison between the simulated and experimentally measured emissivity spectra for all three film thicknesses and the bulk material, under both TE and TM polarizations, at incident angles ranging from 0° to 80° in 10° increments. The overall agreement between simulation and measurement is clear, particularly in capturing the angular and polarization dependence of the emission. For TM polarization, a pronounced emissivity peak is observed at larger angles as the film thickness decreases. However, a slight offset in the measured emissivity values is observed which we attribute to a weak plateau emission from the underlying Si substrate. Whereas, in the simulation, the permittivity model used for Si doesn't have an imaginary part and therefore no absorption is observed in the simulations. Furthermore, for the bulk case, emissivity measurements were carried out using a 1-mm-thick BK7 glass sample, while simulations utilized permittivity data for bulk silicon dioxide reported by Popova *et al* [1]. The differences in material response can be attributed to the fact that silicon dioxide is an amorphous material, whose phonon dispersion and optical response can vary slightly across samples, especially near the Reststrahlen band. Moreover, for TE polarization, the observed peaks around the LO phonon resonances are due to polarization coupling and as expected does not appear in the simulations. Each panel (a-i)

belongs to each angle has eight subplots (2×4) presenting the simulation and measurement results for each sample (columns 1-4) for TE (top) and TM (bottom) polarizations.

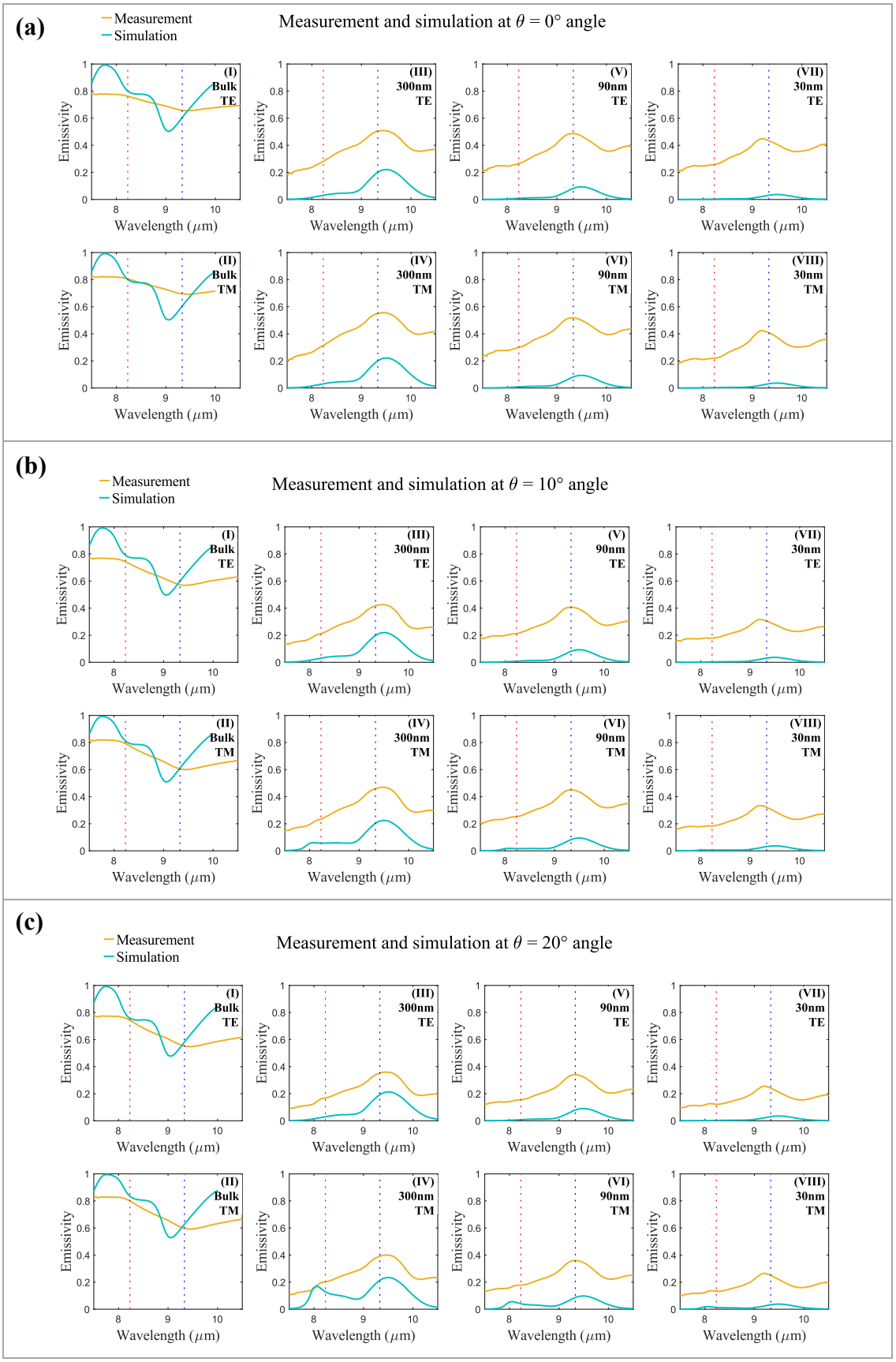

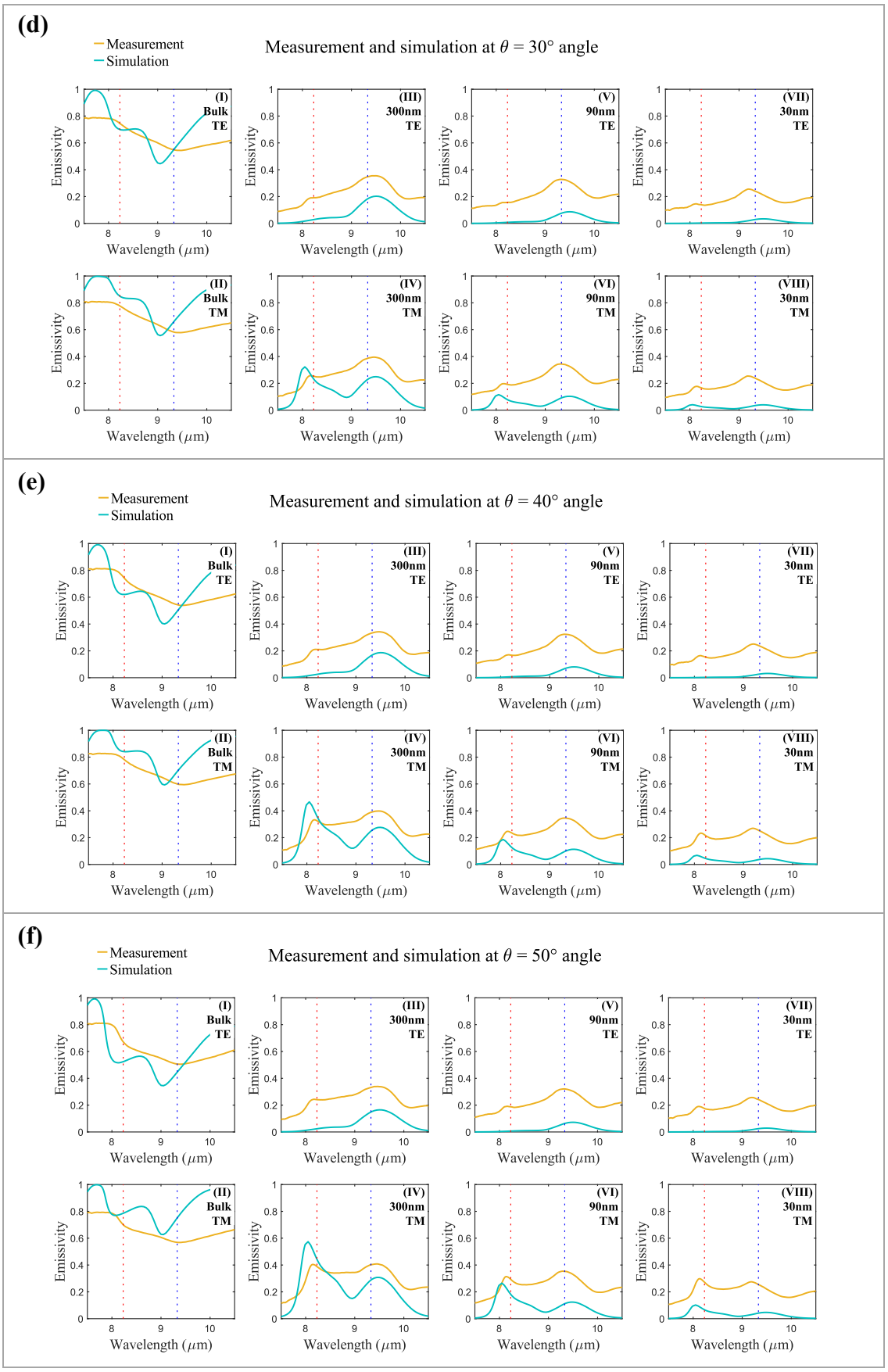
(d)
Measurement
Simulation
Measurement and simulation at θ = 30° angle
(I) Bulk TE
(III) 300nm TE
(V) 90nm TE
(VII) 30nm TE
(II) Bulk TM
(IV) 300nm TM
(VI) 90nm TM
(VIII) 30nm TM
Emissivity
Wavelength (μm)
(e)
Measurement
Simulation
Measurement and simulation at θ = 40° angle
(I) Bulk TE
(III) 300nm TE
(V) 90nm TE
(VII) 30nm TE
(II) Bulk TM
(IV) 300nm TM
(VI) 90nm TM
(VIII) 30nm TM
Emissivity
Wavelength (μm)
(f)
Measurement
Simulation
Measurement and simulation at θ = 50° angle
(I) Bulk TE
(III) 300nm TE
(V) 90nm TE
(VII) 30nm TE
(II) Bulk TM
(IV) 300nm TM
(VI) 90nm TM
(VIII) 30nm TM
Emissivity
Wavelength (μm)

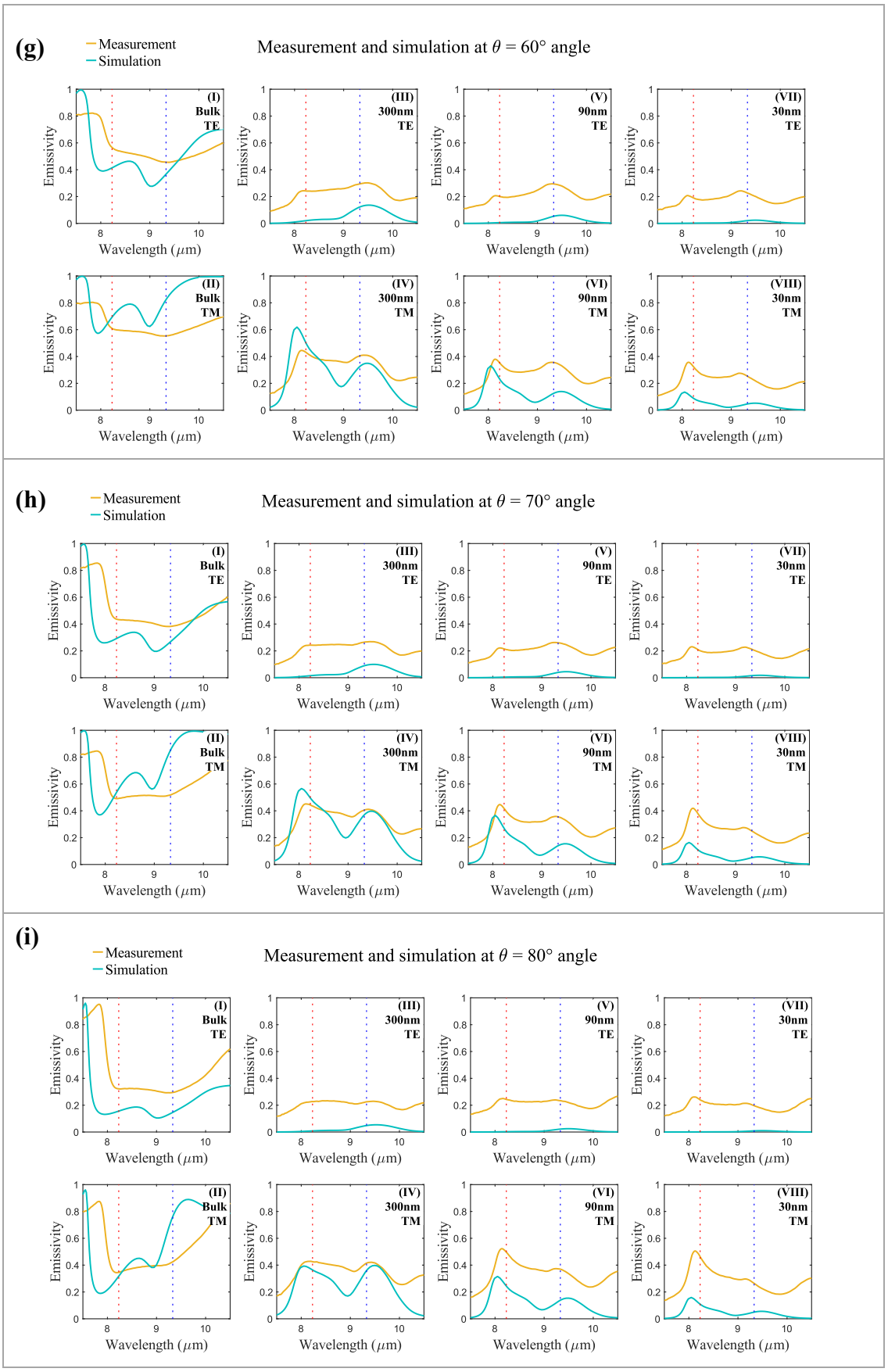
(g)
Measurement
Simulation
Measurement and simulation at θ = 60° angle
(I) Bulk TE
(III) 300nm TE
(V) 90nm TE
(VII) 30nm TE
(II) Bulk TM
(IV) 300nm TM
(VI) 90nm TM
(VIII) 30nm TM
Emissivity
Wavelength (μm)
(h)
Measurement
Simulation
Measurement and simulation at θ = 70° angle
(I) Bulk TE
(III) 300nm TE
(V) 90nm TE
(VII) 30nm TE
(II) Bulk TM
(IV) 300nm TM
(VI) 90nm TM
(VIII) 30nm TM
Emissivity
Wavelength (μm)
(i)
Measurement
Simulation
Measurement and simulation at θ = 80° angle
(I) Bulk TE
(III) 300nm TE
(V) 90nm TE
(VII) 30nm TE
(II) Bulk TM
(IV) 300nm TM
(VI) 90nm TM
(VIII) 30nm TM
Emissivity
Wavelength (μm)

3. Measured emissivity at different temperatures

We performed emission measurements at five temperatures being 25°C, 50°C, 90°C, 130°C, and 160°C. The 130°C temprature was used as a reference to calculate emissivity for other temperatures. Each figure panel (a-d) belongs to each sample for TE (left) and TM (right) polarization. And, for each polarization there are nine subplots (3×3) showing temperature dependence for different angels from 0° to 80°.

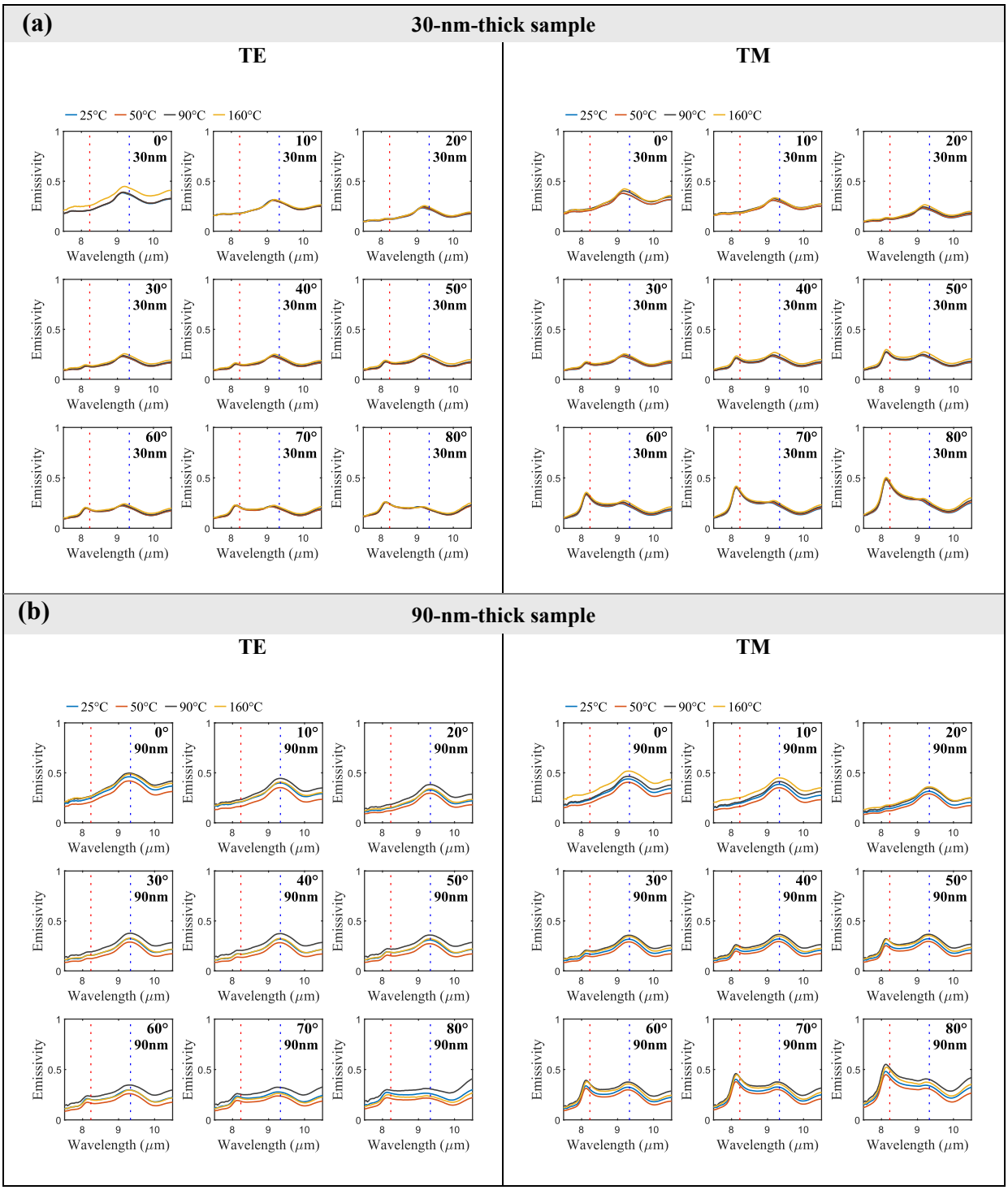

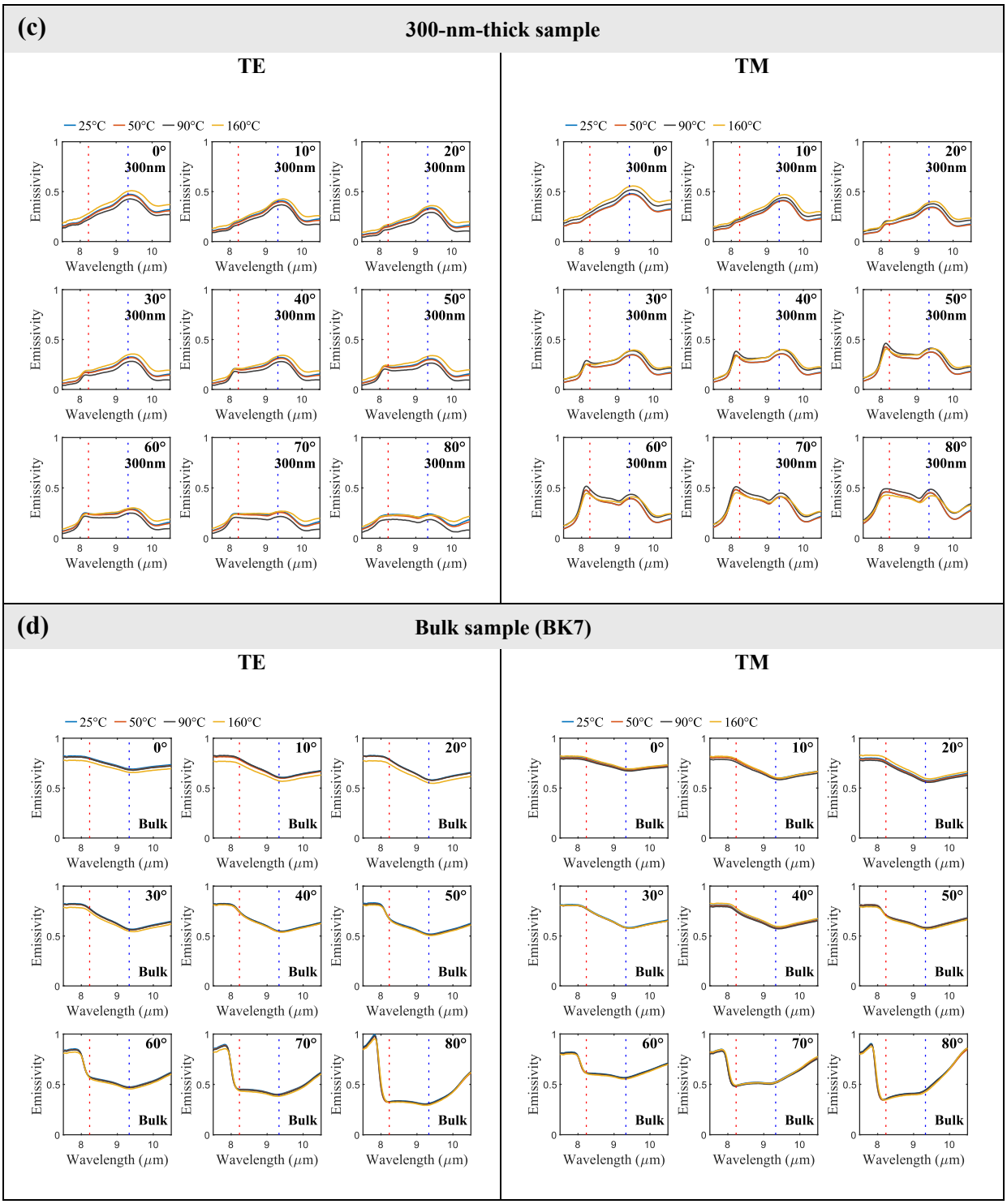
(c)
300-nm-thick sample
TE
TM
25°C 50°C 90°C 160°C
0° 300nm
10° 300nm
20° 300nm
30° 300nm
40° 300nm
50° 300nm
60° 300nm
70° 300nm
80° 300nm
Emissivity
Wavelength (μm)
(d)
Bulk sample (BK7)
TE
TM
25°C 50°C 90°C 160°C
0° Bulk
10° Bulk
20° Bulk
30° Bulk
40° Bulk
50° Bulk
60° Bulk
70° Bulk
80° Bulk
Emissivity
Wavelength (μm)

4. The measured emissions at different temperatures

Emission measurements at 25°C, 50°C, 90°C, 160°C, for all samples, under both TE and TM polarizations, at incident angles ranging from 0° to 80° in 10° increments. Each panel (a-i) belongs to each angle has eight subplots (2×4) presenting the measurement results for each sample (columns 1-4) for TE (top) and TM (bottom) polarizations.

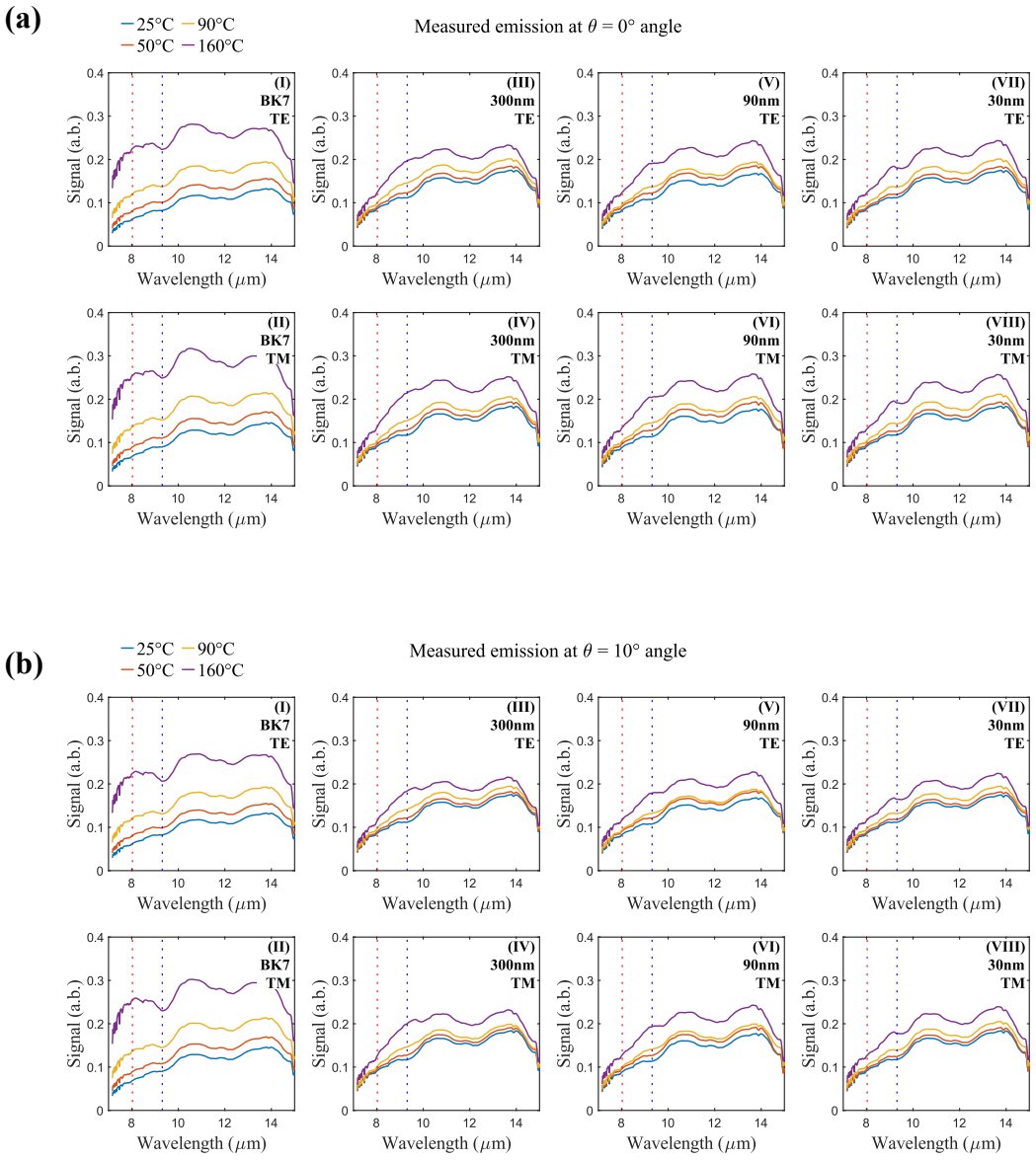

(c)

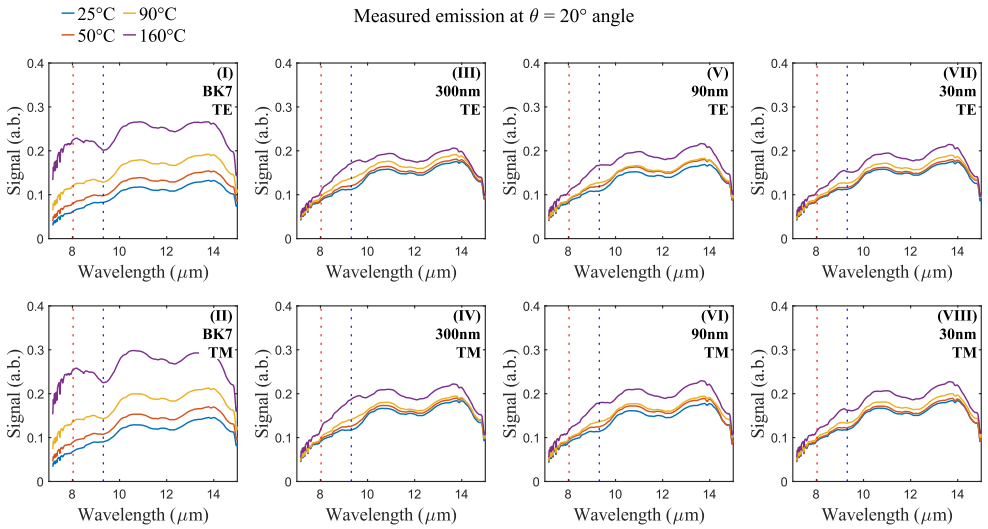
25°C 90°C
50°C 160°C
Measured emission at θ = 20° angle
(I) BK7 TE
(III) 300nm TE
(V) 90nm TE
(VII) 30nm TE
(II) BK7 TM
(IV) 300nm TM
(VI) 90nm TM
(VIII) 30nm TM
Signal (a.b.)
Wavelength (μm)

(d)

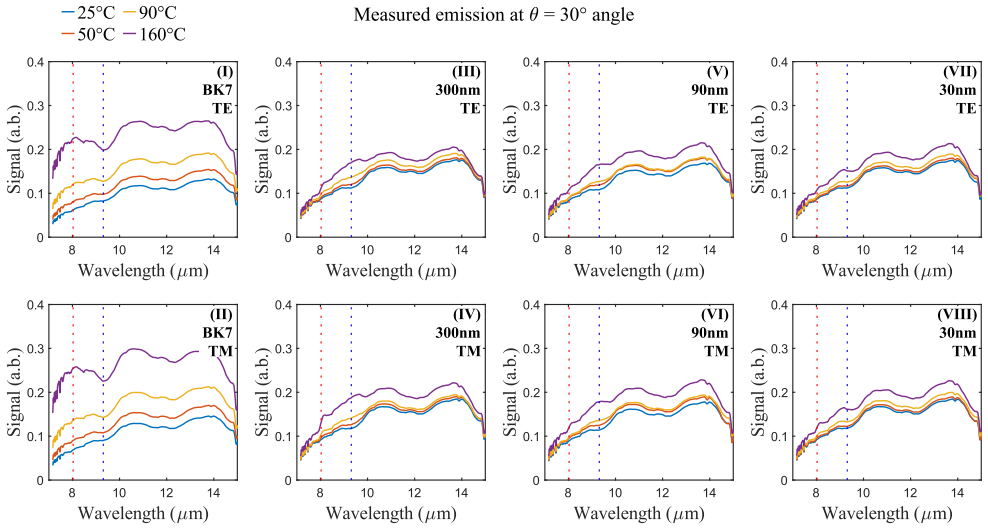
25°C 90°C
50°C 160°C
Measured emission at θ = 30° angle
(I) BK7 TE
(III) 300nm TE
(V) 90nm TE
(VII) 30nm TE
(II) BK7 TM
(IV) 300nm TM
(VI) 90nm TM
(VIII) 30nm TM
Signal (a.b.)
Wavelength (μm)

(e)

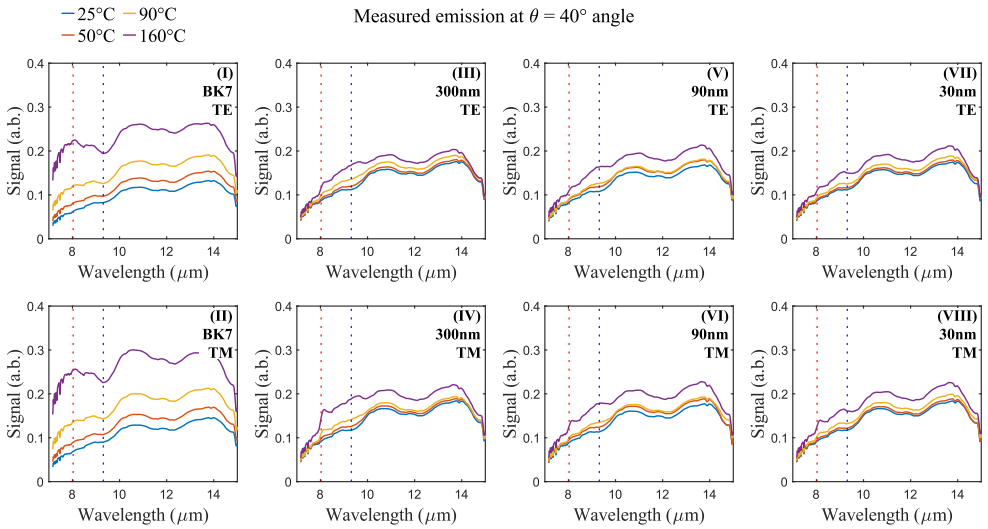
25°C 90°C
50°C 160°C
Measured emission at θ = 40° angle
(I) BK7 TE
(III) 300nm TE
(V) 90nm TE
(VII) 30nm TE
(II) BK7 TM
(IV) 300nm TM
(VI) 90nm TM
(VIII) 30nm TM
Signal (a.b.)
Wavelength (μm)

(f)

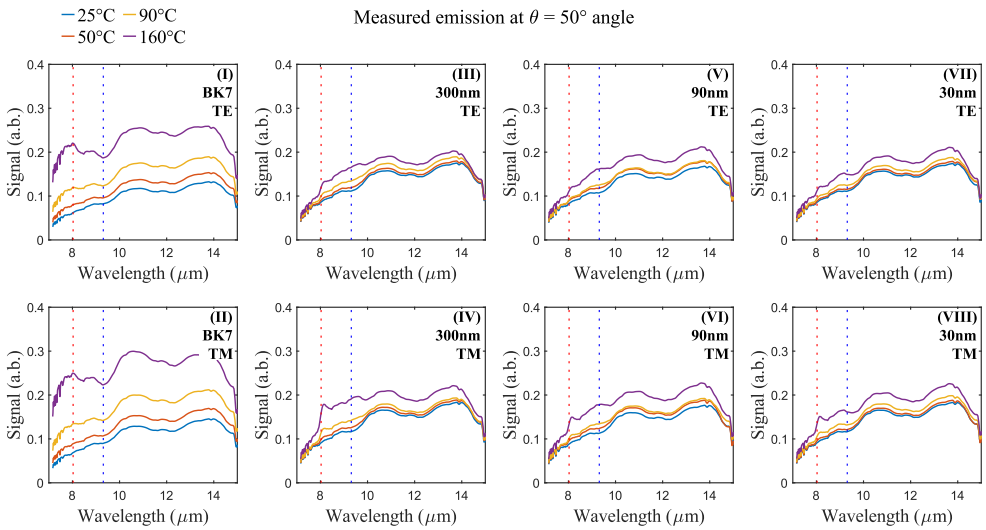
25°C 90°C
50°C 160°C
Measured emission at θ = 50° angle
(I) BK7 TE
(III) 300nm TE
(V) 90nm TE
(VII) 30nm TE
(II) BK7 TM
(IV) 300nm TM
(VI) 90nm TM
(VIII) 30nm TM
Signal (a.b.)
Wavelength (μm)

(g)

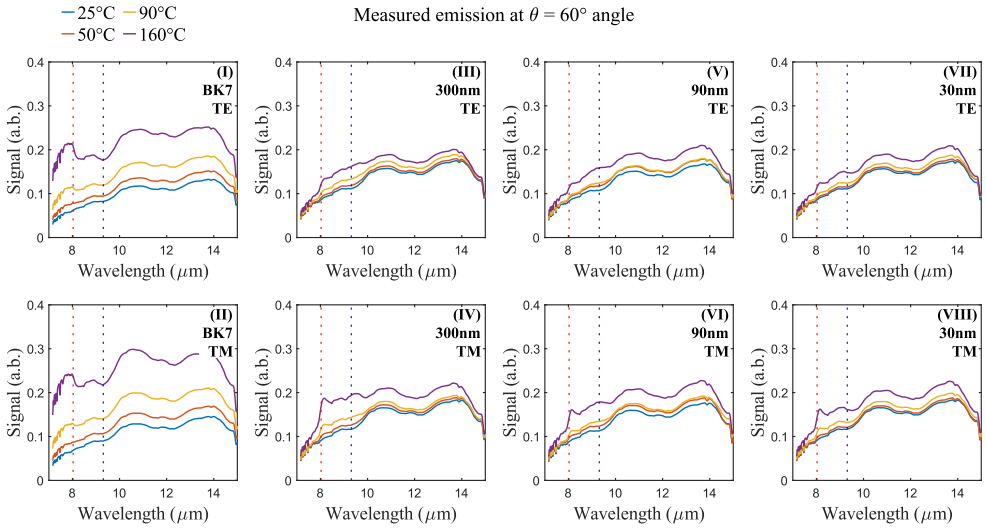
25°C 90°C
50°C 160°C
Measured emission at θ = 60° angle
(I) BK7 TE
(III) 300nm TE
(V) 90nm TE
(VII) 30nm TE
(II) BK7 TM
(IV) 300nm TM
(VI) 90nm TM
(VIII) 30nm TM
Signal (a.b.)
Wavelength (μm)

(h)

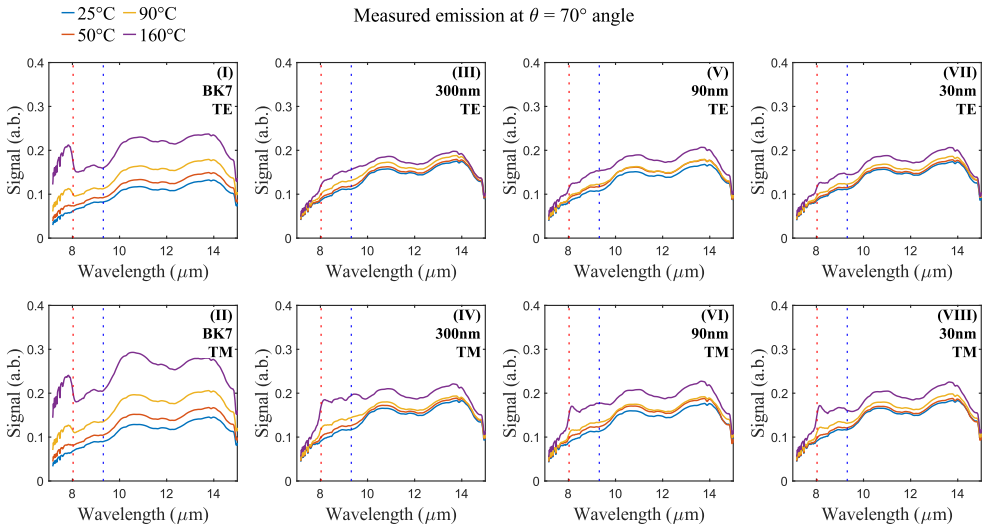
25°C 90°C
50°C 160°C
Measured emission at θ = 70° angle
(I) BK7 TE
(III) 300nm TE
(V) 90nm TE
(VII) 30nm TE
(II) BK7 TM
(IV) 300nm TM
(VI) 90nm TM
(VIII) 30nm TM
Signal (a.b.)
Wavelength (μm)

(i)

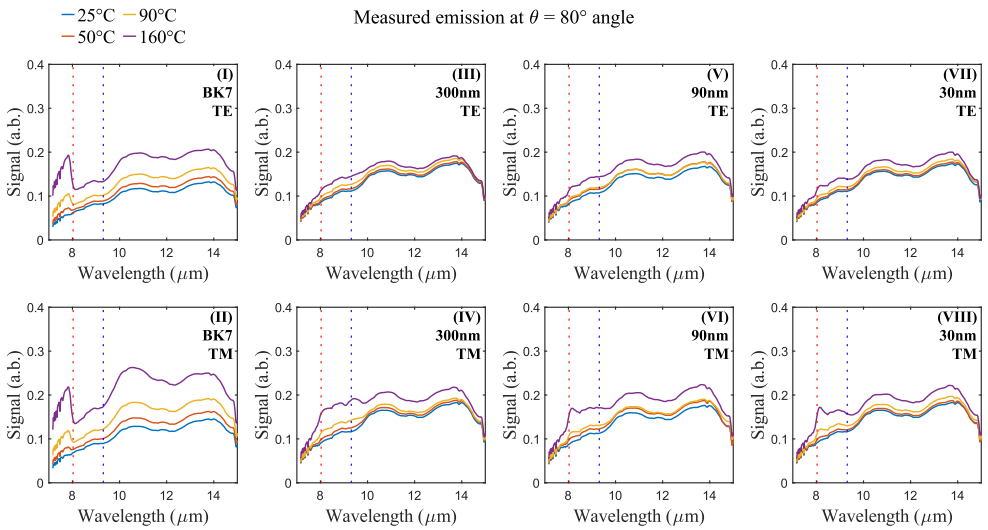

References:

1. S. Popova, T. Tolstykh, V. Vorobev. Optical characteristics of amorphous quartz in the 1400–200 cm^{-1} region, *Opt. Spectrosc.* **33**, 444–445 (1972)

Chapter 3

Strong coupling of gap plasmons with epsilon-near-zero phonon polaritons

3.1 Contribution Statement

The promising optical properties of epsilon-near-zero (ENZ) materials—such as enhanced nonlinearities, phase uniformity, and spatially extended field distributions—offer significant promise for tailoring light–matter interactions. However, a key challenge in accessing these ENZ modes lies in the stringent momentum-matching requirements for free-space excitation. In planar films, this often demands large-angle incidence or sophisticated prism coupling techniques, which are incompatible with compact or integrated device designs. When two resonant systems interact coherently, they no longer behave as independent oscillators. Instead, they form hybridized eigenmodes (upper and lower polaritons) whose frequencies, field profiles, and dispersions are admixtures of the parent resonances and exhibit a clear avoided crossing near zero detuning.

Here, we proposed a metasurface strategy that provides normal-incidence access to ENZ phonon–polaritons and enables designer control of the hybrid dispersion. The platform consists of a periodic array of gold patch (gap-plasmon) antennas integrated on a Al_2O_3 ENZ film. By bringing the gap-plasmon resonance into spectral overlap with the ENZ mode, the system enters the strong-coupling regime, producing a resolvable mode splitting and intense, localized fields. These hybrid modes are valuable because they inherit the extreme field confinement of the ENZ mode of the thin-film, while having the potential to operate over preferential frequencies in the mid-IR spectrum. Although the ENZ wavelength is fixed by the material's phonon frequency, the

hybrid system can be spectrally designed across the mid-IR by tuning the plasmonic resonance geometrically (e.g., patch width), thereby positioning the hybrid polaritons at target wavelengths. In this work we designed and numerically modeled a metasurface structure in which the localized gap plasmon resonances of a gold patch antenna array strongly couple with the ENZ phonon-polariton mode of a nanometer-thin Al_2O_3 film. The structural parameters—such as patch width and ENZ layer thickness—were studied to bring the two resonances into spectral overlap and achieve strong coupling.

This project was completed under expert guidance and technical discussions provided by Dr. Jeremy Upham, Dr. M. Zahirul Alam, and Prof. Robert W. Boyd. My contribution in this project is as follows. I conducted full-wave electromagnetic simulations using the Lumerical FDTD solver to map the reflectance spectra and field distributions for various gold patch width and ENZ film thicknesses. These simulations revealed the evolution of hybrid polariton branches and distinct anti-crossing behavior and mode splitting, indicative of strong coupling between the two primary systems. I measured more than 50 samples using Fourier transform infrared (FTIR) spectrometer. I performed analysis of the numerical and measurement data. The measured reflectance spectra confirmed the predicted mode splitting and matched the simulated results with excellent agreement. I wrote the first draft of the manuscript. The fabrication of the samples was carried out by Dr. Matthew Klein, Dr. Dennis E. Walker Jr., Dr. Shivashankar Vangala, Dr. Joshua R. Hendrickson, from Air Force Research Laboratory, USA.

In summary, beyond demonstrating normal-incidence coupling to a phononic ENZ mode, this chapter establishes a tunable, strongly coupled ENZ–plasmon platform whose hybridized modes can be positioned across the mid-IR via geometry, while preserving ENZ-mediated field concentration, an attractive combination for sensing, nonlinear optics, and thermal-photonics applications.

Observation of strong coupling of gap plasmons with epsilon-near-zero phonon polaritons

Maryam Abbasi,[†] Matthew Klein,[‡,¶] Dennis E. Walker Jr.,[¶] Jeremy Upham,[§] Shivashankar Vangala,[¶] Joshua R. Hendrickson,[¶] M. Zahirul Alam,[§] and Robert W. Boyd[§,†,‖]

[†]*Department of Electrical Engineering, University of Ottawa, ON K1N1A2, Canada.*

[‡]*KBR, Beavercreek, Ohio 45431, USA.*

[¶]*Sensors Directorate, Air Force Research Laboratory, Wright-Patterson AFB, OH 45433, USA.*

[§]*Department of Physics, University of Ottawa, Canada.*

[‖]*Institute of Optics, University of Rochester, Rochester, NY 14627, USA.*

E-mail:

Abstract

Strong coupling between a pair of polaritons in the mid-infrared frequencies, as a consequence of near-field electromagnetic interactions between them, is a versatile platform for engineering light–matter interactions for applications in nonlinear optics, thermal physics, quantum chemistry, and quantum optics. Here, we experimentally demonstrate strong coupling between the epsilon-near-zero (ENZ) phonon polariton mode of a 10-nm-thick aluminum oxide layer and the gap plasmon polariton metasurface supported by an antenna-insulator-metal metasurface. We observe hybridization between the plasmonic and ENZ modes, resulting in mode splitting as large as 2.8 μm. This corresponds to a normalized mode splitting greater than 1, confirming strong

coupling between the two polaritonic modes. Numerical simulations performed using finite-difference time-domain (FDTD) methods show good agreement with experimental reflection spectra. We also numerically demonstrate that ultra-strong coupling between the polariton modes can be accessed by choosing an appropriate thickness of the ENZ layer. The unusual linear and nonlinear optical properties of ENZ materials make such metasurfaces useful platforms for active mid-infrared photonics, thermal emission control, chemical sensing, and enhanced nonlinear optics at mid-infrared frequencies.

Introduction

Two harmonic oscillators are said to be strongly coupled when they exchange energy faster than either of their decay rates. In this regime, the eigenstates of the coupled system become hybridized combinations of the uncoupled modes, exhibiting a characteristic avoided crossing in their dispersion curves near their uncoupled resonance frequencies. This mode splitting, sometimes referred to as a Rabi splitting, is the energy separation between the hybrid modes at the point of zero detuning .[1] Strong coupling and the resulting hybridization have emerged as a powerful tool for controlling light–matter interactions at the nanoscale, with applications ranging from quantum optics and nonlinear photonics to thermal emission engineering.[2–6]

Epsilon-near-zero (ENZ) materials – a material whose real permittivity vanishes at a certain frequency – offer a compelling platform for enhancing light–matter interactions due to their exotic linear electromagnetic properties.[7–10] The optical properties of ENZ materials at near-infrared frequencies, specifically degenerately doped semiconductors, have been well reported.[11–13] In contrast, polar dielectrics such as Al_2O_3, SiO_2, and AlN exhibit ENZ behavior due to strong phonon resonances in the mid-infrared (mid-IR) spectral region and can support low-loss modes, making them an interesting choice for mid-IR optics applications.[14–20]

A thin film of a polar dielectric material supports two types of optical modes with nearly flat dispersion near its LO phonon resonance: a radiative (leaky) Berreman mode and a

non-radiative ENZ mode.[15?] These modes exhibit strong field confinement, near-zero group velocity, and enhanced local density of optical states, making them attractive for controlling emission, absorption, and facilitating nonlinear optical processes.[3,4,21] Metamaterial resonators, quantum wells, and dipole antennas have been used to enable momentum matching and excite the otherwise dark ENZ mode through near-field interactions.[2,5,22,23] In particular, gap-plasmon metal-insulator-metal (MIM) structures that support strongly confined optical resonances have been shown to be effective in enhancing the nonlinear optical response.[21,24] In such a system, angular and spectral tunability can be achieved by adjusting the geometry of the top layer of the metasurface and the gap spacing between the two metallic layers. For example, an array of MIM antennas was used to achieve broadband infrared absorption through coupling between engineered gap modes and ENZ modes of indium tin oxide (ITO).[24]

Scientists have reported strong plasmon-phonon coupling in multiple other systems. For example, ultra-strong coupling between an effective ENZ cavity and phonon-driven ENZ materials was recently reported.[25] Other notable demonstrations of similar physics include the demonstration of a strong coupling between the ENZ mode of a polar dielectric thin film and a graphene sheet,[26] and low-energy localized surface plasmon (LSP) modes of gold dipoles on TEM thin films SiO_2.[27] However, to the best of our knowledge, this is the first investigation of strong plasmon-phonon polariton coupling using a metasurface-mediated gap plasmon and thus providing multiple convenient fabrication parameters by which to tune both the coupling wavelength and the coupling strength.

Here we consider integrating an ultrathin polar dielectric film with gap plasmons at mid-IR frequencies. We find that the confined electric field in the gap can strongly couple to the phonon-driven ENZ mode.[5,27,28] This strong coupling is marked by a clear splitting, where the two hybrid modes inherit properties that are plasmonic and phononic in nature. In this study, we investigate the plasmon-phonon coupling in the mid-IR spectrum in a metasurface of metallic patches and a buried conductive substrate (metasurface-mediated

gap plasmon) combined with an ultra-thin film of aluminum oxide polar dielectric (phonon-driven ENZ mode). By systematically tuning the patch geometry, we demonstrate precise control over the hybridized mode positions, offering a reconfigurable platform for strong light–matter interaction in the mid-infrared regime. The results suggest new pathways for designing tunable photonic devices that take advantage of ENZ materials for applications in mid-infrared sensing, emission engineering, and nanoscale optoelectronics.

Method

The samples investigated in this study consist of a combined structure integrating a gap-plasmon antenna array with a 10-nm-thick film of aluminum oxide (Al_2O_3). The gap-plasmon antenna structure on its own is a metal–insulator–metal configuration, comprising square, 75-nm-thick gold patch antennas positioned above an optically thick titanium nitride (TiN) substrate, separated by a 200-nm-thick silicon (Si) spacer layer, as shown in Fig. 1 (a). The TiN substrate functions as an optical mirror for the antenna system, the resulting gap resonance is a function of the gap thickness and the dimensions of the gold patch metasurface. To enable coupling with the ENZ mode, a 10-nm-thick layer of polar dielectric aluminum oxide is introduced above the Si gap layer to form an integrated structure, Fig. 1 (b). Fig. 1 (c) shows a scanning electron microscopy image from a representative sample. Each of the fabricated arrays have approximately 1 mm^2 surface area which is large compared to the wavelength of observation. All metasurfaces have the same lattice constant of P = 3 μm, but with gold patch widths, W, varying from 800 to 1900 nm.

To model the reflectance spectra, we recreate a unit cell of each sample in FDTD, illuminate them with a plane wave normal to the surface, and the reflected light is collected and projected to the far-field. The permittivity models used in the simulations for gold and TiN are taken from the models or experimental data from Palik et al. and Baliaev et al., respectively.[29,30] As the phononic resonance frequencies in polar dielectrics change in thin

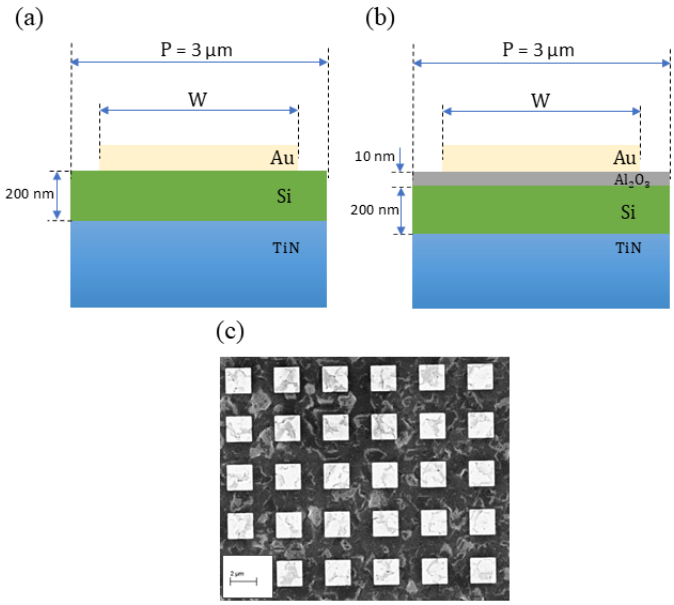

Figure 1: (a) Schematic cross-section of a unit cell of the gap plasmon sample, comprising a square gold patch antenna positioned above an optically thick titanium nitride (TiN) substrate, separated by a 200-nm-thick silicon (Si) gap layer. (b) Schematic cross-sectional of a unit cell of the combined structure, comprising square gold patch antennas with the integration of a 10-nm-thick aluminum oxide ultra-thin film supporting the ENZ mode and enabling hybridization with the gap plasmon resonances. P and W represent the array unit cell width (P=3092 nm) and gold patch width (W spans 800 to 1900 nm), respectively. (c) SEM image of a part of the fabricated gold patch antenna array with P = 3092 nm and W = 1646 nm.

films,[31] we model the real and imaginary parts of the permittivity of the Al_2O_3 thin film according to Franta et al.[32] Fig. 2 shows the real and imaginary parts of the permittivity for a thin film of aluminum oxide with the thickness of 121.5 nm reported by Franta et al.[32] Fig. 2 shows that the real part of the permittivity of aluminium oxide has zero-crossing related to longitudinal optical phonon at $\lambda = 10.8$ μm and transverse optical phonon resonance at $\lambda = 13.5$ μm.

Samples are fabricated by depositing an optically thick layer of TiN on a silicon substrate via electron beam evaporation. Subsequently, a 200 nm layer of polycrystalline silicon is deposited using RF sputtering, followed by the atomic layer deposition of a 10-nm-thick Al_2O_3 film. Arrays of gold squares (75 nm thick) with the targeted width ranging from 800 nm to 1600 nm, in 100 nm increments, were then fabricated using a standard electron beam

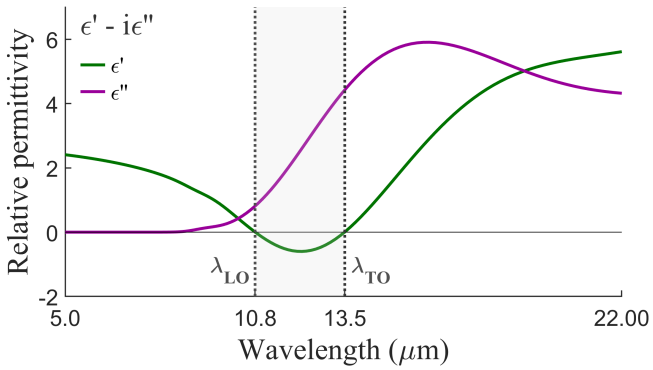

Figure 2: Real and imaginary parts of relative permittivity of thin films of the polar dielectric aluminum oxide (with the thickness of 121.5 nm) based on the model presented by Franta et al.[32] The gray area between $\lambda_{LO} = 10.8$ μm and $\lambda_{TO} = 13.5$ μm shows the Reststrahlen band over which the real part of the permittivity is negative.

lithography and lift-off process. The square arrays were patterned with a fixed periodicity of 3 μm. Gold patches are deposited using electron beam evaporation.

To characterize the coupling and thus hybridization of the gap plasmon to the phononic ENZ mode of the ultra-thin films, we measure the reflectance of gap-plasmon antenna samples with different gold patch widths, in the presence and absence of the Al_2O_3 thin film. The reflection measurements are carried out using Bruker-INVENIO Fourier transform infrared spectrometer (FTIR), attached to a Bruker-HYPERION microscope. Experimental results are compared to numerical modeling of the reflectance using Lumerical FDTD module.

Results and discussion

Fig. 3 shows the reflectance spectra for gold patch antenna arrays of patch widths spanning from 800 nm to 1900 nm with and without the Al_2O_3 thin film. The width W (in nm) is labeled on each spectrum.

First we consider the samples without the ENZ thin film, which show a clear dependence of the gap-mode resonance wavelength on patch width. As the gold patch width increases from 800 nm to 1900 nm, the gap-plasmon antenna resonance redshifts from 6.5 μm to 18

μm, with good agreement between (a) simulation and (b) experimental results showing the gap-plasmon resonance ranging from approximately 9 to 18 μm, which should span over the Reststrahlen band of an Al_2O_3 layer.

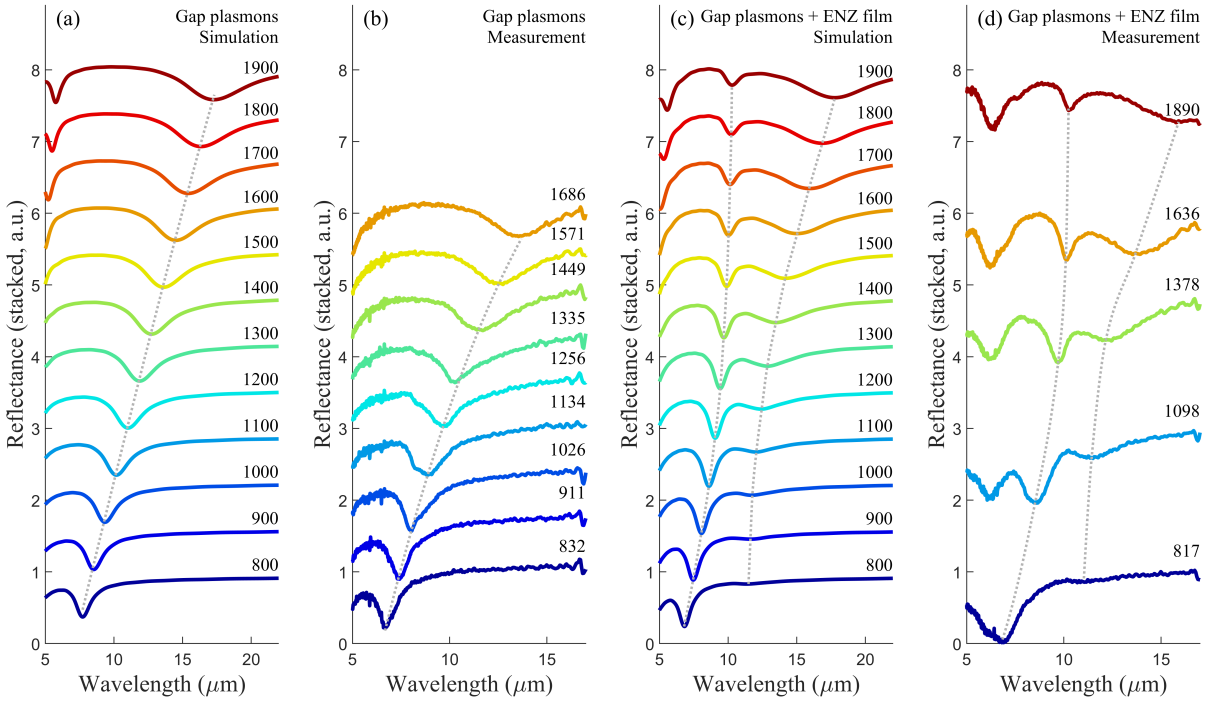

Figure 3: Reflectance from metasurfaces revealing gap plasmon mode dependence on gold patch width, W, for bare samples and samples hybridizing with 10-nm-thick aluminum oxide thin film: (a) simulation and (b) measurement results showing the reflectance spectra of the bare gap-plasmon antenna array; the gray dotted lines connect the resonance wavelengths, and W (in nm) is labeled on each spectrum. (c) Simulation and (d) measurement results showing the reflectance spectra of the combined structure; the gray dotted lines connect the resonance wavelengths of the hybridized modes. The reflectance spectra are vertically offset for better comparison of the evolution of the resonances for different gold patch width

Integrating the aluminum oxide thin film underneath the antennas leads to significant modifications in the reflectance spectra. A clear splitting of two modes emerges, with distinct anti-crossing behavior as a function of gold patch width in both (c) simulation and (d) experimental measurements. This behavior stems from the coupling between the plasmonic antenna mode and the ENZ mode of the ultra-thin aluminum oxide film, located near its LO phonon resonance.[15] This results in the formation of hybridized modes: the upper and

lower polariton branches. The gray dotted lines are fitted to the resonance wavelengths of these upper and lower polariton modes over W, demonstrating their anti-crossing.

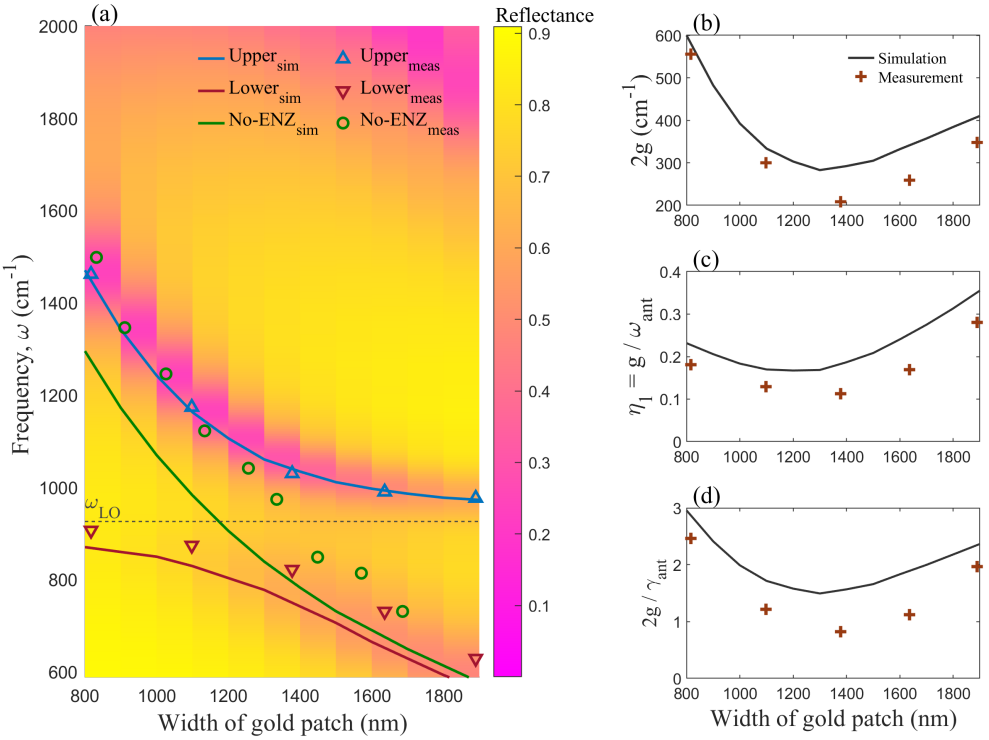

Figure 4: Measurement and numerical simulation results presenting (a) the reflectance spectra of the combined structure (gap-plasmon antenna array with the integrated 10-nm-thick aluminum oxide thin film) for different gold patch widths: The blue, red, and green solid line (markers) show the resonances of the upper, lower, and plasmon polaritons for different gold patch widths based on the simulation (measurement) results. Simulation and measurement results showing (b) level splitting, (c) normalized coupling strength, and (d) normalized mode splitting for different antenna patch widths, where g is the coupling rate (or half of the normal mode splitting). $\omega_{ant.}$ and $\gamma_{ant.}$ denote the frequency and the full width at half maximum (FWHM) of the gap-plasmon antenna resonance for each patch width, respectively. When the bare antenna resonance spectrally approaches to $\lambda_{LO} = 10.8\ \mu$m (W 1200 nm), the anti-crossing and thus the hybridization of the modes into the upper and lower polaritons is most pronounced.

Fig. 4 illustrates the experimental and numerical evidence of the strong coupling between the gap-plasmonic modes of the antennas and the lattice vibrations of aluminum oxide in the mid-IR spectrum. The magnitude of anti-crossing permits quantification of the degree of coupling between the gap plasmon and ENZ mode by determining the normalized coupling

strength, $\eta = g/\omega_{ant.}$, and normalized mode splitting, $2g/\gamma_{ant.}$, of our structure for different antenna patch widths, where g is the coupling rate (or half of normal mode splitting), $\omega_{ant.}$ and $\gamma_{ant.}$ represent the frequency and the full width half maximum (FWHM) of the gap-plasmon antenna resonance for each patch width, respectively. The mode splitting exceeds 2.8 μm with $\eta > 0.1$. All arrays exhibit modal splitting that is larger than the line width of the resonances of the bare antenna array ($2g/\gamma_{ant.} > 1$). These values confirm that the system is in the strong-coupling regime.

Next we investigate the possibility of observing ultrastrong coupling in ENZ-gap plasmon system. For very small thicknesses of the ENZ film, the ENZ mode can be modeled by a flat dispersion line as follows:[3]

$$\omega_{\text{ENZ}}(\mathbf{k}_{\parallel}) = \omega_{0,\text{ENZ}} - \frac{i}{2}\,\gamma_{\text{Al}_2\text{O}_3}, \tag{1}$$

where $\omega_{0,\text{ENZ}} = 925.9$ cm^{-1} is the frequency of the ENZ mode and $\gamma_{\text{Al}_2\text{O}_3} = 282.5$ cm^{-1} is the damping in the permittivity of Al_2O_3, extracted from the permittivity model reported in Fig .2. The coupling strength of the system depends on the spatial overlap between the gap plasmon and ENZ modes, and can be tuned by varying the ENZ material properties and film thickness. Fig. 5(a) shows numerically calculated reflectance spectra for ENZ film thicknesses ranging from 2 nm to 100 nm, with the gold patch width fixed at W=1200 nm. At this width, the resonance of the bare gap-plasmon antenna overlaps with the longitudinal optical (LO) phonon resonance of the ENZ layer (see Fig. 3(a)). A clear resonance splitting indicative of strong coupling is observed for ENZ thicknesses below 20 nm.

Fig. 5 (b) and (c) present the extracted coupling strength and normalized mode splitting as functions of ENZ thickness. As shown, the resonance splitting increases nearly linearly from 2 nm to 20 nm. For larger thicknesses, however, the behavior transitions to a sub-linear regime, approximately following a $\sqrt{h}$ dependence, as indicated by the fitted dashed curves. These empirical fits follow the form $a\sqrt{h} + b$, where the fitting parameters are $a = 0.039$, $b = 0.03$ for panel (b), and $a = 0.25$, $b = 0.2$ for panel (c). This reduction in coupling

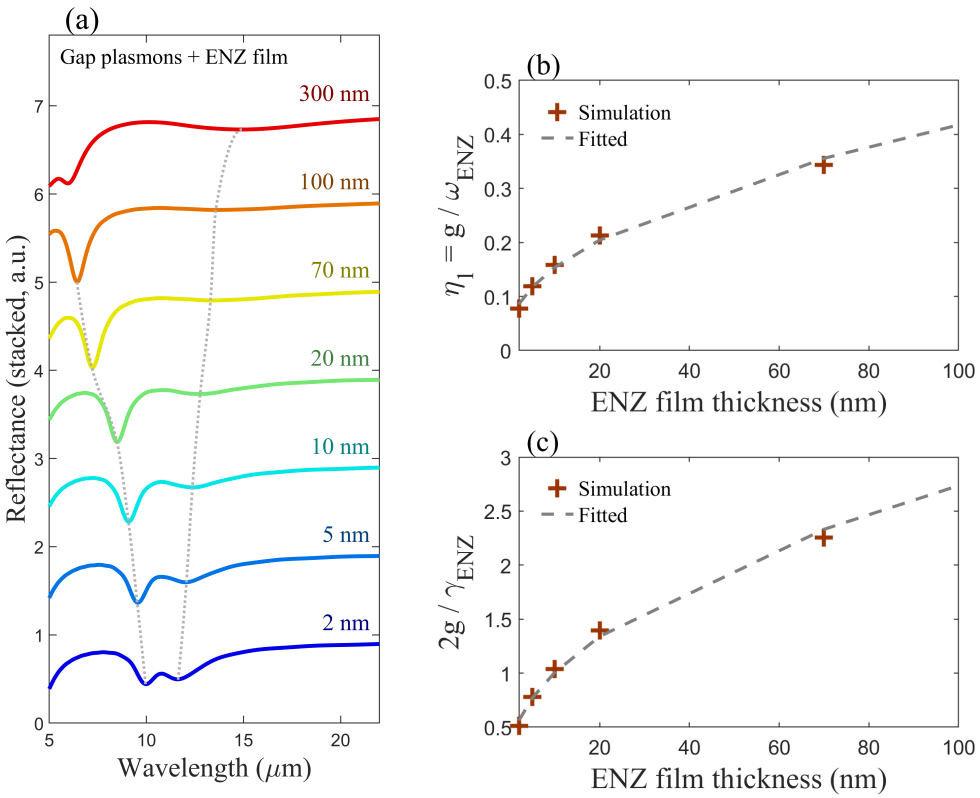

Figure 5: (a) The reflectance spectra are vertically offset for better comparison of the evolution of the resonances for different ENZ film thicknesses, with P = 3 μm and W = 1200 nm. The value of h is labeled on each spectrum. The gray dotted lines connect the resonance wavelengths of the upper and lower polaritons. (b) Normalized coupling strength, and (c) Normalized mode splitting for different ENZ film thicknesses, where g is the coupling rate (or half of the normal mode splitting), and ω_{ENZ} and γ_{ENZ} denote the frequency and full width at half maximum (FWHM) of the ENZ mode based on the flat dispersion approximation, Eq.1, respectively. The fitted curves shown in (b) and (c) follow the empirical relation $a\sqrt{h} + b$, capturing the observed $\sqrt{h}$-dependence of the coupling as the ENZ film thickness increases.

behaviour can be attributed to changes in the quality of the ENZ mode: as the ENZ film becomes thicker, the electric field distribution deviates from the uniform profile characteristic of the ENZ condition. A degradation in the quality of the ENZ mode leads to a degradation of the coupling. Nevertheless, we find that for an aluminium oxide thickness of slightly larger than 20 nm the system begins to show ultrastrong coupling.[3]

Conclusions

In summary, we have demonstrated strong coupling between gap plasmon modes and the ENZ phonon polariton of a polar dielectric film using a coupled system of gold patch antennas deposited on top of an ultrathin aluminum oxide layer. The degree of strong coupling is exhibited by modal splitting that exceeds the bandwidth of the bare antenna resonances and a normalized coupling strength $\eta > 0.1$. The observed mode splitting and anti-crossing behavior confirm the formation of hybrid plasmon–phonon polaritons, combining the benefits of field confinement from plasmonic structures with the long lifetimes of phonon modes. This coupling between LO phonons in the ENZ mode of the thin film and free-space optical modes could be an avenue toward manipulating the thermal emission of the system, opening pathways toward actively tunable thermal emitters, surface-enhanced sensing, and compact mid-infrared photonic components leveraging ENZ materials.

Our approach gives rise to tunable hybridized polariton modes by varying the antenna geometry, providing a robust and versatile scheme for engineering mid-IR light–matter interactions. While gap plasmons are principally dependent on the spacer thickness between the two conductive layers, we show here that using a metasurface as one layer not only greatly facilitates optical coupling from free space, but also the metasurface properties, such as the gold patch width, provide an additional parameter by which to tune the gap plasmon and optimize coupling to the ENZ mode. Further investigation of metasurface designs coupled to phonon-driven ENZ modes could reveal additional pathways to manipulating thermal emission. Furthermore, just as metasurface coupling to plasmon-driven ENZ modes in plasmonic thin films led to an order-of-magnitude increase in nonlinear optical responses in the near-infrared regime, it is possible that metasurface coupling to phonon-driven ENZ modes in the mid-infrared could have analogous benefits, which would have major implications for research into mid-infrared nonlinear optics.

Acknowledgement

This work was supported by the Natural Science and Engineering Council of Canada under Discovery Grant RGPIN/2017-06880 and by the Canada Research Chairs program under award 950-231657. In addition, RWB acknowledges support through the US Office of Naval Research MURI award N00014-20-1-2558, US National Science Foundation Award 2138174. The research performed by M.K. at the Air Force Research Laboratory was supported by contract award FA807518D0015. J.R.H. and S.V. acknowledge support from the Air Force Office of Scientific Research under award number FA9550-25RYCOR006 and FA9550-23RYCOR001, respectively.

References

(1) Bishop, L. S.; Chow, J. M.; Koch, J.; Houck, A. A.; Devoret, M. H.; Thuneberg, E.; Girvin, S. M.; Schoelkopf, R. J. Nonlinear response of the vacuum Rabi resonance. *Nature Physics* **2009**, *5*, 105–109.

(2) Karimi, M.; Awan, K. M.; Vaddi, Y.; Alaee, R.; Upham, J.; Alam, M. Z.; Boyd, R. W. Interactions of Fundamental Mie Modes with Thin Epsilon-near-Zero Substrates. *Nano Letters* **2023**, *23*, 11555–11561, PMID: 38038228.

(3) Choudhary, S.; Iqbal, S.; Karimi, M.; Reshef, O.; Alam, M. Z.; Boyd, R. W. Strongly Coupled Plasmon Polaritons in Gold and Epsilon-Near-Zero Bifilms. *ACS Photonics* **2023**, *10*, 162–169.

(4) Choudhary, S.; De Leon, I.; Swiecicki, S.; Awan, K. M.; Schulz, S. A.; Upham, J.; Alam, M. Z.; Sipe, J. E.; Boyd, R. W. Weak superradiance in arrays of plasmonic nanoantennas. *Phys. Rev. A* **2019**, *100*, 043814.

(5) Liu, Y.; Willis, R. F. Plasmon-phonon strongly coupled mode in epitaxial graphene. *Phys. Rev. B* **2010**, *81*, 081406.

(6) Lagos, M. J.; Batson, P. E.; Lyu, Z.; Hohenester, U. Imaging Strongly Coupled Plasmon–Phonon Modes in Mid-Infrared Double Antennas. *ACS Photonics* **2021**, *8*, 1293–1300.

(7) Alù, A.; Silveirinha, M. G.; Salandrino, A.; Engheta, N. Epsilon-near-zero metamaterials and electromagnetic sources: Tailoring the radiation phase pattern. *Phys. Rev. B* **2007**, *75*, 155410.

(8) Alam, M. Z.; Leon, I. D.; Boyd, R. W. Large optical nonlinearity of indium tin oxide in its epsilon-near-zero region. *Science* **2016**, *352*, 795–797.

(9) Gui, Y.; Miscuglio, M.; Ma, Z.; Tahersima, M. H.; Sun, S.; Amin, R.; Dalir, H.; Sorger, V. J. Towards integrated metatronics: a holistic approach on precise optical and electrical properties of Indium Tin Oxide. *Scientific Reports* **2019**, *9*, 11279.

(10) Wang, Y.; colleagues Broadband frequency translation through time refraction in indium–tin-oxide epsilon-near-zero films. *Nature Communications* **2020**, *11*.

(11) Caspani, L.; Kaipurath, R. P. M.; Clerici, M.; Ferrera, M.; Roger, T.; Kim, J.; Kinsey, N.; Pietrzyk, M.; Di Falco, A.; Shalaev, V. M.; Boltasseva, A.; Faccio, D. Enhanced Nonlinear Refractive Index in ϵ-Near-Zero Materials. *Phys. Rev. Lett.* **2016**, *116*, 233901.

(12) Alam, M. Z.; Schulz, S. A.; Upham, J.; Leon, I. D.; Boyd, R. W. Large optical nonlinearity of nanoantennas coupled to an epsilon-near-zero material. *Nature Photonics* **2018**, *12*, 79–83.

(13) Schulz, S. A. et al. Roadmap on photonic metasurfaces. *Applied Physics Letters* **2024**, *124*, 260701.

(14) Caldwell, J. D.; Kretinin, A.; Chen, Y.; others Sub-diffractional volume-confined po-

laritons in the natural hyperbolic material hexagonal boron nitride. *Nature Communications* **2014**, *5*, 1–7.

(15) Vassant, S.; Hugonin, J.-P.; Marquier, F.; Greffet, J.-J. Berreman mode and epsilon near zero mode. *Optics Express* **2012**, *20*, 23971–23977.

(16) Rivera, N.; Christensen, T. K.; Narang, P. Phonon Polaritonics in Two-Dimensional Materials. *Nano Letters* **2019**, *19*, 2653–2660.

(17) Nordin, L.; Dominguez, O.; Roberts, C. M.; Streyer, W.; Feng, K.; Fang, Z.; Podolskiy, V. A.; Hoffman, A. J.; Wasserman, D. Mid-infrared epsilon-near-zero modes in ultra-thin phononic films. *Applied Physics Letters* **2017**, *111*, 091105.

(18) Caldwell, J. D.; Lindsay, L.; Giannini, V.; Vurgaftman, I.; Reinecke, T. L.; Maier, S. A.; Glembocki, O. J. Low-loss, infrared and terahertz nanophotonics using surface phonon polaritons. *Nanophotonics* **2015**, *4*, 44–68.

(19) Ziman, J. M. *Principles of the Theory of Solids*; Cambridge University Press: Cambridge, 1972.

(20) Passler, N. C.; Gubbin, C. R.; Folland, T. G.; Razdolski, I.; Katzer, D. S.; Storm, D. F.; Wolf, M.; De Liberato, S.; Caldwell, J. D.; Paarmann, A. Strong Coupling of Epsilon-Near-Zero Phonon Polaritons in Polar Dielectric Heterostructures. *Nano Letters* **2018**, *18*, 4285–4292, PMID: 29894195.

(21) Dass, C. K.; Kwon, H.; Vangala, S.; Smith, E. M.; Cleary, J. W.; Guo, J.; Alù, A.; Hendrickson, J. R. Gap-Plasmon-Enhanced Second-Harmonic Generation in Epsilon-Near-Zero Nanolayers. *ACS Photonics* **2020**, *7*, 174–179.

(22) Schulz, S. A.; Tahir, A. A.; Alam, M. Z.; Upham, J.; De Leon, I.; Boyd, R. W. Optical response of dipole antennas on an epsilon-near-zero substrate. *Phys. Rev. A* **2016**, *93*, 063846.

(23) Luxmoore, I. J.; Gan, C. H.; Liu, P. Q.; Valmorra, F.; Li, P.; Faist, J.; Nash, G. R. Strong Coupling in the Far-Infrared between Graphene Plasmons and the Surface Optical Phonons of Silicon Dioxide. *ACS Photonics* **2014**, *1*, 1151–1155.

(24) Hendrickson, J. R.; Vangala, S.; Dass, C.; Gibson, R.; Goldsmith, J.; Leedy, K.; Walker, D. E. J.; Cleary, J. W.; Kim, W.; Guo, J. Coupling of Epsilon-Near-Zero Mode to Gap Plasmon Mode for Flat-Top Wideband Perfect Light Absorption. *ACS Photonics* **2018**, *5*, 776–781.

(25) Yoo, D.; de León-Pérez, F.; Pelton, M.; Lee, I.-H.; Mohr, D. A.; Raschke, M. B.; Caldwell, J. D.; Martín-Moreno, L.; Oh, S.-H. Ultrastrong plasmon–phonon coupling via epsilon-near-zero nanocavities. *Nature Photonics* **2021**, *15*, 125–130.

(26) Xu, H.; Yang, M.; Chen, Y. Strong Coupling of Epsilon-Near-Zero Mode to Graphene Plasmon for Optimizing Propagation Length and Optical Field Confinement. *The Journal of Physical Chemistry C* **2022**, *126*, 4024–4029.

(27) Gallina, P.; Konečná, A.; Liška, J. c. v.; Idrobo, J. C.; Šikola, T. c. v. Strongly Coupled Plasmon and Phonon Polaritons as Seen by Photon and Electron Probes. *Phys. Rev. Appl.* **2023**, *19*, 024042.

(28) Shelton, D.; Brener, I.; Ginn, J. C.; Sinclair, M. B.; Peters, D. W.; Coffey, K. R.; Boreman, G. D. Strong Coupling between Nanoscale Metamaterials and Phonons. *Nano Letters* **2011**, *11*, 2104–2108, PMID: 21462937.

(29) Palik, E. D. *Handbook of Optical Constants of Solids*; Academic Press, 1998.

(30) Beliaev, L. Y.; Shkondin, E.; Lavrinenko, A. V.; Takayama, O. Titanium Nitride Nanotrench Metasurfaces for Mid-infrared Chemical Sensing. *ACS Applied Optical Materials* **2024**, *2*, 88–96.

(31) Kischkat, J.; Peters, S.; Gruska, B.; Semtsiv, M.; Chashnikova, M.; Klinkmüller, M.; others Mid-infrared optical properties of thin films of aluminum oxide, titanium dioxide, silicon dioxide, aluminum nitride, and silicon nitride. *Applied Optics* **2012**, *51*, 6789–6798.

(32) Franta, D.; Nečas, D.; Ohlídal, I.; Giglia, A. Dispersion model for optical thin films applicable in wide spectral range. *SPIE* **2015**, *9628*, 96281U.

Chapter 4

Field enhancement in the mid-IR regime using ENZ material

In the previous chapter, we demonstrated the strong coupling between gap plasmon resonances and the ENZ phonon polariton mode supported by an ultra-thin polar dielectric film. This interaction gives rise to hybridized polaritonic states, featuring highly localized electromagnetic fields and altered dispersion characteristics. A notable advantage of this structure is the significant electric field enhancement (FE) within the ENZ layer, which is particularly relevant for nonlinear optical applications where the response scales with the local field intensity. Recent studies have shown that Drude-type epsilon–near–zero (ENZ) resonances can dramatically enhance optical nonlinearities; when a plasmonic resonance is strongly coupled to an ENZ mode, the nonlinear response has been boosted by tens-fold (typically $\sim 30\times$), owing to subwavelength field compression and an almost uniform electric field within the ENZ film [1, 2, 3, 4]. Motivated by these results, we numerically investigate the field enhancement in a gap-plasmon/ENZ architecture, targeting the hybrid mode that maximizes electric-field energy in the ENZ layer while keeping losses and radiative coupling practical [5, 6].

In this chapter, we present a numerical investigation of the electric field enhancement as a function of the ENZ film thickness. Employing full-wave electromagnetic simulations using the Lumerical FDTD module, we show that the strong mode localization and hybridization can produce field intensities several orders of magnitude higher than the incident field. These findings highlight the potential of ENZ-coupled gap plasmon antennas as an effective platform for mid-infrared nonlinear optics, including second-harmonic generation (SHG), as well as third order nonlinear responses.

4.1 Introduction

To derive the mathematical framework for nonlinear optical response of a medium, we begin with Maxwell's equations. These fundamental equations govern the behavior of electric field **E**, electric displacement field **D**, magnetic field **H**, and magnetic flux density **B**. In differential form, Maxwell's equations for a linear and nonmagnetic material containing no free charges or free current are expressed as:

$$\nabla \cdot \mathbf{D} = 0 \tag{4.1}$$

$$\nabla \times \mathbf{E} = -\frac{\partial \mathbf{B}}{\partial t} \tag{4.2}$$

$$\nabla \cdot \mathbf{B} = 0 \tag{4.3}$$

$$\nabla \times \mathbf{H} = \frac{\partial \mathbf{D}}{\partial t} \tag{4.4}$$

For materials characterized by a complex permittivity, the permittivity ϵ can be expressed as:

$$\epsilon = \epsilon' + i\epsilon'' = \epsilon_0 \left(1 + \chi' + i\chi''\right), \tag{4.5}$$

where ϵ' and ϵ'' are the real and imaginary parts of the permittivity, respectively, and χ' and χ'' represent the real and imaginary parts of the electric susceptibility. We also assume material is nonmagnetic so that $\tilde{\mathbf{B}} = \mu_0 \tilde{\mathbf{H}}$.

An applied electric field results in the creation of electric dipole moments inside the material. Consequently, $\tilde{\mathbf{D}}$, is a function of both the external electric field, $\tilde{\mathbf{E}}$, and the material's dipole moment per unit volume, $\tilde{\mathbf{P}}$ (all in the phasor domain):

$$\tilde{\mathbf{D}} = \epsilon_0 \tilde{\mathbf{E}} + \tilde{\mathbf{P}}, \tag{4.6}$$

The polarization vector $\tilde{\mathbf{P}}$ has both linear and nonlinear parts. Assuming that the nonlinear response is only perturbative to the linear response, $\tilde{\mathbf{P}}$ can be expressed as a power series expansion to include the nonlinear response [7]:

$$\tilde{\mathbf{P}} = \epsilon_0 [\chi^{(1)} \tilde{\mathbf{E}} + \chi^{(2)} \tilde{\mathbf{E}}^2 + \chi^{(3)} \tilde{\mathbf{E}}^3 + \ldots], \tag{4.7}$$

where $\chi^{(n)}$ is the nth-order susceptibility tensor that describes the response of the material to the applied electric field. The linear optical response of a material is described by the $\chi^{(1)}$ term, whereas higher-order terms such as $\chi^{(2)}$, and $\chi^{(3)}$ correspond

to its nonlinear optical response. We can express the displacement field as:

$$\tilde{\mathbf{D}} = \epsilon_0(1+\chi^{(1)})\tilde{\mathbf{E}} + \tilde{\mathbf{P}_{\mathbf{NL}}} = \epsilon_0\epsilon_r\tilde{\mathbf{E}} + \tilde{\mathbf{P}_{NL}}, \tag{4.8}$$

where $\epsilon_r = 1 + \chi^{(1)}$ is linear relative permittivity and $\tilde{P}^{NL}$ is nonlinear optical polarization of the material. The nonlinear polarization plays a key role in the nonlinear optical response since it can act as a source of new components of the electromagnetic field according to the following equation:

$$\nabla^2\tilde{\mathbf{E}} - \frac{1}{c^2}\frac{\partial^2}{\partial t^2}\tilde{\mathbf{E}} = \frac{1}{\epsilon_0 c^2}\frac{\partial^2\tilde{\mathbf{P}}}{\partial t^2}, \tag{4.9}$$

Alternatively, the nonlinear wave equation is:

$$\nabla^2\tilde{\mathbf{E}} - \frac{\epsilon_r}{c^2}\frac{\partial^2}{\partial t^2}\tilde{\mathbf{E}} = \frac{1}{\epsilon_0 c^2}\frac{\partial^2\tilde{\mathbf{P}}^{NL}}{\partial t^2}. \tag{4.10}$$

While the present chapter concentrates on numerical field-enhancement analysis in the mid-infrared, we have experimentally investigated third-order nonlinear response in a metal–dielectric ENZ multilayer using the Z–scan technique in the visible range (410–600 nm). Appendix **??** provides a detailed description of the experimental setup, beam characterization, and representative open- and closed-aperture Z–scan measurements, which form a complementary platform for future nonlinear experiments on ENZ-coupled structures.

4.2 Motivation

In a material with a vanishingly small linear permittivity ($\epsilon \to 0$), the nonlinear wave equation can be expressed as below and can be concluded that the optical response of the material can be strongly affected by the nonlinear properties under ENZ condition:

$$\nabla^2\tilde{\mathbf{E}} = \frac{1}{\epsilon_0 c^2}\frac{\partial^2\tilde{\mathbf{P}}^{NL}}{\partial t^2}. \tag{4.11}$$

Nonlinear optical processes, such as second-harmonic generation (SHG), third-harmonic generation (THG), and difference-frequency generation, are inherently weak in most materials due to the small magnitude of their nonlinear susceptibilities. These processes depend nonlinearly on the electric field, often scaling with the square or cube of the field amplitude. As a result, significant nonlinear effects typically require

either high-intensity light sources or engineered structures that can locally amplify the electromagnetic field. Field enhancement is thus a critical factor in enabling and boosting nonlinear optical responses. The electric field enhancement factor is defined as:

$$\mathbf{F} = \frac{|\mathbf{E}|}{|\mathbf{E_0}|} \tag{4.12}$$

where $|\mathbf{E}|$ is the electric field amplitude inside the structure and $|\mathbf{E_0}|$ is the incident field amplitude.

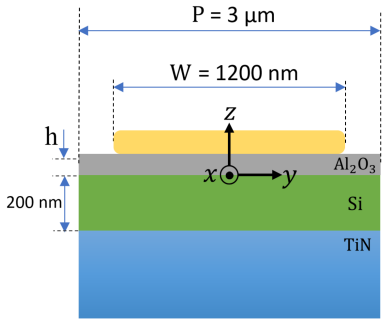

FIGURE 4.1: Schematic cross-sectional view of a unit cell of the combined structure, comprising square gold patch antennas with the integration of a aluminum oxide ultra-thin film supporting the ENZ mode and enabling hybridization with the gap plasmon resonances. P = 3 μm represent the array unit cell and and W = 1200 nm is the width of gold patches.

By concentrating electromagnetic energy into subwavelength volumes—particularly in regions of high field confinement—materials can exhibit dramatically increased nonlinear polarization, even under moderate incident power. This makes structures with strong local field enhancement highly attractive for integrated nonlinear optics, especially in platforms where power efficiency or device footprint is a concern. In the context of our structure, the strong coupling between the gap plasmon mode and the ENZ phonon polariton mode not only modifies the dispersion relation but also leads to the formation of hybrid states with intense localized fields. These hybrid modes are capable of producing electric field intensities several orders of magnitude greater than the incident field, particularly within the ENZ layer where the permittivity approaches zero. To quantify this effect, we performed full-wave electromagnetic simulations using the Lumerical FDTD solver. Our results demonstrate substantial field enhancement in the ENZ region, with the maximum enhancement strongly dependent on the thickness of the ENZ film. These findings confirm that the designed structure supports highly confined hybrid modes, making it a promising candidate for mid-infrared nonlinear optical applications.

4.3 Results and Discussion

We begin by examining the evolution of hybridized gap-plasmons and phonon polariton modes as a function of the ENZ film thickness. The structure is shown in Fig. 4.1 where the sample is illuminated with plane wave under normal angle with the electric field aligned in x direction.

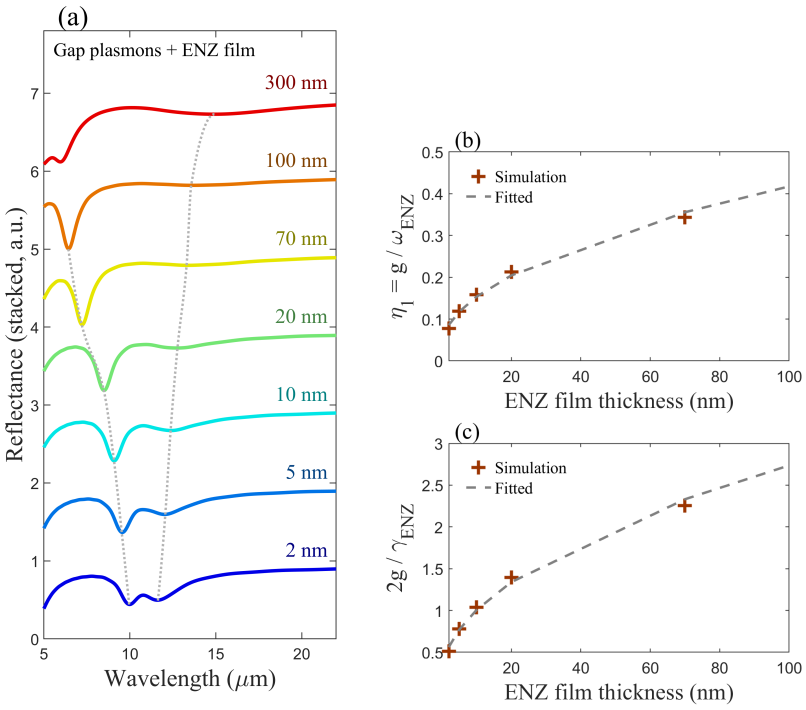

FIGURE 4.2: (a) The reflectance spectra are vertically offset for better comparison of the evolution of the resonances for different ENZ film thicknesses, with P = 3 μm and W = 1200 nm. The value of h is labeled on each spectrum. The gray dotted lines connect the resonance wavelengths of the upper and lower polaritons. (b) Normalized coupling strength, and (c) Normalized mode splitting for different ENZ film thicknesses, where g is the coupling rate (or half of the vacuum Rabi splitting), and ω_{ENZ} and γ_{ENZ} denote the frequency and full width at half maximum (FWHM) of the ENZ mode based on the flat dispersion approximation, (see Eq. 1 in chapter 3), respectively. The fitted curves shown in (b) and (c) follow the empirical relation $a\sqrt{\text{h}}+b$, capturing the observed $\sqrt{\text{h}}$-dependence of the coupling as the ENZ film thickness increases.

In previous chapter we discussed that the coupling strength of the system depends on the spatial overlap between the gap plasmons and the ENZ mode, and can be tuned by varying the ENZ material properties and film thickness. Fig. 4.2(a) shows numerically calculated reflectance spectra for ENZ film thicknesses ranging from 2 nm to 100 nm, with the gold patch width fixed at W=1200 nm. At this width, the resonance of the bare gap-plasmon antenna overlaps with the longitudinal optical (LO)

phonon resonance of the ENZ film. A clear resonance splitting—indicative of strong coupling—is observed for ENZ thicknesses below 20 nm. The reflectance minima trace out two distinct branches (gray dotted lines) corresponding to the upper and lower polariton modes, arising from coupling between the gap plasmon resonance and the ENZ phonon polariton.

Fig. 4.2 (b) and (c) present the extracted coupling strength and normalized mode splitting as functions of ENZ thickness. As shown, the resonance splitting increases nearly linearly from 2 nm to 20 nm. For larger thicknesses, however, the behavior transitions to a sub-linear regime, approximately following a $\sqrt{\mathrm{h}}$ dependence, as indicated by the fitted dashed curves. These empirical fits follow the form $a\sqrt{\mathrm{h}} + b$, where the fitting parameters are $a = 0.039$, $b = 0.03$ for panel (b), and $a = 0.25$, $b = 0.2$ for panel (c). For an ultrathin ENZ film of thickness $h \ll \lambda$, the collective light–matter coupling (mode splitting) follows the standard many-oscillator scaling $g \propto \sqrt{\mathrm{N_{eff}}}$, where the effective number of dipoles participating scales with the active volume. With constant areal density, $\mathrm{N_{eff}} \propto \mathrm{h}$, and therefore $g \propto \sqrt{\mathrm{h}}$. This scaling also emerges from Hopfield-type treatments of phonon–polaritons, where the coupling depends on the oscillator strength per unit area (linear in h) [7, 5, 8, 9, 6]. The observed $\sqrt{\mathrm{h}}$ trend in our data is thus expected in the ultrathin limit. This reduction in coupling efficiency can be attributed to changes in the quality of the ENZ mode: as the ENZ film becomes thicker, the electric field distribution deviates from the uniform profile characteristic of the ENZ condition. Consequently, the mode becomes more dispersive and the overlap with the plasmonic mode weakens, limiting the strength of hybridization. In the following paragraphs, we present the calculated field enhancement of these hybridized modes.

A key consequence of this strong coupling is the significant local field enhancement inside the ENZ layer, which is critical for nonlinear optical applications. To quantify this, we performed FDTD simulations of the structure with the patch edges rounded with a 10 nm radius of curvature to avoid scattering due to sharp edges. Fig. 4.3 and Fig. 4.4 display a cross-sectional views (in the YZ plane) of the electric field enhancement within the ENZ layer for the upper and lower polariton resonances for different ENZ film thicknesses (the full cross-sectional views are labeled a1–g1, and the zoomed-in view around the ENZ layer are labeled a2–g2), respectively. Intense field localization is observed inside the ENZ layer, particularly for thin ENZ films smaller than 20 nm. The electric field distribution on the Z-axis (under and close

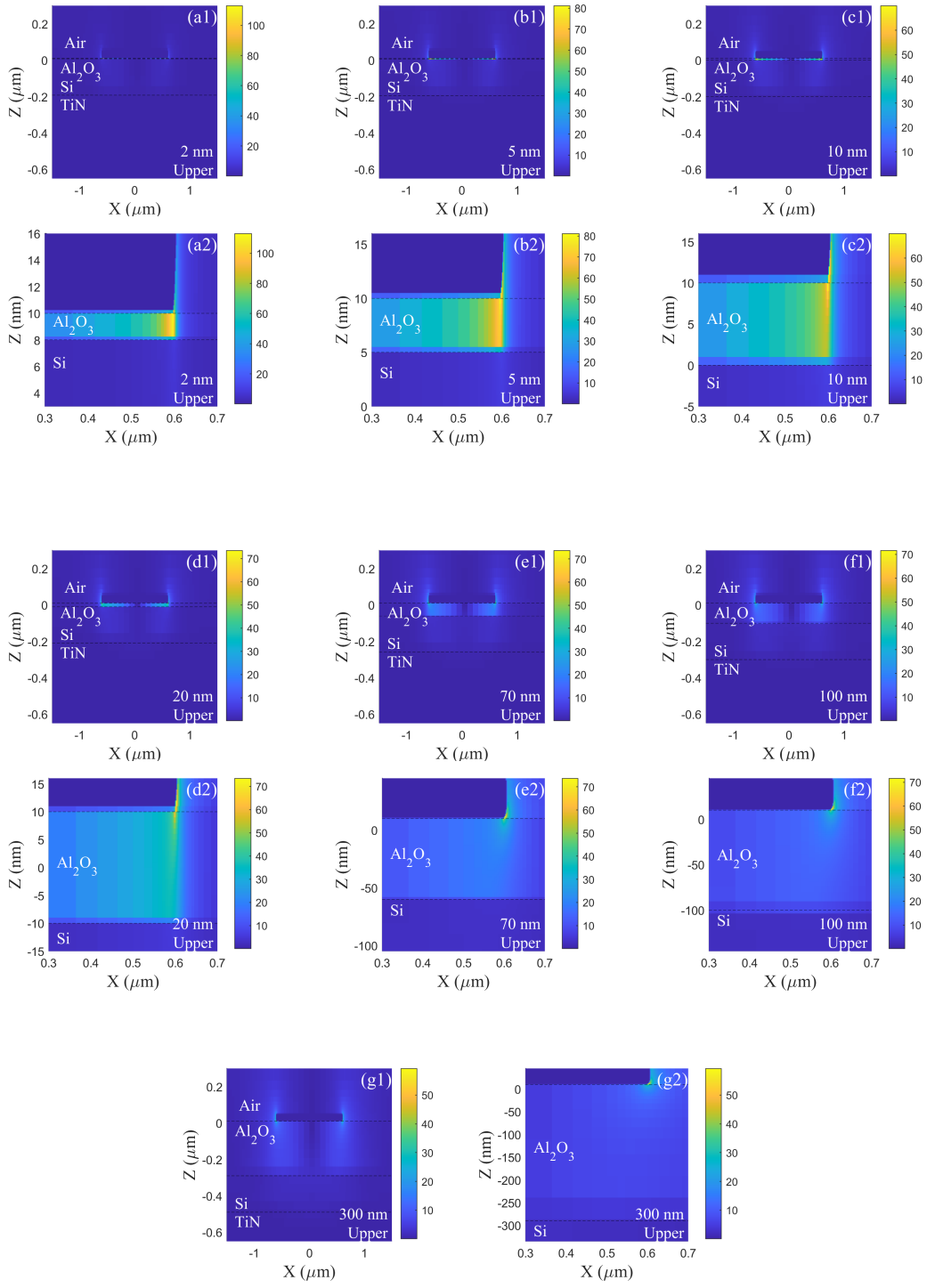

FIGURE 4.3: Numerically calculated electric field enhancement distributions at the upper polariton mode in the YZ cross-section of the structure for ENZ film thicknesses ranging from 2 to 300 nm, with gold patch width W = 1200 nm and period P = 3 μm. For each ENZ thickness, two panels are shown: the full cross-sectional view (top row, labeled a1–g1) and a zoomed-in view around the ENZ layer (bottom row, labeled a2–g2). These pairs illustrate how the field localization evolves with increasing ENZ thickness, particularly within and near the ENZ region.

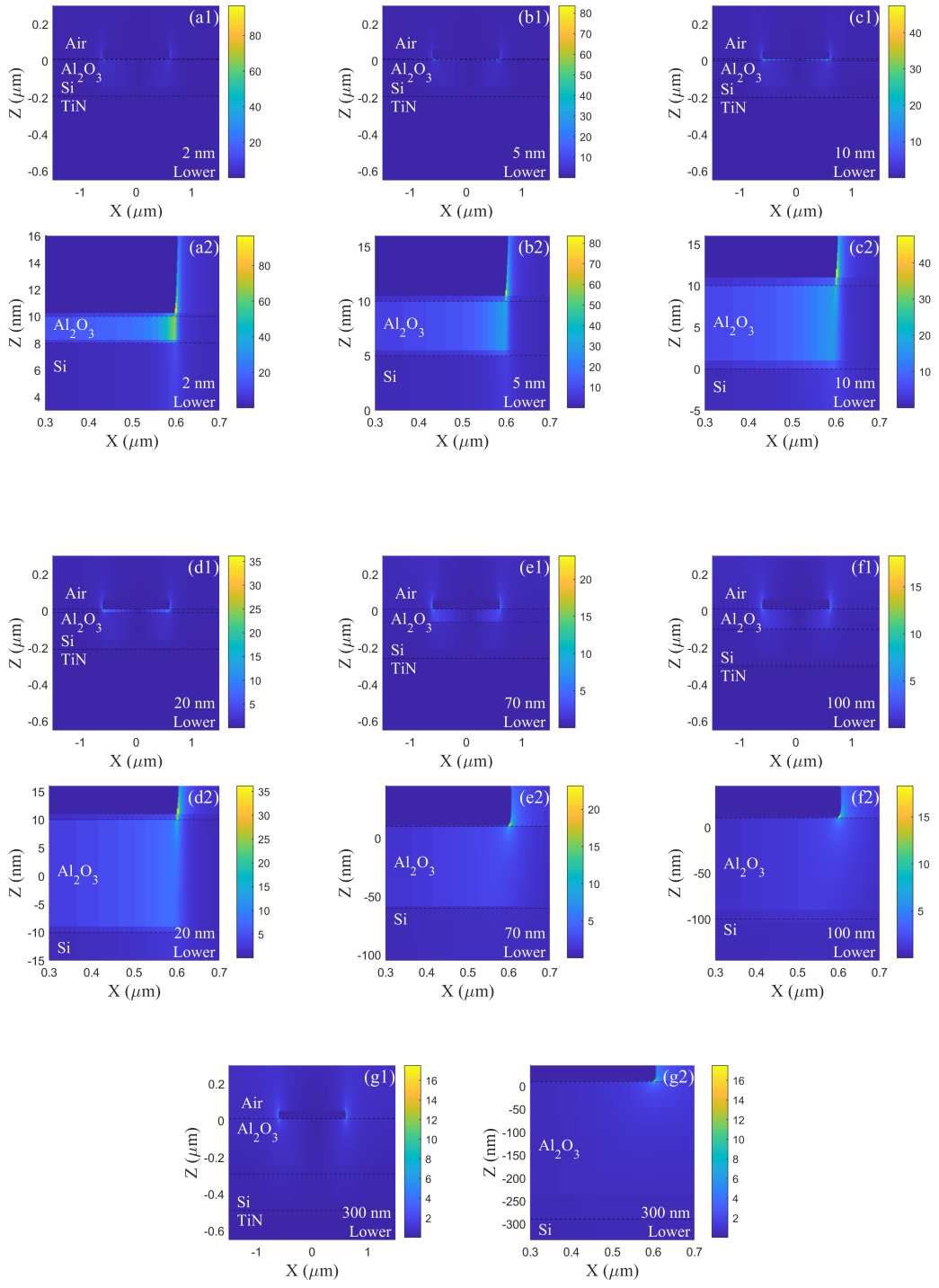

FIGURE 4.4: Numerically calculated electric field enhancement distributions at the lower polariton mode in the YZ cross-section of the structure for ENZ film thicknesses ranging from 2 to 300 nm, with gold patch width W = 1200 nm and period P = 3 μm. For each ENZ thickness, two panels are shown: the full cross-sectional view (top row, labeled a1–g1) and a zoomed-in view around the ENZ layer (bottom row, labeled a2–g2). These pairs illustrate how the field localization evolves with increasing ENZ thickness, particularly within and near the ENZ region.

to the edges of the gold patches at approximately y = 580 nm) is demonstrated in Fig. 4.5 for the upper and Fig. 4.6 for the lower polariton modes for each ENZ film thickness (a-g). The gray patch area represents the ENZ layer. As observed the field enhancement of almost 40 to 70 is achieved for ENZ film thicknesses smaller than 10 nm at upper polariton resonance and up to 50 at lower polariton resonance.

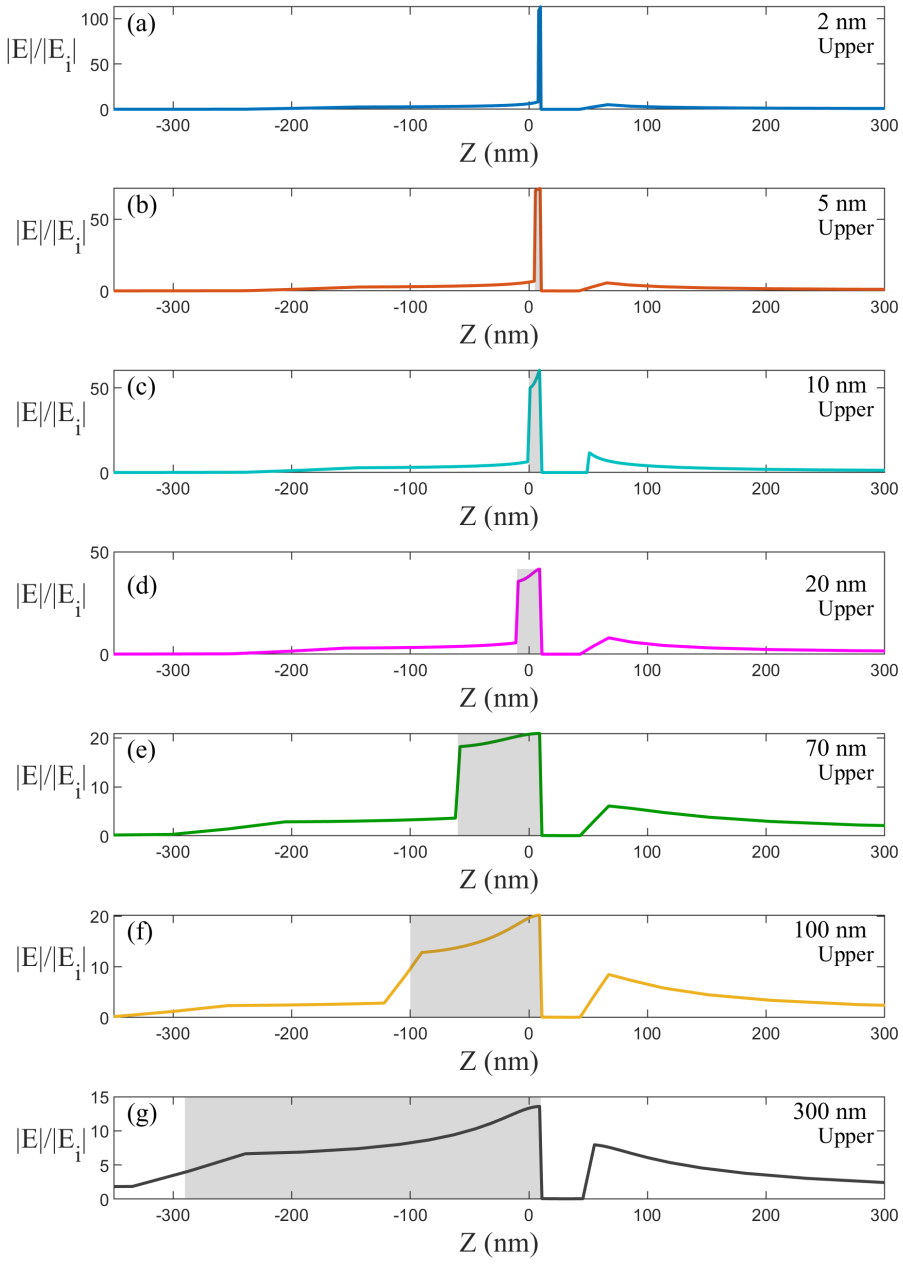

FIGURE 4.5: Numerically calculated field enhancement at upper polariton mode on the cross section of the structure in YZ plane (close to the edge of the gold patches at approximately y = 590 nm) for different ENZ film thicknesses from 2 to 300 nm (a-g); with P = 3 μm and W = 1200 nm. The gray patch area represents the ENZ layer.

Fig. 4.7 (a) and (b) combine the FE reported in Fig. 4.5 and Fig. 4.6 to show

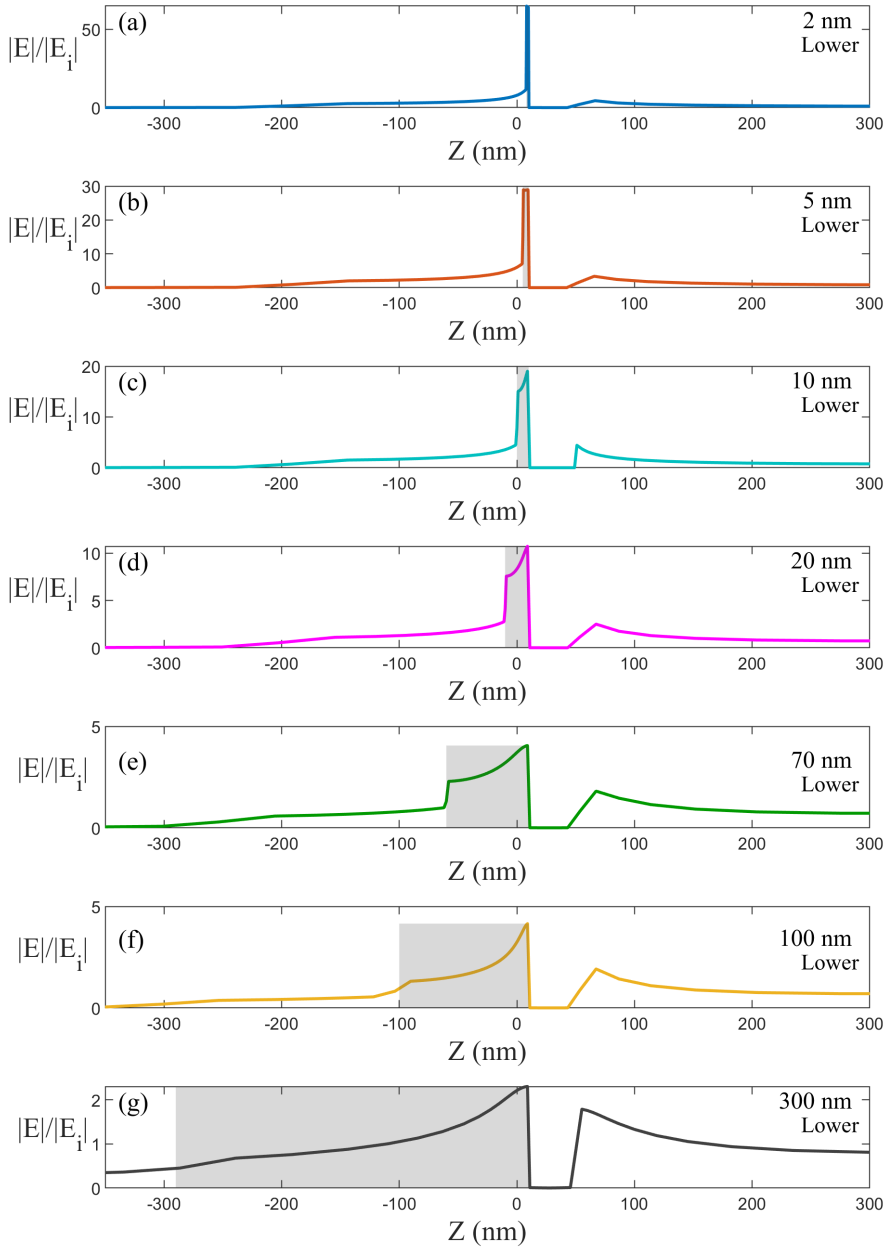

FIGURE 4.6: Numerically calculated field enhancement at lower polariton mode on the cross section of the structure in YZ plane (close to the edge of the gold patches at approximately y = 590 nm) for different ENZ film thicknesses from 2 to 300 nm (a-g); with P = 3 μm and W = 1200 nm. The gray patch area represents the ENZ layer.

the relative strength of the calculated FE for upper and lower polaritons for different ENZ film thicknesses. Moreover, for a better comparison, the maximum field enhancement vs. different ENZ film thicknesses is shown in Fig. 4.8. The field enhancement decreases significantly as the ENZ-film thickness increases, and almost no enhancement is obtained for thicknesses larger than 70 nm for both upper and lower polariton

modes. This result suggests that the ENZ layer thickness can be optimized to maximize nonlinear interaction strength. As observed, the field enhancement reaches a maximum for thicknesses in the range of 5–10 nm, where the ENZ mode is strongly confined and resonantly hybridized with the gap plasmon mode. Beyond 10 nm, ENZ confinement weakens, and the enhancement correspondingly decreases.

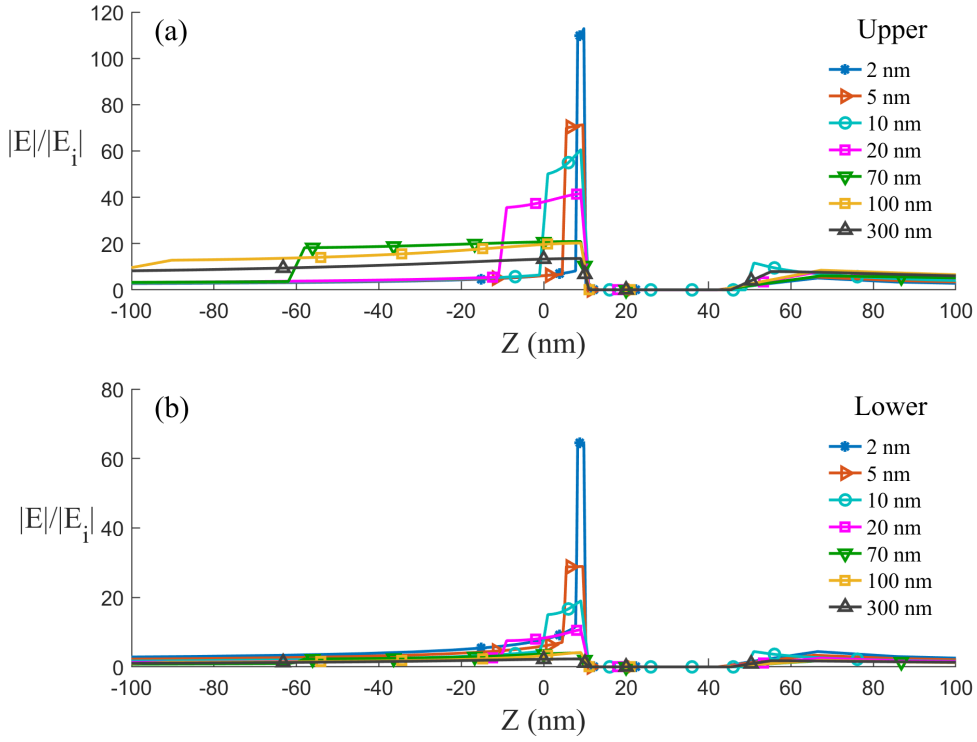

FIGURE 4.7: Comparison of the numerically calculated field enhancement at upper (a) and lower(b) polariton mode on the cross section of the structure in YZ plane (close to the edge of the gold patches at approximately y = 590 nm) for different ENZ film thicknesses from 2 to 300 nm; with P = 3 μm and W = 1200 nm. The gray patch area represents the ENZ layer. The markers are for visual guidance.

The hybrid modes inherit different fractions of plasmonic and ENZ character depending on detuning. Near the LO phonon frequency, the upper polaritons carry a larger ENZ admixture. In the ENZ regime the normal field becomes nearly uniform across the film and its amplitude scales inversely with thickness, producing strong FE inside the ENZ layer [5]. The lower polaritons are more plasmon-like; their fields concentrate mainly in the metal/dielectric gap and at metal interfaces rather than within the ENZ film, yielding a smaller FE inside the ENZ layer. Empirically, the depth of the reflectance dip correlates with the overlap of the mode with the ENZ layer and the degree of impedance matching; deeper dips in the upper polariton mode typically coincide with larger field energy inside the ENZ film, consistent with the

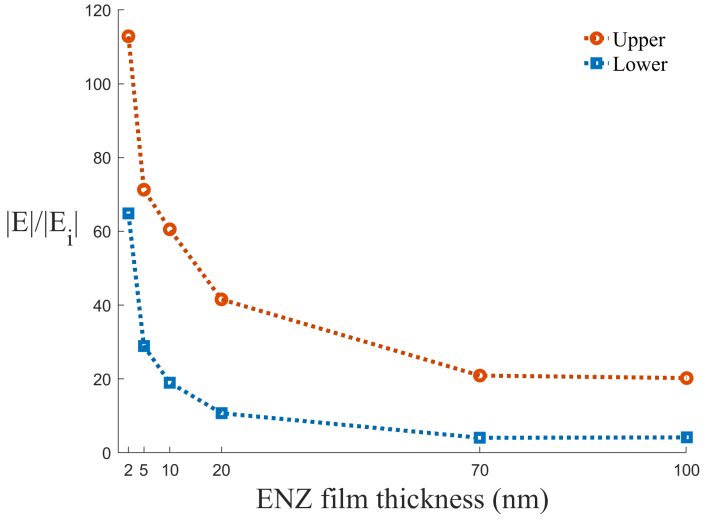

FIGURE 4.8: Simulation results showing the maximum field enhancement for different ENZ film thicknesses at the upper and lower hybridized polariton modes. The field enhancement pertains to YZ cross section at y = 590 (under and close to the edges of the gold patches) with P = 3 μm and W = 1200 nm.

larger FE we obtain [10, 11, 6]. As h decreases, ENZ-layer fields grow, but coupling to the gap-plasmon weakens. Our simulations point to an optimum in the **5–20 nm** range for oxide ENZ films, where the upper polaritons FE is near its maximum while linewidth and fabrication tolerances remain manageable. For experiments targeting $\chi^{(3)}$ in the ENZ layer, we therefore recommend exciting the upper polaritons at the thickness where (i) their reflectance minimum is deep and (ii) the ENZ-layer overlap factor is maximal.

4.4 Conclusion

We showed how the thickness of the phonon ENZ film can be exploited in the design procedure to control the coupling of the structure. We have demonstrated through simulation that the strongly coupled gap-plasmon antenna and aluminum oxide phononic ENZ film structure supports large electric field enhancements, particularly when the ENZ film is in the 5–20 nm range. In summary, the strongest ENZ-mediated field enhancement occurs for the upper polariton and follows the expected $\sqrt{h}$ scaling. This field concentration, driven by ENZ–plasmon hybridization, provides a platform for mid-IR nonlinear optics. These findings lay the groundwork for future experimental efforts aimed at realizing enhanced nonlinear optical effects using ENZ–plasmonic structures.

References

[1] M. Z. Alam, I. De Leon, and R. W. Boyd. "Large optical nonlinearity of indium tin oxide in its epsilon-near-zero region". In: *Science* 352.6287 (2016), pp. 795–797. DOI: 10.1126/science.aad3105.

[2] M. Zahirul Alam et al. "Large optical nonlinearity of nanoantennas coupled to an epsilon-near-zero material". In: *Nature Photonics* 12.2 (2018), pp. 79–83. ISSN: 1749-4893. DOI: 10.1038/s41566-017-0089-9. URL: https://doi.org/10.1038/s41566-017-0089-9.

[3] L. Caspani et al. "Enhanced nonlinear refractive index in ϵ-near-zero materials". In: *Physical Review Letters* 116.23 (2016), p. 233901. DOI: 10.1103/PhysRevLett.116.233901. URL: https://link.aps.org/doi/10.1103/PhysRevLett.116.233901.

[4] Orad Reshef et al. "Nonlinear optical effects in epsilon-near-zero media". In: *Nature Reviews Materials* 3 (2019), pp. 170–182. DOI: 10.1038/s41578-019-0120-5.

[5] Salvatore Campione, Igal Brener, and Francois Marquier. "Theory of epsilon-near-zero modes in ultrathin films". In: *Phys. Rev. B* 91.12 (2015), p. 121408. DOI: 10.1103/PhysRevB.91.121408.

[6] Daehan Yoo et al. "Ultrastrong plasmon–phonon coupling via epsilon-near-zero nanocavities". In: *Nature Photonics* 15 (2021), pp. 125–130. DOI: 10.1038/s41566-020-00731-5.

[7] Robert W Boyd. *Nonlinear optics*. Academic press, 2020.

[8] Saumya Choudhary et al. "Strongly Coupled Plasmon Polaritons in Gold and Epsilon-Near-Zero Bifilms". In: *ACS Photonics* 10.1 (2023), pp. 162–169. DOI: 10.1021/acsphotonics.2c01412. eprint: https://doi.org/10.1021/acsphotonics.2c01412. URL: https://doi.org/10.1021/acsphotonics.2c01412.

[9] Nikolai Christian Passler et al. "Strong Coupling of Epsilon-Near-Zero Phonon Polaritons in Polar Dielectric Heterostructures". In: *Nano Letters* 18.7 (2018). PMID: 29894195, pp. 4285–4292. DOI: 10.1021/acs.nanolett.8b01273.

[10] Fei Ding et al. "A review of gap-surface plasmon metasurfaces: fundamentals and applications". In: *Nanophotonics* 7.6 (2018), pp. 1129–1156. DOI: 10.1515/nanoph-2017-0125.

[11] Randall A. Smith, N. Asger Mortensen, and Sergey I. Bozhevolnyi. "Gap and channelled plasmons in tapered grooves: a review". In: *arXiv preprint arXiv:1503.00554* (2015). Also covers bow-tie antennas.

Chapter 5

Conclusion and Future Works

In this thesis, we explored the fundamental and applied aspects of light–matter interaction in epsilon-near-zero (ENZ) materials, with a particular focus on their phononic realizations in the mid-infrared (mid-IR) spectral range. The main focus of this work was the experimental and theoretical investigation of coherence in thermal emission from ultra-thin polar dielectric films under the ENZ condition, specifically silicon dioxide (SiO_2). Complementary to this, we also examined strong coupling between phonon ENZ modes and engineered gap-plasmonic resonances in gold antenna arrays, as well as the associated field enhancement phenomena arising from such hybridization. The convergence of these research directions has yielded insights relevant to both fundamental physics and the development of advanced photonic components.

The primary focus of this thesis was to investigate the coherence properties of thermal emission from thin SiO_2 films. Leveraging the epsilon-near-zero behavior of polar dielectrics, near their transverse and longitudinal optical phonons, we demonstrated that ultra-thin SiO_2 layers can support spectrally selective thermal radiation with improved temporal coherence near their LO phonon frequency. It was the first project related to thermal emission in our group and constitutes the first experimental study in our laboratory operating in the mid-IR spectrum. It involved extensive research to acquire the knowledge and skills to perform the experiments as well as numerical calculations, including the acquisition and integration of a Fourier-transform infrared (FTIR) spectrometer, thermal controlling, and mid-IR optical components. Our measurements show narrow TM-polarized emission features near the LO phonon; the Q-factor increases as the film thins, consistent with ENZ-supported modes. We established an FTIR-based mid-IR platform (instrumentation, thermal stages, and analysis codes) to carry out angle- and polarization-resolved emissivity measurements.

Our strategy to improve the coherence of thermal emission was based on the suppression of the unwanted emission modes and leveraging the ENZ condition to provide an in-phase field distribution over the emitter. These observations are consistent with the excitation of Berreman modes close to the longitudinal phonon-polariton resonances that become prominent near the ENZ condition. Importantly, our results reveal that coherence in thermal emission can be realized without the need for complex photonic crystals or metasurfaces, relying instead on the intrinsic material response of a sub-wavelength polar dielectric film. These findings were corroborated by simulations, which allowed us to systematically examine the relationship between film thickness, emission angle, and sharpness of our emissions. We showed that as the film becomes thinner, the Q-factor of the peak of the emission –observed around the LO phonon resonance frequency – increases, which we attributed to improved temporal coherence, and the emission becomes more spectrally narrow, consistent with theoretical predictions for ENZ-supported waveguide modes. This study contributes to the growing body of literature that positions polar dielectrics as viable alternatives to plasmonic materials for controlling thermal radiation in the infrared.

Building our understanding of phonon-induced ENZ materials, we explored strong coupling between the ENZ phonon polariton in an Al_2O_3 thin film and the gap-plasmon mode of a gold patch antenna array. By carefully designing the antenna geometry to overlap the plasmonic resonance with the LO phonon resonance of the dielectric, we observed pronounced anticrossing in the reflection spectra, a hallmark of strong coupling. The dispersion of the hybridized system revealed a resonance splitting that persisted for ENZ layer thicknesses up to a few tens of nanometers. This strong coupling regime results in the formation of upper and lower polariton branches. We analyzed this behavior across a range of ENZ film thicknesses and demonstrated that the coupling strength increased nearly linearly with the thickness h of the thin film (up to approximately 20 nm), followed by a sublinear regime described well by a $\sqrt{h}$ dependence. This trend reflects the fact that for very thin films, the ENZ mode remains well-confined and uniform, maximizing spatial overlap with the plasmonic field. As the film becomes thicker, the field distribution deviates from uniformity and the ENZ mode acquires dispersion, weakening the coupling. These findings support the potential of using ENZ materials as tunable optical cavities in integrated infrared photonics.

Finally, we performed full-wave electromagnetic simulations to quantify the electric

field enhancement enabled by the strong coupling between gap-plasmons and the ENZ mode in a thin film of Al_2O_3 polar dielectric. We found that for ENZ film thicknesses below 10 nm, the electric field within the dielectric layer was enhanced by up to two orders of magnitude relative to the incident field. This significant enhancement is attributed to the near-zero permittivity condition, yet not limited to the otherwise fixed ENZ frequency of the ENZ material. We demonstrated that this enhancement is highly localized inside the ENZ film and is strongly dependent on the ENZ layer thickness. As the film becomes thicker, the ENZ condition becomes less ideal, leading to a decrease in field confinement and enhancement. Our results show that optimal enhancement occurs in the 5–10 nm thickness range, where hybridization is strongest, and the ENZ condition is best maintained. The implications of this result are significant for nonlinear optics. The strong local field concentration within the ENZ region makes these structures promising candidates for mid-infrared nonlinear phenomena.

Outlook

This thesis has demonstrated the remarkable potential of ultra-thin polar dielectric films, particularly SiO_2, for engineering spectrally selective and partially coherent thermal emission in the mid-infrared. Building on these findings, several promising directions can be envisioned for future work.

Future work will examine (i) 3D-confined emitters (nanocubes, nanopillars, resonator arrays) to reshape the photonic DOS and (ii) gratings for momentum-matched out-coupling and enhanced directionality. In the current work, ultra-thin geometry was shown to be essential for suppressing unwanted modes and promoting coherence. The next step is to explore how nanostructured geometries—such as nanocubes, nanopillars, or resonator arrays—further reshape the photonic density of states and influence the angular, spectral, and polarization characteristics of thermal emission. By confining the emitter in all three dimensions, one can achieve even stronger modal control, potentially enabling sharp, highly directional emission from a nanoscale footprint. Apart from the application of modification of the emission, I am interested in exploring how the emission from 3D subwavelength particles might diverge from the Planck's law formalism for thermal emission. Does that result in a resonance shift in the emission peak, how much that change is adjustable.

A number of such structures are already being fabricated and will be measured in the near future in our lab. Additionally, we are fabricating SiO_2-based thermal emitters with surface gratings, aiming to enhance the directionality. These periodic structures have two implications, first to tailor the out-coupling of guided or surface-confined modes into the far field, and second to increase the spatial distribution of coherent oscillations thereby increasing the directionality of the emitter (analogous to array antennas). Once fabrication is complete, we will perform angle-resolved emissivity measurements to evaluate the effectiveness of this design.

Another exciting research direction involves using thermal emitters into optical resonators/cavities. Such a feedback mechanism could increase the Q-factor of the emission spectrum beyond what is achievable with material dispersion alone. Integration with high-reflectivity mirrors or photonic crystal structures could allow the realization of narrowband, coherent thermal sources with customizable emission wavelengths. These concepts pave the way toward the development of on-chip, integrated mid-infrared light sources that operate passively through thermal excitation—a promising alternative for sensing and spectroscopy in spectral regions where traditional semiconductor sources are limited. A further avenue of exploration is thermal source tunability. While most current emitters are static in frequency and profile, integrating active materials (e.g., phase-change media, graphene, electro-optic materials) or incorporating MEMS-based actuation could allow dynamic control of thermal emission spectra and directionality. This could enable programmable thermal emitters, useful for adaptive IR imaging or spectral encoding in free-space communications.

In parallel, the project on strong coupling between ENZ phonon polaritons and gap-plasmon resonators opens up a rich landscape for linear and nonlinear optics. A key future objective is to experimentally characterize the nonlinear response of the coupled system. Our laboratory is equipped with femtosecond pulsed lasers and a difference frequency generator (DFG), enabling mid-IR nonlinear spectroscopy. Using these tools, we plan to probe the enhancement of nonlinear processes such as four-wave mixing in the strongly coupled regime. Of particular interest is how optical pumping can modify the hybridized polariton modes—offering a potential pathway toward actively tunable, nonlinear ENZ-polariton platforms. Currently, we don't actually know how large a nonlinear response to expect, nor do we know how fast these responses are. On the other hand, these structures can also be of interest for the modification of thermal emission and harnessing the phononic dispersion.

In summary, the broader vision for this research open path to practical applications, including compact, tunable, and mid-IR thermal emitters, mid-IR sensing and nonlinear optical devices.

Appendix A

Numerical simulation methods

A.1 Finite-element simulations using COMSOL

The planar SiO_2/Si structures investigated in chapter 2 are analyzed with a frequency–domain finite-element method (FEM) implemented in COMSOL MULTIPHYSICS [1]. A two–dimensional model is used, representing an xz cross-section of an infinitely extended film stack. The fields are assumed to be invariant along the y-direction so that all quantities depend only on x and z.

A.1.1 Model geometry and boundary conditions

The model tree and the corresponding computational domain are shown in Fig. A.1. The stack consists of a semi-infinite Si substrate, an ultra-thin SiO_2 film, and a semi-infinite air region. The vertical boundaries (left and right) are treated as Floquet (periodic) boundaries, which enforce phase continuity for plane waves propagating parallel to the interface and effectively represent an infinitely extended film in the lateral direction. The top and bottom boundaries are defined as ports representing the incoming and outgoing plane waves in air and Si, respectively. Separate Electromagnetic Waves, Frequency Domain (EWFD) solvers are used for transverse–electric (TE) and transverse–magnetic (TM) polarizations. For the SiO_2 layer, we directly import the ellipsometry-derived refractive index data into COMSOL.

A.1.2 Port excitation, polarization, and meshing

Port settings for TE and TM simulations are illustrated in ig. A.2. For both polarizations, Port 1 at the top of the domain is used as the excitation port, while Port 2 at the bottom acts as the output. The ports are of the Periodic type. In the TE configuration shown in Fig. A.2(a), the input quantity is the electric field; an incident

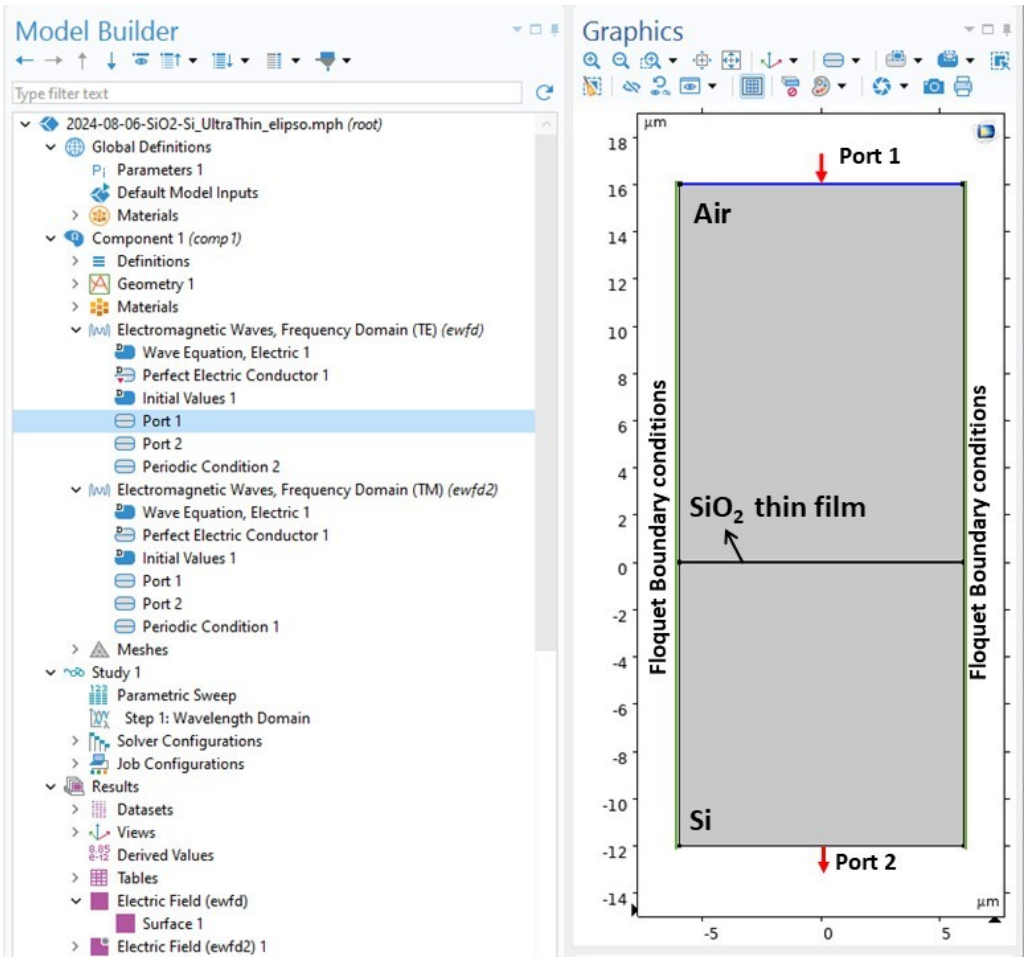

FIGURE A.1: COMSOL model for the planar SiO_2/Si structure. Left: model builder tree showing materials, TE/TM physics interfaces, ports, periodic boundary condition and study definition. Right: 2D cross-section of the computational domain with the ultra-thin SiO_2 layer on Si, Floquet boundary conditions on the vertical sides, and Port 1 (air) and Port 2 (Si) at the top and bottom, respectively.

plane wave with unit amplitude ($E_0 = 1$ V/m) is launched from Port 1 at normal incidence ($\theta_{\text{in}} = 0$). For TM polarization shown in Fig. A.2(b), the magnetic field is used as the input quantity and a unit-amplitude mode ($H_0 = 1$ A/m) is launched from the top port. In both cases, the port input power is set to $P_{\text{in}} = 1$ W/m so that the computed S-parameters can be directly interpreted as power reflection and transmission coefficients. The refractive index used in the automatic mode solver is taken from the corresponding material data (air or Si) at each wavelength.

The computational domain is discretized with triangular finite elements. A globally graded mesh is used, with strong refinement in the vicinity of the ultra-thin SiO_2 film where the fields vary most rapidly. As shown in Fig. A.3, the mesh is significantly denser in the oxide region than in the surrounding air and substrate, ensuring that the

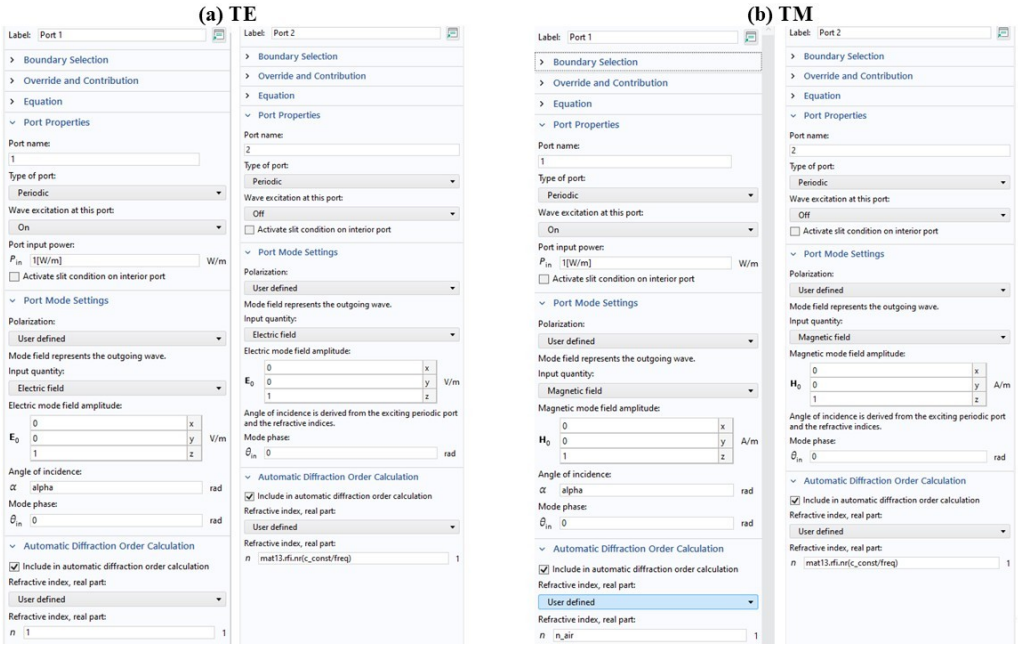

FIGURE A.2: Port settings in COMSOL for the planar SiO_2/Si structure. (a) TE case: the electric field is used as the input quantity with $E_0 = 1$ V/m at Port 1 and Periodic ports at both the top and bottom boundaries. (b) TM case: the magnetic field is the input quantity with $H_0 = 1$ A/m. In both polarizations, the ports are of the Periodic type, the input power is set to $P_{\text{in}} = 1$ W/m.

subwavelength thickness of the film is adequately resolved. Mesh-convergence tests were performed by systematically refining the mesh in and around the oxide layer and verifying that the resulting reflectance and bsorptance spectra remained unchanged within numerical accuracy.

A.1.3 Extraction of spectra

A parametric sweep over wavelength and angle of incidence is carried out for each polarization using the Wavelength Domain study step. COMSOL returns the complex scattering parameters $S_{11}(\lambda)$ and $S_{21}(\lambda)$, from which the reflectance and transmittance are obtained as

$$R(\lambda) = |S_{11}(\lambda)|^2 , \qquad T(\lambda) = |S_{21}(\lambda)|^2 . \tag{A.1}$$

The absorptance is then calculated as

$$A(\lambda) = 1 - R(\lambda) - T(\lambda). \tag{A.2}$$

These FEM-derived spectra are used in chapter 2 to compare with the measured

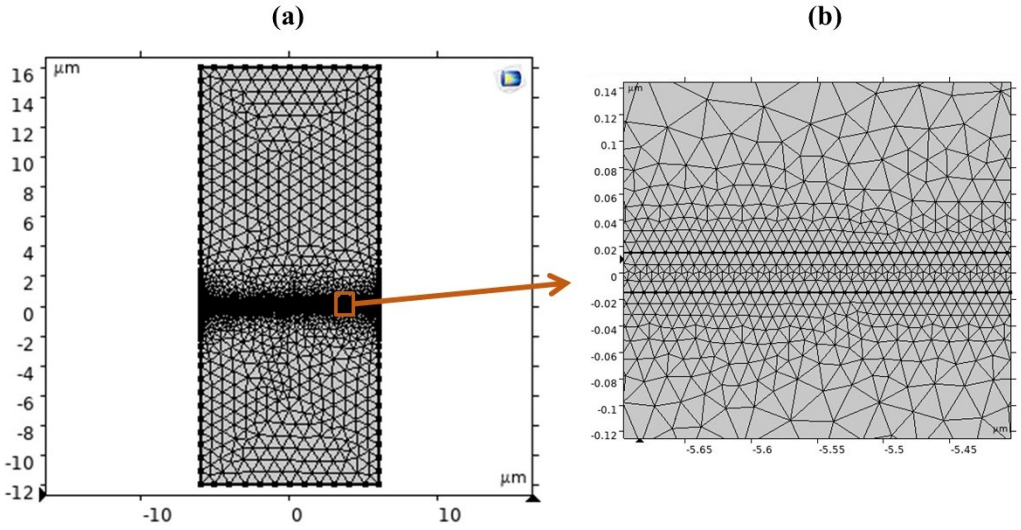

FIGURE A.3: Finite-element mesh used in the COMSOL simulations. (a) Global view of the triangular mesh for the full air/SiO_2/Si stack. (b) Zoomed view of the mesh in the vicinity of the ultra-thin SiO_2 layer, highlighting the strong refinement used to resolve the rapid variation of the fields across the film.

emissivity, and to quantify the influence of film thickness and material parameters on the absorption features.

A.2 Finite-difference time-domain method using Lumerical

Three-dimensional finite-difference time domain (FDTD) is a well-known method to solve the electrodynamics of a system numerically by discretizing the Maxwell equation in time domain using the central-difference approximation (sometimes referred to as the Yee lattice) [2, 3]. We used a commercial FDTD software package, known as Lumerical FDTD solver, to calculate the reflectance spectra of the structures discussed in chapter 3 and 4.

A.2.1 Geometry, source, and monitors

Fig. A.4 shows the Lumerical FDTD simulation detail for the gap-plasmon/ENZ structure. The figure shows the 3D model and cross-sectional views with the FDTD simulation region, plane-wave source plane, and the field and reflectance monitors. The simulated unit cell corresponds to a single gold patch on top of the multilayer stack Si/TiN (for gap-plasmomn antenna) and Si/Al_2O_3/TiN (for gap-plasmon antenna with the integrated ENZ thin film) discussed in chapter 3. The lateral size of the

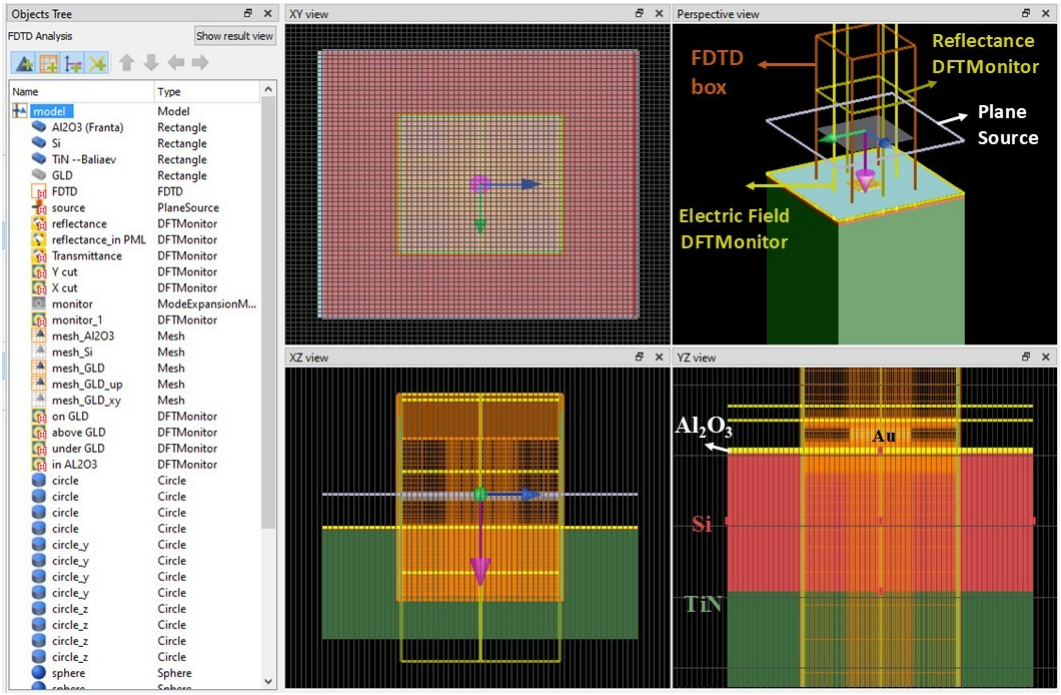

FIGURE A.4: Lumerical FDTD simulation showing the 3D model and cross-sectional views with the FDTD simulation region, plane-wave source plane, and the field and reflectance monitors

patch is W, the period of the array is P. The thicknesses of the Au, Al_2O_3, Si and TiN layers are chosen to match the fabricated samples. The structure is illuminated from the air by a normally incident, broadband plane-wave source. The source spectrum covers the mid-infrared range used in the experiments, and the fields are recorded in the frequency domain using built-in DFT monitors.

A.2.2 Boundary conditions, meshing, and convergence

Figure A.5 summarizes the key numerical settings used in the Lumerical FDTD simulations. To model an infinite periodic array, Bloch (periodic) boundary conditions are applied along the in-plane directions (x and y), with Bloch wave vectors corresponding to normal incidence, Fig. A.5 (a). Along the out-of-plane direction (z), perfectly matched layers (PMLs) are used at the top and bottom boundaries to absorb outgoing waves. The PMLs employ a stretched–coordinate implementation with a standard profile and multiple layers, ensuring efficient attenuation of outgoing fields. The FDTD simulation region is chosen large enough to include the entire multilayer stack and a portion of the surrounding air above the gold patch, as illustrated in the cross-sectional xz-view in Fig. A.5 (b). The upper PML is placed sufficiently far from the structure so that the near fields associated with the gap-plasmon mode and the

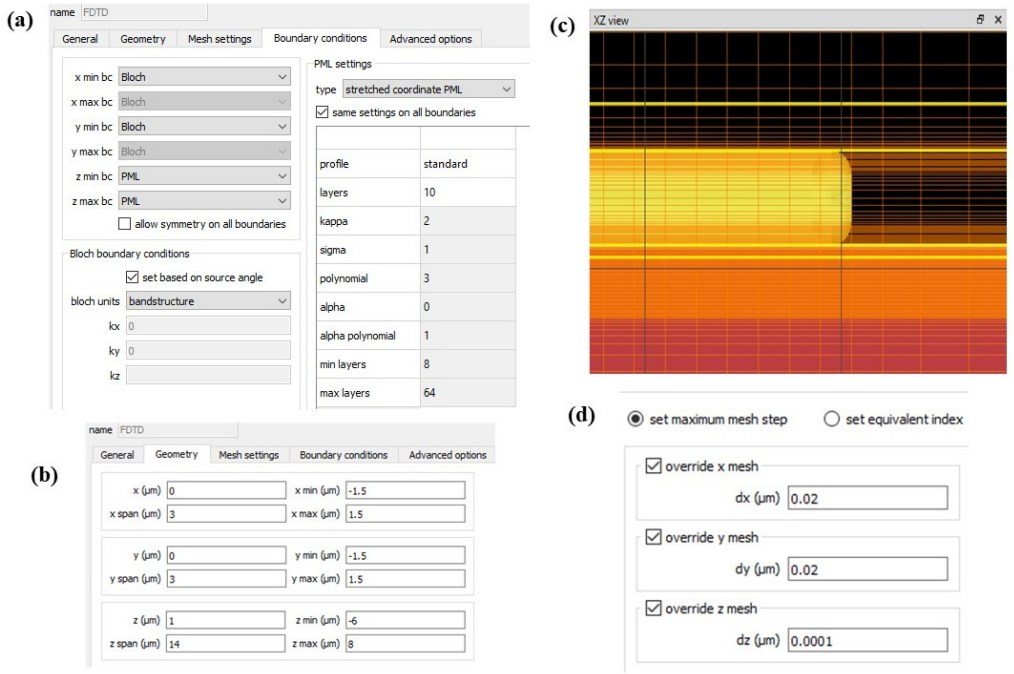

FIGURE A.5: Lumerical FDTD simulation settings. (a) Perfectly matched layer (PML) parameters using a stretched–coordinate PML with a standard profile. (b) Bloch (periodic) boundary conditions applied along the in-plane directions and PMLs along the out-of-plane direction. (c) Cross-sectional xz-view of the fine meshes around the gold patch edges and in the ENZ thin film. (d) Mesh-override settings specifying the maximum mesh step in the x, y, and z directions.

ENZ layer decay before reaching the absorbing boundary. Fig. A.5 (c) shows the fine meshes around the patch edges and the ENZ thin film. The mesh override settings are shown in Fig. A.5 (d); mesh steps are on the order of $\Delta x = \Delta y \approx 0.02$ μm and $\Delta z \approx 1 \times 10^{-4}$ μm, ensuring that the round geometries and the subwavelength ENZ layer are well resolved. Coarser mesh cells are used in regions far from the structure to reduce the total simulation time. The time step is chosen automatically by the software according to the Courant stability condition. The simulations are run until the residual field energy in the computational domain falls below a predefined auto-shutoff level, ensuring that all transient fields have decayed. Convergence was verified by repeating selected simulations with finer mesh sizes and thicker PMLs, confirming that the reflectance spectra and resonant wavelengths change negligibly.

A.2.3 Material models

Fig. A.6 shows the material–fit panels for the real and imaginary parts of the permittivity used in the FDTD model (solid lines) together with the target material data (symbols) over the simulated mid-infrared spectral range. For all simulations,

frequency-dependent material models are employed. The dispersive permittivities of Al_2O_3 and TiN are imported into the material database from external optical-constant data, while Au and Si are taken from standard tabulated data. In each case, the real and imaginary parts of the permittivity are fitted using multi-coefficient models over the wavelength range of interest, ensuring close agreement between the FDTD model and the underlying material data.

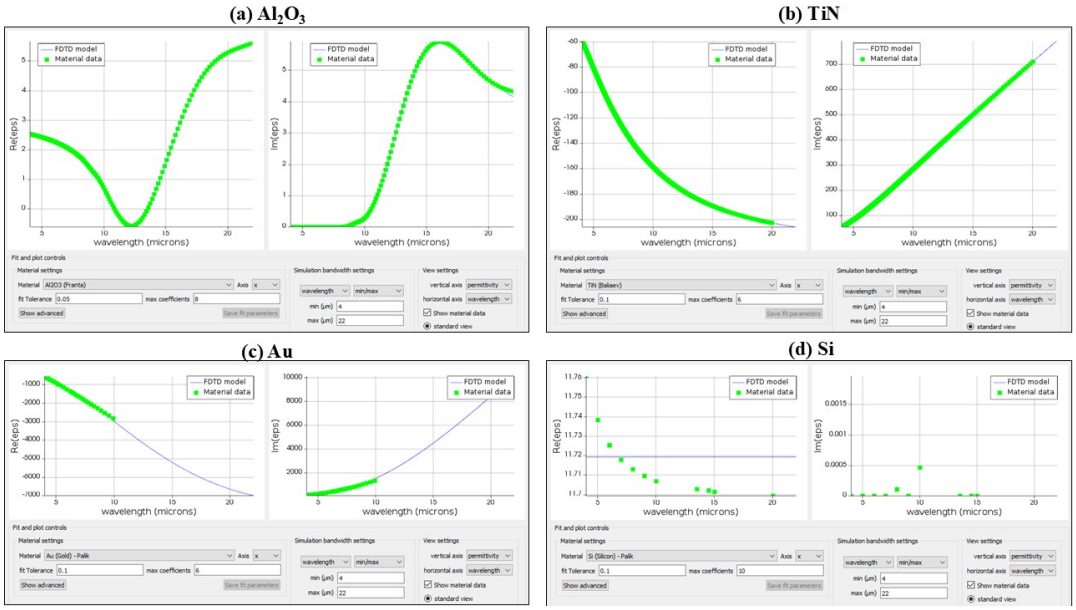

FIGURE A.6: Material fits used in the Lumerical FDTD simulations. (a) Al_2O_3, (b) TiN, (c) Au, and (d) Si. For each material, the green symbols represent the target permittivity data and the solid curves show the corresponding multi-coefficient fit used internally by the FDTD solver for both the real and imaginary parts of the permittivity.

A.2.4 Extraction of reflectance

Reflectance spectra are obtained from a frequency-domain power monitor placed in the air region above the structure, between the source plane and the top surface of the gold patches. The monitor records the upward and downward propagating components of the Poynting vector as a function of wavelength. The reflectance $R(\lambda)$ is calculated by normalizing the reflected power to the incident power of the plane-wave source,

$$R(\lambda) = \frac{P_{\text{reflected}}(\lambda)}{P_{\text{incident}}(\lambda)}. \tag{A.3}$$

Within the parameter sweep over the antenna width, W, and the ENZ thin film, h, this procedure is repeated automatically so that, for each value of W, both the

reflectance spectrum and the corresponding field profiles are obtained. These numerically obtained reflectance spectra are used throughout chapters 3 and 4 to identify the gap-plasmons and hybridized modes of the combined structure, to compare with the measured mid-infrared reflectance, and to quantify the dependence of the resonances on the ENZ-film thickness and other geometric parameters.

References

[1] Jian-Ming Jin. *The Finite Element Method in Electromagnetics*. 3rd ed. Hoboken, NJ: Wiley-IEEE Press, 2014.

[2] Dennis M Sullivan. *Electromagnetic simulation using the FDTD method*. John Wiley & Sons, 2013.

[3] Stephen D Gedney. "Introduction to the finite-difference time-domain (FDTD) method for electromagnetics". In: *Synthesis Lectures on Computational Electromagnetics* 6.1 (2011), pp. 1–250.

Appendix B

Nonlinear characterization using Z-scan technique

In our group, an artificial ENZ medium was realized by stacking SiO_2 and Ag layers. When the layer thicknesses are deeply subwavelength, the effective permittivity is well approximated by a thickness–weighted average of the constituent permittivities (effective–medium). Earlier measurements on this sample were performed at normal incidence and a single polarization [1]. We were interested to study the sample and its ENZ behavior over different polarizations, angles, and wavelengthes. My collaboration in this project was performing the measurements and collect the data. To investigate the nonlinear optical response of a metal–dielectric multilayer, I implemented the Z–scan technique which is an established method for measuring third–order nonlinear coefficients such as the nonlinear refractive index (n_2) and the two–photon absorption coefficient (β). It can also probe higher–order effects [2, 3]. The Z–scan method translates the sample along the propagation (z) axis of a focused beam while monitoring the transmitted power. In open–aperture Z–scan (no aperture before the detector), changes in transmission arise from nonlinear absorption (e.g., two–photon or saturable absorption). In closed–aperture Z–scan (a small aperture before the detector), the transmission becomes sensitive to nonlinear refraction; from these data one extracts n_2. Our goal here was to study how the nonlinear kerr effect varies with polarization, angle of incidence, and wavelength across the visible range (410–600 nm). My contribution was the experimental implementation: I built a Z–scan setup and collected data for TE and TM polarizations, angles of incidence from 0° to 55° in 5° steps, and wavelengths from 410 to 600 nm in 10 nm steps.

The schematic and the photograph of the setup are shown in Fig. B.1 and Fig. B.4. As observed in Fig. B.1, an Ekspla picosecond laser at 355 nm (28 ps, 50 Hz) pumps

an optical parametric generator (OPG) to generate tunable radiation from 410 to 600 nm. A spectral filter removes the idler. A half–wave plate (achromatic, AR coated) followed by a Glan–Taylor polarizer controls polarization state and average power; the wave plate is mounted on a motorized rotation stage. To clean the phase front and have a pure gaussian beam, the beam is focused with a 100 mm lens into a 100 μm pinhole (diamond aperture). The lens before the pinhole (L1) is mounted on a translation stage to compensate for small chromatic shifts of the focal spot. The diverging Gaussian beam is then collimated with a 300 mm lens. Fig. B.2 (a) and (b) show the measured beam intensity profiles before spatial filtering and after the spatial filter and collimation (after lens L2). The resulting collimated beam has a $1/e^2$ diameter of ∼2–3 mm with ellipticity >92% for all wavelengths reported in Table B.3.

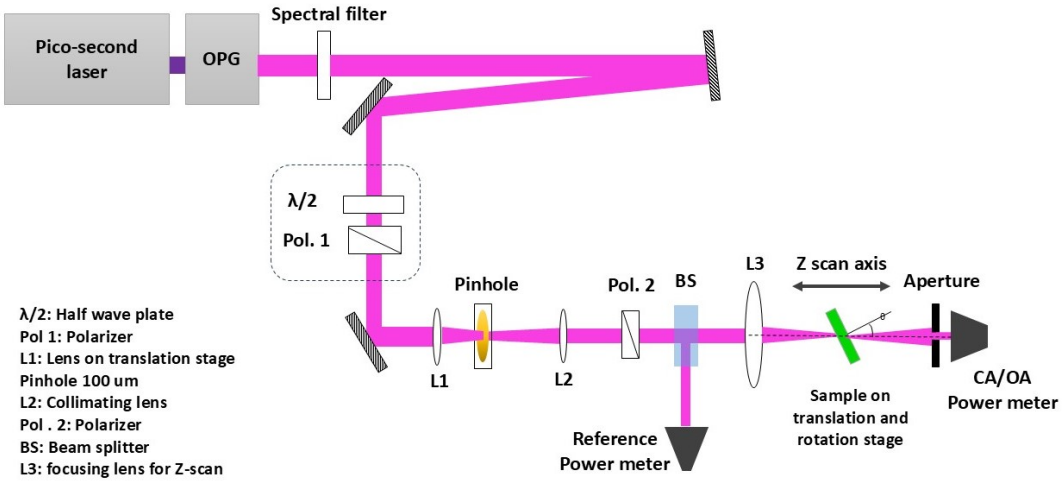

FIGURE B.1: Schematic of the Z–scan setup for angular and spectral measurements of the metal–dielectric ENZ multistack under TE and TM polarizations.

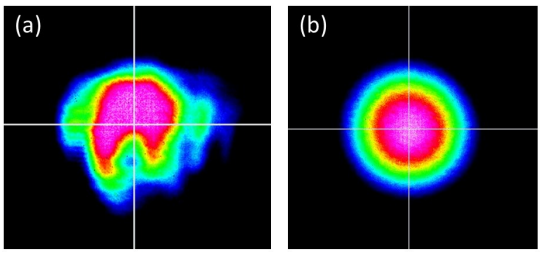

FIGURE B.2: Measured beam intensity profiles: (a) before spatial filtering, (b) after spatial filtering and collimation. The collimated beam (b) has a $1/e^2$ diameter of ∼2–3 mm and ellipticity >92% across 410–600 nm.

Wavelength (nm)	Diameter 1/e2 collimated input beam (mm)	Diameter 1/e2 Focoused beam (μm)	Diameter FWHM Focoused beam (μm)
410	2.131	24.5	20.76
420	2.076	25.76	21.83
430	2.359	23.21	19.67
440	2.447	22.89	19.4
450	2.477	23.13	19.6
460	2.51	23.33	19.77
470	2.554	23.43	19.85
480	2.537	24.09	20.41
490	2.617	23.83	20.2
500	2.629	24.21	20.52
510	2.703	24.05	20.38
520	2.653	24.95	21.14
530	2.785	24.22	20.53
540	2.777	24.75	20.98
550	2.728	25.67	21.75
560	2.906	24.53	20.79
570	2.843	25.52	21.63
580	2.879	25.65	21.74
590	2.988	25.14	21.3
600	3.106	24.6	20.84

FIGURE B.3: Measured $1/e^2$ diameter of the collimated input beam and calculated $1/e^2$ and FWHM diameters at focus.

A rotatable polarizer sets TE/TM polarization of the beam. A pellicle beam splitter directs a small fraction of the beam to a reference detector to record source fluctuations during Z–scan and enable normalization of both open– and closed–aperture traces. After the sample, a diffraction–limited aspheric lens ($f = 100$ mm) focuses the beam along the z–axis. The z–scan travel length is 2 cm. The sample mount consists of a rotation stage atop a linear stage, allowing automated angular scans and z–translation. The focused spot size and Rayleigh range z_0 were calculated, and the thin–sample condition $L \ll z_0$ (with L the film thickness) was verified. Measurements were performed at a fixed peak intensity of ~ 80 MW/cm^2 at the focus, with a beam diameter of approximately 25 μm (at $1/e^2$). For each wavelength, polarization, and angle, we recorded open–aperture and closed–aperture transmissions. The aperture (1 mm) was mounted on a two–axis stage for precise centering. We initially attempted simultaneous acquisition of open– and closed–aperture signals using a pellicle splitter after the sample, but due to weak signals we adopted sequential measurements without the post–sample splitter. I also wrote a python code to control the setup and collect the data (the motor stages, power meters, and etc.). As a representative of the measurements we show two sets of measurements in here. Fig. B.5 present data at TE polarization and 480 nm: (a,b) raw closed– and open–aperture signals; (c,d) corresponding signals normalized by the reference channel for multiple incidence angles. Fig. B.6 present data at TM polarization and 505 nm: (a,b) raw closed– and open–aperture signals; (c,d) corresponding signals normalized by the reference channel for multiple incidence angles.

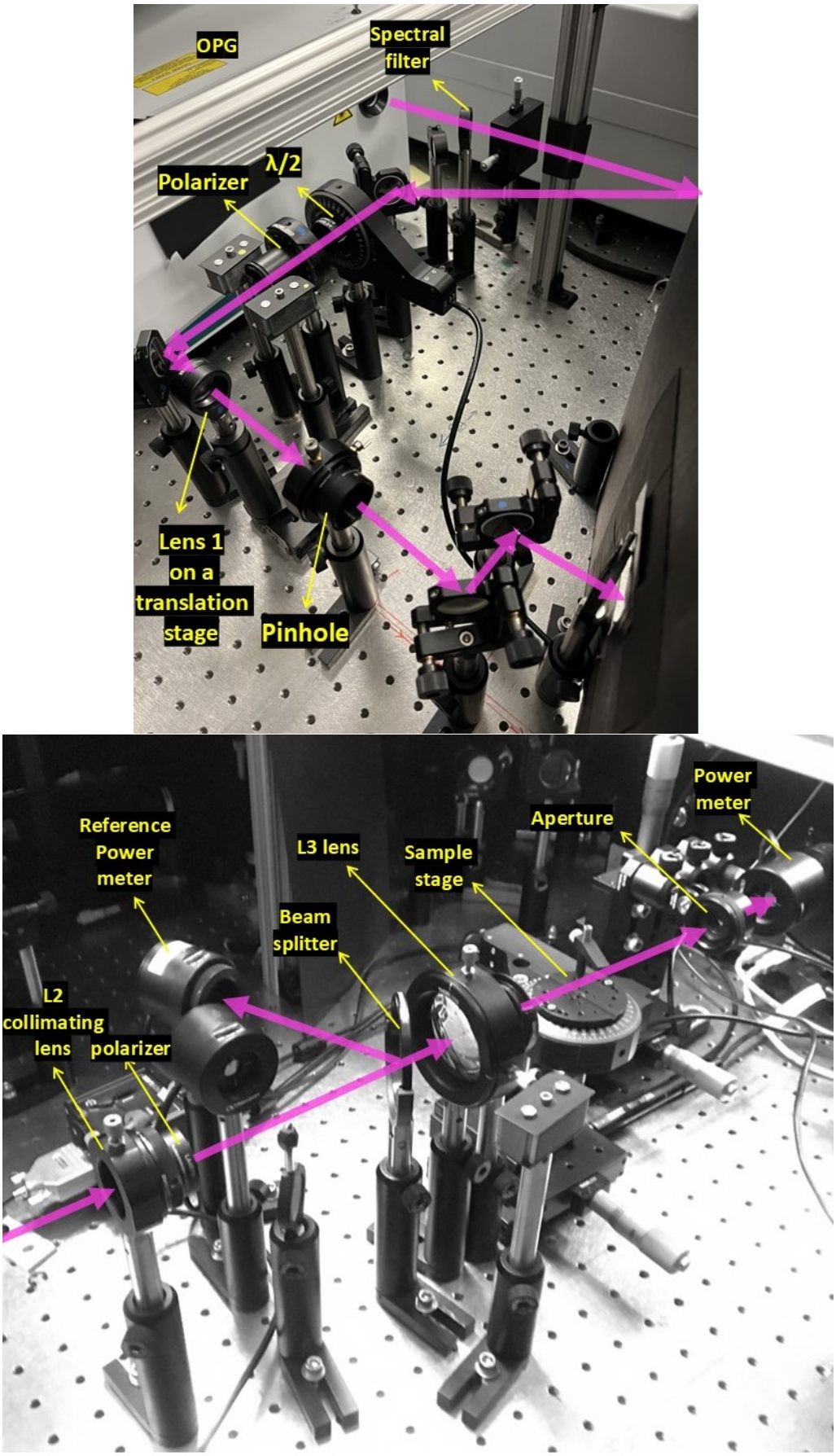

FIGURE B.4: Photographs of the Z–scan apparatus for angular and spectral measurements of the metal–dielectric ENZ multistack under TE and TM polarizations.

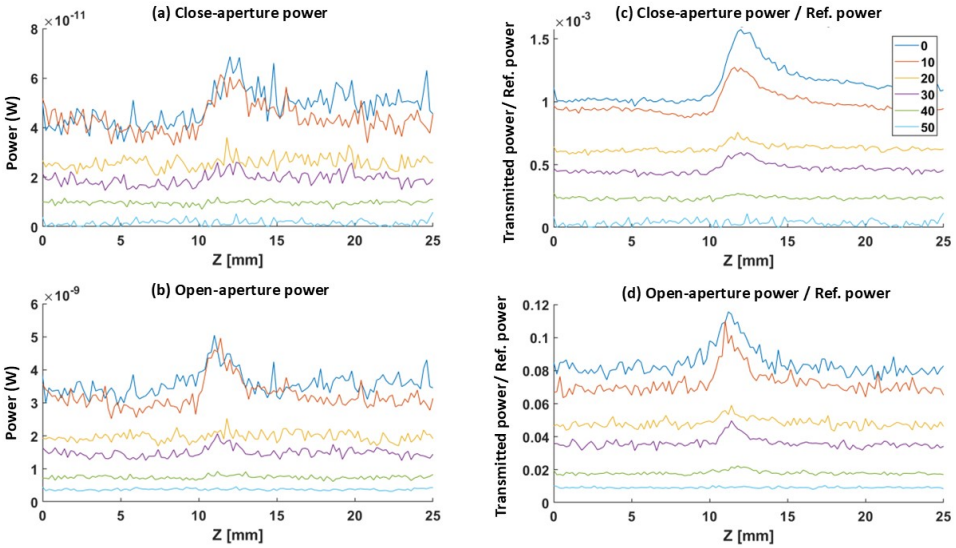

FIGURE B.5: Representative data at TE polarization and 480 nm: (a,b) raw closed– and open–aperture signals; (c,d) corresponding signals normalized by the reference channel for multiple incidence angles.

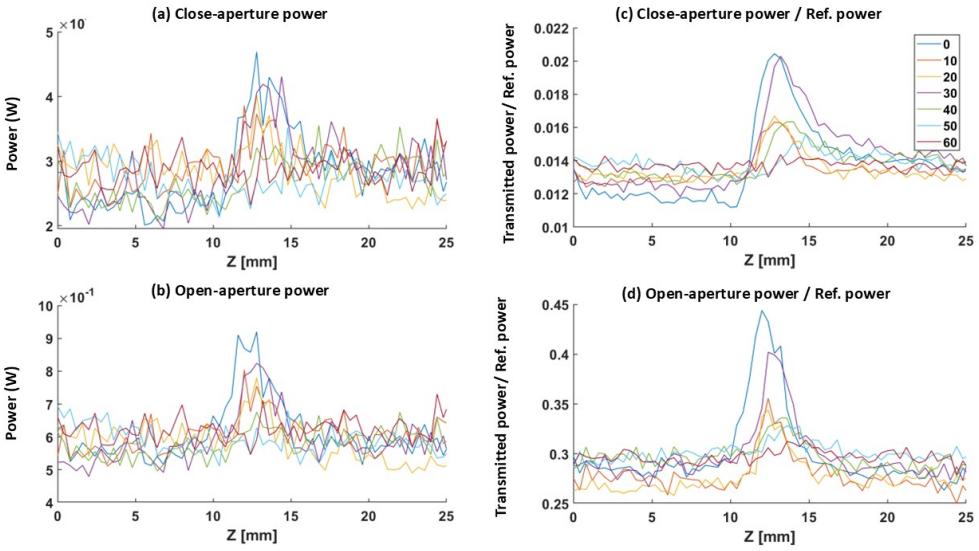

FIGURE B.6: Representative data at TM polarization and 505 nm: (a,b) raw closed– and open–aperture signals; (c,d) corresponding signals normalized by the reference channel for multiple incidence angles.

References

[1] Sisira Suresh et al. "Enhanced Nonlinear Optical Responses of Layered Epsilon-Near-Zero Metamaterials at Visible Frequencies". In: *ACS Photonics* 8.1 (Jan. 2021), pp. 125–129. DOI: 10.1021/acsphotonics.0c01178. URL: https://doi.org/10.1021/acsphotonics.0c01178.

[2] M. Sheik-Bahae et al. "Sensitive measurement of optical nonlinearities using a single beam". In: *IEEE Journal of Quantum Electronics* 26.4 (1990), pp. 760–769. DOI: 10.1109/3.53394.

[3] Cid B. de Araújo, Anderson S. L. Gomes, and Georges Boudebs. "Techniques for nonlinear optical characterization of materials: a review". In: *Reports on Progress in Physics* 79.3 (2016), p. 036401. DOI: 10.1088/0034-4885/79/3/036401. URL: https://doi.org/10.1088/0034-4885/79/3/036401.